HIGH-TEMPERATURE LINEAR RADIATION-CAVITY
SOLAR COLLECTOR WITH A FRESNEL CONCENTRATOR

Zenen I. Antoniak

DDC
FEB 13 1978
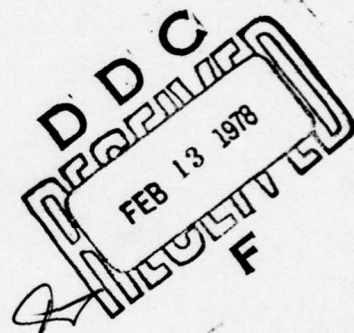F

The Pennsylvania State University
Institute for Science and Engineering
APPLIED RESEARCH LABORATORY
Post Office Box 30
State College, PA 16801

NAVY DEPARTMENT

NAVAL SEA SYSTEMS COMMAND

REPORT DOCUMENTATION PAGE	READ INSTRUCTIONS BEFORE COMPLETING FORM	
1. REPORT NUMBER TM-77-326	**2. GOVT ACCESSION NO.**	**3. RECIPIENT'S CATALOG NUMBER**
4. TITLE (and Subtitle) HIGH-TEMPERATURE LINEAR RADIATION-CAVITY SOLAR COLLECTOR WITH A FRESNEL CONCENTRATOR.	**5. TYPE OF REPORT & PERIOD COVERED** PhD Thesis, March 1978 Doctoral thesis	
	6. PERFORMING ORG. REPORT NUMBER TM 77-326	
7. AUTHOR(s) Zenen I. Antoniak	**8. CONTRACT OR GRANT NUMBER(s)** N00017-73-C-1418	
9. PERFORMING ORGANIZATION NAME AND ADDRESS The Pennsylvania State University Applied Research Laboratory P. O. Box 30, State College, PA 16801	**10. PROGRAM ELEMENT, PROJECT, TASK AREA & WORK UNIT NUMBERS**	
11. CONTROLLING OFFICE NAME AND ADDRESS Naval Sea Systems Command Department of the Navy Washington, D. C. 20362	**12. REPORT DATE** December 8, 1977 8 Dec 77	
	13. NUMBER OF PAGES 234 pages & figures 235 p.	
14. MONITORING AGENCY NAME & ADDRESS(if different from Controlling Office)	**15. SECURITY CLASS. (of this report)** Unclassified, Unlimited	
	15a. DECLASSIFICATION/DOWNGRADING SCHEDULE	

16. DISTRIBUTION STATEMENT (of this Report)

Approved for public release, distribution unlimited,
per NSSC (Naval Sea Systems Command), 1/8/78.

D D C
RECEIVED
FEB 13 1978
F

17. DISTRIBUTION STATEMENT (of the abstract entered in Block 20, if different from Report)

18. SUPPLEMENTARY NOTES

19. KEY WORDS (Continue on reverse side if necessary and identify by block number)

Solar energy   Heat Transfer
Solar collector
Fresnel
Radiation

20. ABSTRACT (Continue on reverse side if necessary and identify by block number)

A model solar-thermal concentrator-collector that is 1/6th scale (in cross section) relative to a system considered to be of practical dimensions for power generation has been constructed and tested. It consists of an Archimedes (i.e., Fresnel) mirror-concentrator, 5 cm ID x 1.5 m long glass receiver pipe, 0.3 cm thick graphite absorber, and gaseous (Ar) heat transfer medium. The mirror-contractor utilizes 40 suitably tilted reflective strips, each 1.6 cm wide by 1.5 m long; the strips are mounted in a parallel planar array which

DD FORM 1 JAN 73 **1473**   EDITION OF 1 NOV 65 IS OBSOLETE   391 007   UNCLASSIFIED

20. ABSTRACT (Continued)

moves east-west within two 1.67 m dia. tracks located near its ends. The glass receiver pipe holds the thin material that absorbs the concentrated solar radiation focused on it and transfers it as thermal energy to the flowing gas, which exits at high temperature. This receiver pipe remains fixed. The insulation (2.5 cm thick) surrounding the pipe, except for a narrow (2 cm wide) longitudinal aperture, rotates in such a manner that alignment between the aperture and the tracking concentrator is always maintained. The collector is tilted at 41° (the latitude of State College, PA) from the horizontal so that its axis is parallel to the earth's rotational axis when the device is oriented north-south. The small size of the aperture and the internalized flux absorption and heat transfer within the cavity receiver reduce thermal and radiative losses substantially. An alternative 0.09 cm thick copper absorber with a selective oxide surface has also been employed. / sq. m.

On clear days (direct solar flux ca. 800 W m^{-2}), stagnation (i.e., no-flow condition) temperatures of ca. 370°C have been reached at the center of the experimental device, where end effects are minimal. Experiments have been performed with gas flow rates up to ca. 100 liters/min (200 RE 2000), resulting in a bulk fluid temperature rise in the axial (flow) direction of up to 285°C. These experiments have been utilized in a study of heat transfer processes within the collector. A computer model of this system which takes into account most of the influential variables (e.g., combined forced-free convection, establishment of velocity and temperature profiles, and axial heat conduction) has been developed. Its behavior agrees well with observations. Also, after ca. 200 h of high-temperature operation, materials degradation was measured and found to be very low.

The good agreement between the analytical and experimental results permitted the formulation of a second computer model, of the full-scale device, with confidence. The effect of various parameters such as insulation thickness, aperture width, and antireflective coatings has been investigated in an optimazation sutdy of the proposed full-scale collector. It was concluded that the aperture width, aperture emittance, and mirror reflectance exert the strongest influence on the exit temperature and collector efficiency.

ii

ABSTRACT

A model solar-thermal concentrator-collector that is 1/6th
scale (in cross section) relative to a system considered to be of
practical dimensions for power generation has been constructed
and tested. It consists of an Archimedes (i.e., Fresnel) mirror-
concentrator, 5 cm I.D. x 1.5 m long glass receiver pipe, 0.3 cm
thick graphite absorber, and gaseous (Ar) heat transfer medium.
The mirror-concentrator utilizes 40 suitably tilted reflective
strips, each 1.6 cm wide by 1.5 m long; the strips are mounted in a
parallel planar array which moves east-west within two 1.67 m dia.
tracks located near its ends. The glass receiver pipe holds the
thin material that absorbs the concentrated solar radiation focused
on it and transfers it as thermal energy to the flowing gas, which
exits at high temperature. This receiver pipe remains fixed. The
insulation (2.5 cm thick) surrounding the pipe, except for a narrow
(2 cm wide) longitudinal aperture, rotates in such a manner that
alignment between the aperture and the tracking concentrator is
always maintained. The collector is tilted at 41° (the latitude of
State College, PA) from the horizontal so that its axis is parallel
to the earth's rotational axis when the device is oriented north-south.
The small size of the aperture and the internalized flux absorption

and heat transfer within the cavity receiver reduce thermal and radiative losses substantially. An alternative 0.09 cm thick copper absorber with a selective oxide surface has also been employed.

On clear days (direct solar flux ca. 800 W m^{-2}), stagnation (i.e., no-flow condition) temperatures of ca. 370°C have been reached at the center of the experimental device, where end effects are minimal. Experiments have been performed with gas flow rates up to ca. 100 liters min^{-1} (200 < Re < 2000), resulting in a bulk fluid temperature rise in the axial (flow) direction of up to 285°C. These experiments have been utilized in a study of heat transfer processes within the collector. A computer model of this system which takes into account most of the influential variables (e.g., combined forced-free convection, establishment of velocity and temperature profiles, and axial heat conduction) has been developed. Its behavior agrees well with observations. Also, after ca. 200 h of high-temperature operation, materials degradation was measured and found to be very low.

The good agreement between the analytical and experimental results permitted the formulation of a second computer model, of the full-scale device, with confidence. The effect of various parameters such as insulation thickness, aperture width, and antireflective coatings has been investigated in an optimization study of the proposed full-scale collector. It was concluded that the aperture width, aperture emittance, and mirror reflectance exert the strongest influence on the exit temperature and collector efficiency.

TABLE OF CONTENTS

LIST OF TABLES

LIST OF FIGURES

NOMENCLATURE

Dimensionless Numbers

Gr   Grashof number, $\beta g a^4 \frac{dT_B}{dz} / \nu^2$

Nu   Nusselt number, $\bar{h} D_h/k$

Pr   Prandtl number, $C_p \mu/k$

Ra   Rayleigh number, $\beta \rho^2 g C_p \frac{dT_b}{dz} a^4/k \mu$ $(= Gr \cdot Pr)$

Re   Reynolds number, $\rho V_m D_h/\mu$

z^+ axial position, z/D_h Re Pr

Roman Letters

a $1/2 D_h$

A   area

A_c flow cross-sectional area, cm^2

A_p heat transfer area, per unit axial length, $cm^2 cm^{-1}$

C_p specific heat at constant pressure, $J g^{-1} {}^{\circ}C^{-1}$

D_h hydraulic diameter, $4A_c/A_p$, cm

g   gravitational acceleration, $cm\ s^{-2}$

h   heat transfer coefficient, $W\ cm^{-2}\ °C^{-1}$

$\bar{h}$ peripheral average heat transfer coefficient at a given axial position z, $W\ cm^{-2}\ °C^{-1}$

k   fluid thermal conductivity, $W\ cm^{-1}\ °C^{-1}$

L   length, cm

$\dot{m}$ mass flow rate ($= A_c V_m \rho$), $g\ s^{-1}$

P   pressure, cm

q_{C1} heat loss through insulation, per unit axial length, $W\ cm^{-1}$

q_{C2} heat loss by axial conduction, per unit axial length, $W\ cm^{-1}$

q_L $q_R + q_{C1}$, sum of radial heat losses, per unit axial length, $W\ cm^{-1}$

q_N $q_S - q_L - q_{C2}$, net heat input into gas, $W\ cm^{-1}$

q_R heat loss from radiation by aperture, (i.e., Pyrex + side walls), per unit axial length, $W\ cm^{-1}$

q_S solar flux incident on receiver, per unit axial length, $W\ cm^{-1}$

R   radius, cm

T   temperature, °C

T_b bulk (mean mixed over A_c) fluid temperature $(A_c V_m)^{-1} \int_{A_c} V\, T\, dA_c$, °C

$\bar{T}_w$ peripheral average wall temperature at a given axial position z; average temperature of aperture sides at a given axial position z, °C

V_m average velocity over A_c, cm s^{-1}, STP

W width, cm

z axial position from onset of heating, cm

Greek Letters

α absorptance

β coefficient of thermal expansion, $1/\rho \; (\partial\rho/\partial T)_p$, °C^{-1}

ε emittance

λ wavelength, μm

μ dynamic viscosity, g s^{-1} cm^{-1}

ν kinematic viscosity, cm^2 s^{-1}

ρ density, g cm^{-3}; reflectance

σ Stefan – Boltzmann constant

τ transmittance

Subscripts

e   of the external insulation surface

g   of the gas (i.e., fluid)

G   of the graphite

i   inside surface

M   of the mirror

o   outside surface

p   pressure; perimeter

P   of the Pyrex (glass receiver)

w   at the wall (i.e., aperture sides or inside perimeter of receiver, Pyrex + graphite)

∞ ambient conditions

ACKNOWLEDGMENTS

CHAPTER I

SOLAR THERMAL PROCESSES

A. Introduction

Solar thermal power generation is one method currently being investigated as a potential means of converting solar energy to electricity. This involves a number of steps: collection of the solar flux as thermal energy; transfer of this energy to a suitable fluid; conversion to mechanical energy via a heat engine; and, finally, coupling of the engine to an electric generator. Except for differences in energy sources, the process is essentially the same as that employed in large nuclear and fossil-fuel electric generating stations. Thus, research centers on the solar-to-heated working fluid steps, these having a decisive influence on overall system efficiency.

The heat engine (usually a Rankine or Brayton cycle) has the Carnot efficiency as a theoretical upper bound. Because for a specified heat rejection temperature the Carnot efficiency is a function solely of the operating fluid temperature at the inlet of the heat engine, a high exit fluid temperature from the solar collector is a prerequisite for a realistic design. The required high temperature can only be achieved by a focusing (i.e., concentrating)

collector. Focusing collectors utilize optical systems - reflectors or refractors - to increase the (normally low) intensity of solar radiation impinging on the absorber. Higher energy flux on that surface results in a smaller surface area for a given total amount of energy transfer, and correspondingly reduced thermal losses, thus permitting higher temperatures to be reached.

Unfortunately, focusing collectors have a number of disadvantages when compared with the simpler non-focusing flat-plate collectors:

(1) optical transmission losses become significant because of the imperfect optics of a real concentrator;

(2) generally, only the direct component of solar radiation can be utilized;

(3) the added cost and complexity of concentrator and tracking systems must be borne.

It is obvious that, for a given incident flux, the maximum useful output of a collector will be obtained when the sum of the thermal and optical losses is a minimum. There is a trade-off to be made here, for at high concentration ratios (i.e., small receiver) much of the energy will miss the receiver altogether, while at low concentrations the large receiver surface will lose much of the energy. A large number of designs have been proposed that attempt to improve collector performance. These designs can usually be

placed in one of two broad categories: long linear collectors (also termed "distributed collection systems") of the solar-farm type, or tower receivers with flat heliostats.

B. The Solar Farm

Long linear collector designs covering large land areas have been extensively treated by the Meinels (1), and by Duffie and Beckman (2). The absorber pipe is often placed within an evacuated glass envelope, and the solar flux is most frequently concentrated by either a parabolic trough reflector (3) or the less common Fresnel refractor (4), which has been investigated by Nelson et al. (5). A selective surface is proposed for the absorber exterior, and part of the envelope is silvered to be highly reflective (see Figure 1) (4,6). Heat at high temperature is extracted via a fluid flowing through the absorber pipe, exiting at ca. 500°C; the fluid can be sodium (4) or steam (7). Parasitic fluid pumping losses, for a receiver up to 1 km in length, have been shown to be negligibly small in comparison with the power produced (7).

The theoretical analysis of such a collector's performance has frequently been extremely simplified (1,3,4). A more complex mathematical formulation of heat exchange within the receiver and to the ambient environment, as well as the effects of several fluid types, the inlet temperature, and the flow rate, is given by Lee and Schimmel (6). For turbulent flow, the percentage of energy extracted by the fluid from the incoming solar flux is estimated at 40-50%;
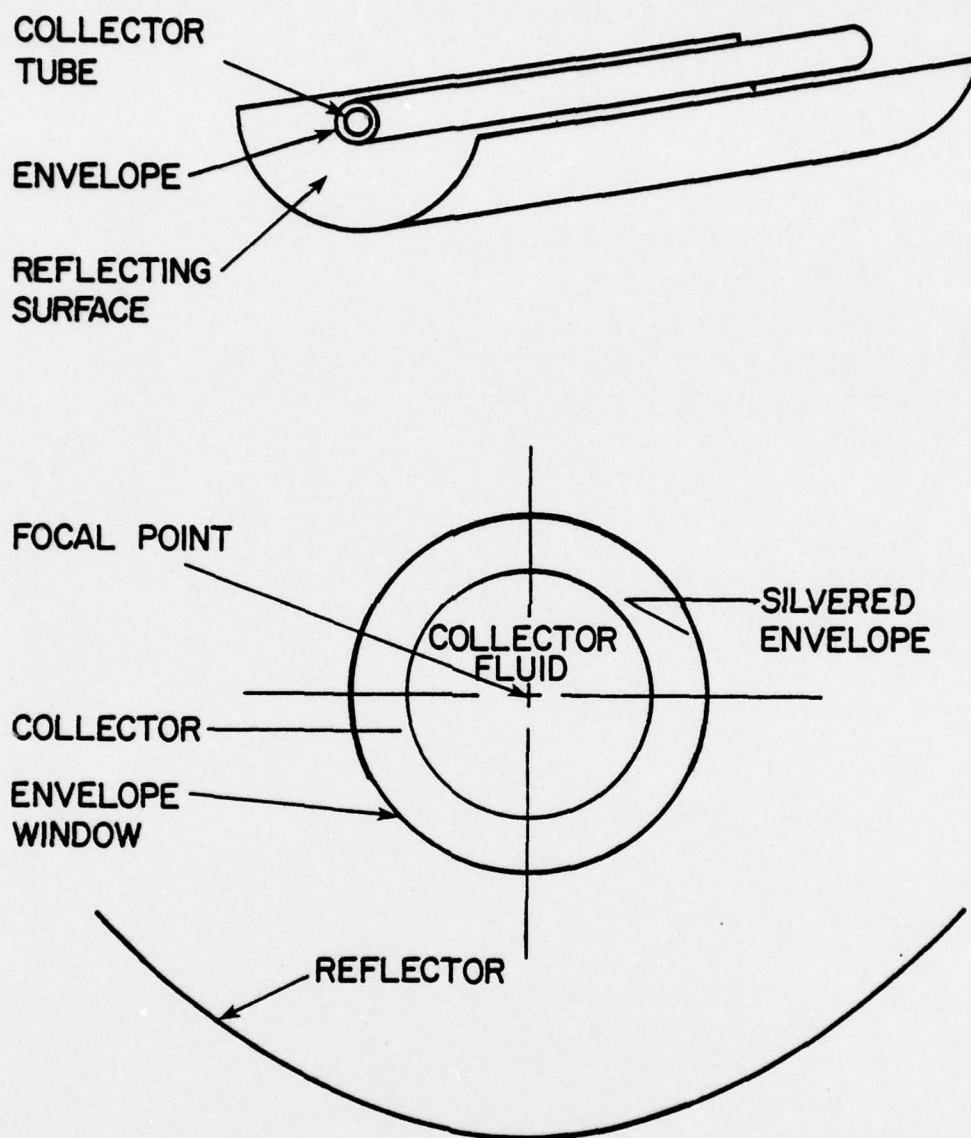
Figure 1. Cylindrical parabolic collector.

selective coatings on the absorber were found to be relatively unimportant if the surrounding envelope is silvered (6). A fairly comprehensive analysis is presented by Edenburn (8), who considered both an evacuated and a non-evacuated annular receiver, with Therminol 66 as the working fluid. Experimentally determined and calculated efficiencies of heat transfer (not defined) are stated to be in excellent agreement, and range between 35-62%, with fluid inlet temperatures spanning 475-578°K (8).

Recent experiments with water (9) and an evacuated envelope about the receiver pipe resulted in peak efficiencies at 300°C (defined as net heat delivered/perpendicular solar flux) of 50% and 30%, respectively, for a selectively coated and a black painted tube. Cobble and Smith (10) analyzed in detail a projected 5 kW solar electric generating station with air as the working fluid in an open Brayton cycle and predict an overall maximum efficiency (cycle power/flux on concentrator) of about 6%, with an optimum z ($z = T_{max}/T_{inlet}$, over the cycle) of approximately 2.9. No envelope or insulation was considered around the absorber pipe. This conversion efficiency is only about one-half the projected 12% calculated by Meinel and Meinel for a steam turbine cycle (7). The latter authors propose a 1.61 km^2 "farm," with a collector fill factor of 50%, operating over a $\Delta T = 100°C$, and producing a peak electrical output of 90 MWe at the quoted efficiency.

Optimization studies have been done by many. For example, Singh and Cheema (11) studied the performance of a cylindrical-parabolic collector, while Howell and Bannerot (12) investigated

maximizing cycle work output, and Turner (13) considered minimizing the piping and insulation requirements. The entire solar farm concept has recently been the subject of very comprehensive research efforts by the University of Minnesota and Honeywell (14); however, further evolutionary development of the concept appears to have been brought nearly to a halt in favor of the solar tower approach.

C. The Solar Tower

The solar tower concept is currently under intensive development by DOE (the federal Department of Energy) with progressively larger test facilities planned. This concept differs from others in that it replaces most of the plumbing required for transport of heat to the power plant by optical transmission of the solar flux to a central receiver. Very high concentration ratios, on the order of 1000, are achievable; thus, the solar flux can theoretically be utilized at the highest temperatures tolerated by the materials employed, with relatively low energy losses from re-radiation and convection.

A typical solar tower power plant is shown in Figure 2. Heliostats, comprised of two-axis steerable flat reflectors and ancillary equipment, are situated at ground level about a tower. The solar flux incident on the reflectors is continuously directed at a receiver on top of the tower where it is converted to heat in an energy transfer fluid. The heat is transported to the ground and used to operate a heat engine (15,16). For a nominal 100 MWe power
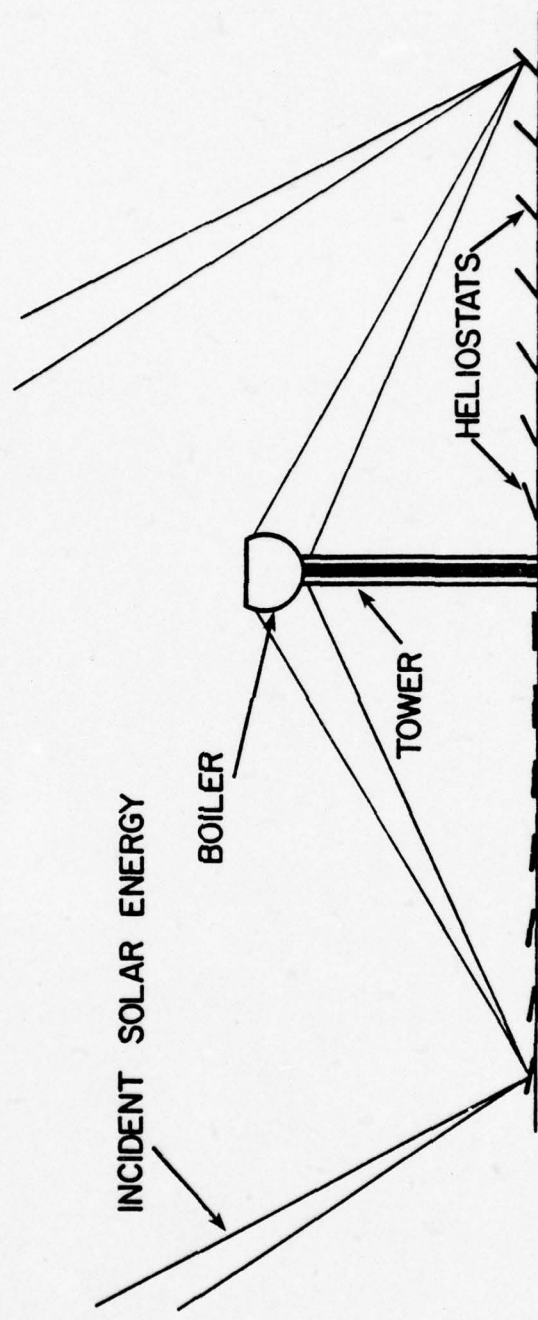
Figure 2. Cross-sectional view of solar tower system.

plant, the overall thermal collection efficiency attainable was estimated at about 60% (17) early in the design process. The system would require eight 426 x 426 m modules each containing 1840 - 37.2 m^2 heliostats and a 122 m high tower with a cavity steam generator receiver of approximately 94% conversion efficiency (heat into steam/energy into cavity) (18). The land area requirement here is about the same as for a linear receiver farm of similar output.

Although seemingly simpler, the solar tower design has some disadvantages peculiar to itself. These are:

(1) onerous tracking requirements;

(2) flux and temperature peaks at potentially unacceptable levels on the receiver;

(3) additional costs for the support tower and heliostat mounts/tracking mechanisms.

To achieve the desired concentration factor of ca. 1000, the total optical aberration must be limited to 2-4 milliradians (mr); this requires optical flatness of the reflector surface to ca. 2 mr, and tracking accuracy to ca. 1 mr (19). Flux distributions on the receiver surface have been studied by Lipps (20), and by Riaz and Gurr (21), among others; Blake et al. (18) also considered the temperature distribution. If all the heliostats are aimed at the central zone of a receiver, unacceptably high Gaussian-like

flux peaks result (19) with the currently favored design of a spirally-wound hemispherical boiler and a cylindrically-shaped receiver. The peak flux can obviously be reduced to acceptable levels by displacing the aim points of some heliostats, although this does increase the receiver size and the amount of bypassed flux. Also, the nominal design solar heat flux for the tower receiver is approximately an order of magnitude greater than the fluxes encountered in conventional steam boilers. Thus, design operating conditions and fabrication techniques for the receiver will necessarily depart from conventional practice. The generation of superheated steam by means of a thin-walled receiver of tubular construction, using technology garnered from aerospace research on rocket thrust chambers, has been suggested by Sobin et al. (22). This type of receiver, with either single-pass or helical-spiral tube arrangements, could readily handle the anticipated fluxes, and would be compact as well. An alternate design uses a liquid metal intermediate fluid which generates saturated steam (23). Liquid metals, such as sodium, are known to possess excellent heat transfer properties.

Yet another approach foresees a receiver constructed of open-ended ceramic cavities (24). Heat transfer is by impingement-jet techniques; the fluid is made to flow through a porous baffle plate and to impinge on the heated receiver surface. Heated air at ca. 1000°C is supplied to a regenerative Brayton cycle operating at a pressure ratio of four. The ceramic materials are resistant to the high temperatures encountered, permitting operation in an oxidizing

atmosphere at temperatures to ca. 1650°C. A quartz window over the flux-inlet side of the cavity offers no improvement in theoretical efficiency, when compared to a windowless cavity (25).

Tower costs are a function of both height (varying approximately as height squared) and receiver weight. A tapered free-standing concrete tower is the preferred choice for the heavier steam generating receivers; the lighter liquid metal or air cycle receivers can use a more economical guyed steel construction (19).

Heliostats must be individually controlled about two axes to maintain the solar flux on the receiver, adding appreciably to the cost and complexity of this design. Furthermore, the mean mirror utilization factor here is only ca. 0.70 (19). This includes the averaged effects of foreshortening or non-perpendicularity of mirrors to the solar flux (ca. 0.75), shading and blocking between adjacent mirrors (0.85-0.95), and bypassing the receiver (0.8-1.0). Easton et al. (26) developed a procedure for optimizing the energy collection portion of a central receiver power plant. Still, the low utilization factor for the heliostats largely offsets the material/cost savings that this design otherwise offers relative to a solar farm, since the mirror utilization factor can be significantly higher in the latter.

Wen and Wu (27) present a theoretical performance comparison between the central tower receiver system (solar tower) and a distributed system (solar farm - linear receiver). These systems were analyzed at a rated capacity of 30 MWth, delivered in the form of

superheated steam at 538°C and 68 atm. On an annual basis the boiler section (which provides 22.7 MWth at rated capacity) of a N-S trough collector has an energy performance factor of ca. 0.32 (where 1858 kWth-hr/m^2-yr = 1), a two-axis trough shows an improvement to ca. 0.51. A tower with a conical absorber achieves ca. 0.63, while the considerably more expensive (26) tilted cavity receiver manages ca. 0.85. These values are at reflector surface slope error = 0.20° and a pointing error of 0.16°, and decline with increasing errors. But the land utilization factor, defined as the ratio of the collector area to the land area, varies considerably with system employed. The central receiver system has a land utilization factor < 30%. Higher factors exist for the other types: 36% for the two-axis linear collectors, and 71% for a single-axis trough collector oriented N-S (27). These would tend to even out land requirements for a given capacity; reflector manufacturing costs, including the costs associated with tracking mechanisms, control, maintenance, and auxiliary components such as piping and insulation (linear systems) and tower construction (central receiver systems) must also be considered in a comprehensive total cost evaluation program.

A preliminary and rather simplified cost analysis and comparison of a distributed system with the central receiver is presented by Caputo and Truscello (28). The electrical energy cost is claimed to be 48 mills/kWe-hr in the case of the central receiver, and approximately double this for linear systems. It is not clear if

all the aforementioned factors influencing costs of these systems were taken into account here, but the inclusion of the linear collector capital cost at twice the central receiver collector cost (28) makes this doubtful. Clearly, although much work has recently been accomplished on solar thermal power systems, it appears that additional work is necessary before one system can be shown conclusively superior to others.

Sandia Laboratory, Albuquerque, NM, is currently overseeing construction and testing of a 91 m tower, with a field of 320 - 1.2 x 1.2 m heliostats. It is expected to yield steam at 1010°C, for a maximum output of ca. 5 MWth, thus making it the largest solar facility in the world (29). Its primary purpose is to test boiler designs and materials, mirrors, and other components for a 10 MW facility that has recently been approved for construction. The site for the larger plant, which will employ conventional steam generating equipment, is on 130 acres at Barstow, CA. The 10 MW plant is expected to be operational in 1980 or 1981.

D. Linear Radiation-Cavity Collector

Research at The Pennsylvania State University is aimed at developing a concentrator-collector of the solar farm type that is built of readily available materials, is simple in operation, and will heat a gas to fairly high temperatures (525-575°C) so it can move directly into a gas turbine in a closed-cycle Brayton scheme.

To this end, advantage is taken of the ability of a small aperture in the wall of a large cavity to act essentially as a blackbody; i.e., practically all the radiation incident upon it is absorbed (30). Palmer (31) and Palmer and Kuo (32) exploited this feature in a proposed modified solar farm concept, and also designed an Archimedes (i.e., Fresnel) mirror-concentrator to replace the more complex parabolic trough (see Figure 3). The mirror rotates about the collector pipe, which remains stationary and contains a thin slab of commercial graphite as flux absorber. In the original proposal (32) the individual mirror strips were rotated simulta-neously at varying rates, concomitant with rotation of the entire mirror array. In the present work a somewhat simpler tracking mechanism is employed.

The solar farm concept examined here was estimated to provide an output of 25 MWe from an area smaller than 1 km^2 (including the power plant), under what seemed to be realistic assumptions regarding losses and optical features (32). The total conversion efficiency, conservatively calculated relative to the solar flux at the top of the atmosphere, was found to be in the range from about 4.5-5.9%. Relative to the flux entering the collector, the efficiency was estimated to be from 12-14.5%.

E. The Purpose and Method of the Present Study

The writer believes that in the near future our society must develop and exploit power production methods such as those described
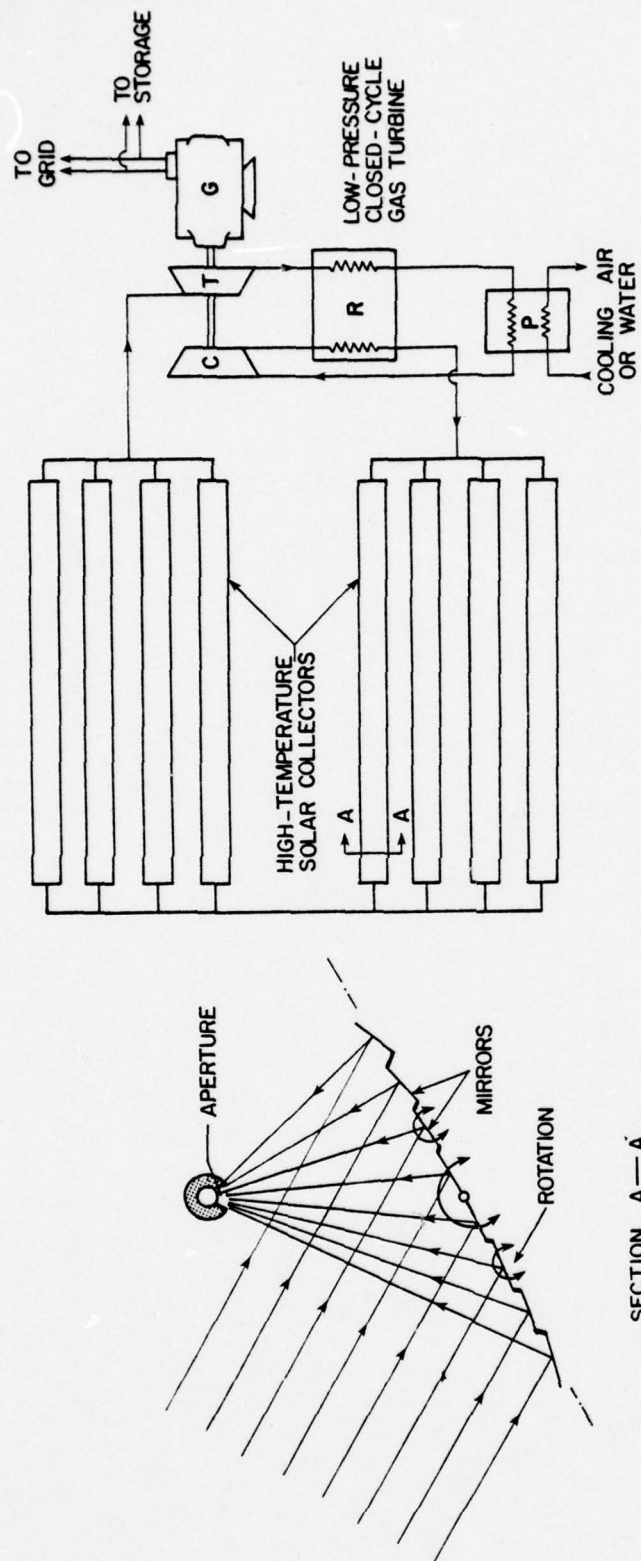
Figure 3. Radiation-cavity solar collector "farm." T, turbine; C, compressor; G, generator; R, regenerator; P, precooler.

above. However, choosing among the numerous methods proposed is

difficult. The criterion to be used is primarily one of cost,

which is inseparably linked with overall system size, complexity,

reliability, and efficiency. Idealized mathematical models of

proposed designs presented in the past and discussed above, with

simplistic experimental support (if any), preclude a rational selec-

tion process. Thus, experiments must be performed and realistic

models constructed to determine rather accurately the potential

efficiency of a full-scale version of a particular power-production

method.

To this end a somewhat simplified first model of the linear

cavity receiver design described in Section D, above, was built to

approximately 1:11 scale in cross section. Experience gained with

this first model (described in Chapter II) led to the design and

construction of a larger (1:6 scale), more realistic, and more

versatile second model, representing the full-scale device much more

closely. Detailed studies were performed (described in Chapter III)

on the temperature rise of the gas as a function of its flow rate

as it traverses the receiver pipe, and on the asymptotically

limiting gas temperature (i.e., stagnation temperature (1)) achiev-

able at a given solar flux level. Attendant computer modeling of

the experimental device yielded results in close agreement with

empirical (see Chapter IV), and provided confidence in developing

a computer model of the full-scale device (described in Chapter V).

This research indicates that the basic concept studied here has proven

sound, and reasonably efficient utilization of solar energy at high temperatures can be realized. Nevertheless, additional modeling, both empirical and theoretical, is in order (see Chapter VI) before a rigorously optimized large-scale solar farm of this type can be constructed.

CHAPTER II

FIRST EXPERIMENTAL MODEL (STATIC GAS)

A. Introduction

An experimental model of the full-scale design (see Chapter
V) was constructed at The Pennsylvania State University early in
1975. The cross-sectional scale factor was approximately 1:11.
The receiver aperture, which was not insulated in order to allow
the solar flux to enter the pipe, was proportionately much larger:
ca. 0.6 of the receiver pipe diameter versus 0.2 for the full-scale
device (see Figures 4-6). Insulation also was much thinner (Table 1),
so that conduction heat losses were relatively large. The short
length of the model introduced end effects - axial temperature
gradients - which channeled heat away from the center, lowering the
maximum temperature there.

B. Construction

The glass receiver tube was sealed (rounded) at one end and
capped at the other end with a Transite plug. This had two small
holes drilled through it (ca. 0.25 cm diameter) for thermocouple
insertion. Graphite absorber material was placed in the center of
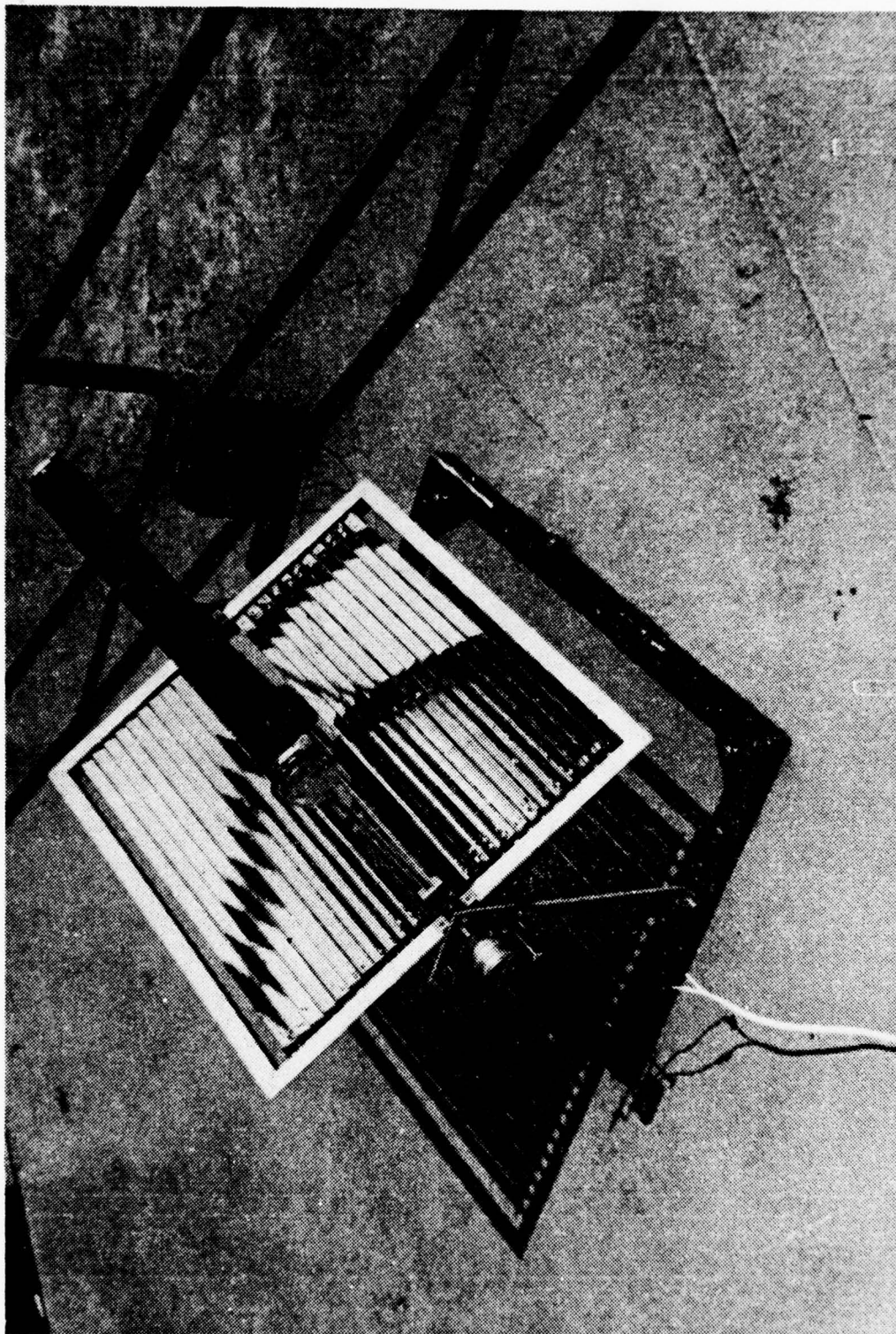
Figure 4. 1/11 Scale experimental model.
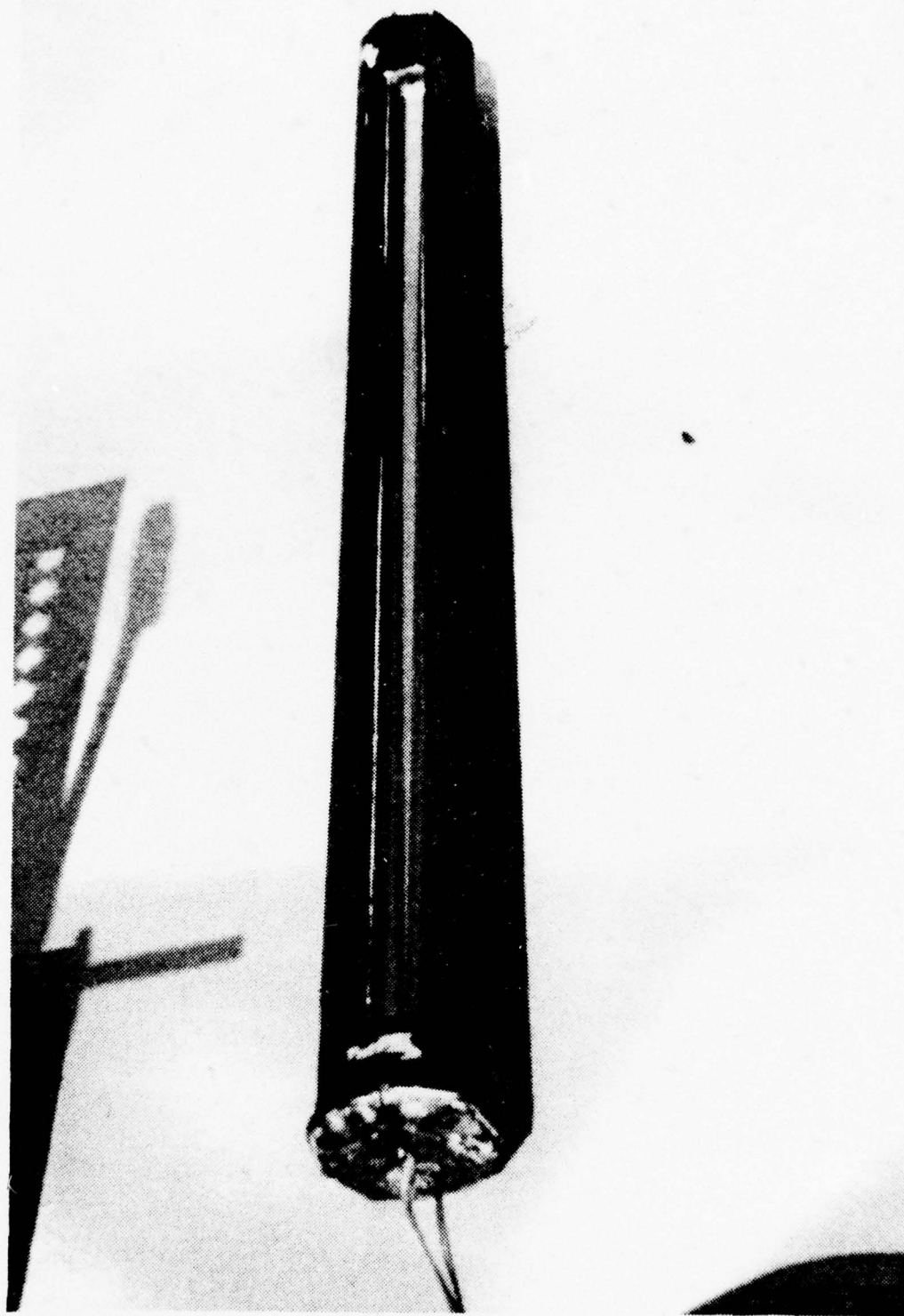
Figure 5. View into aperture.
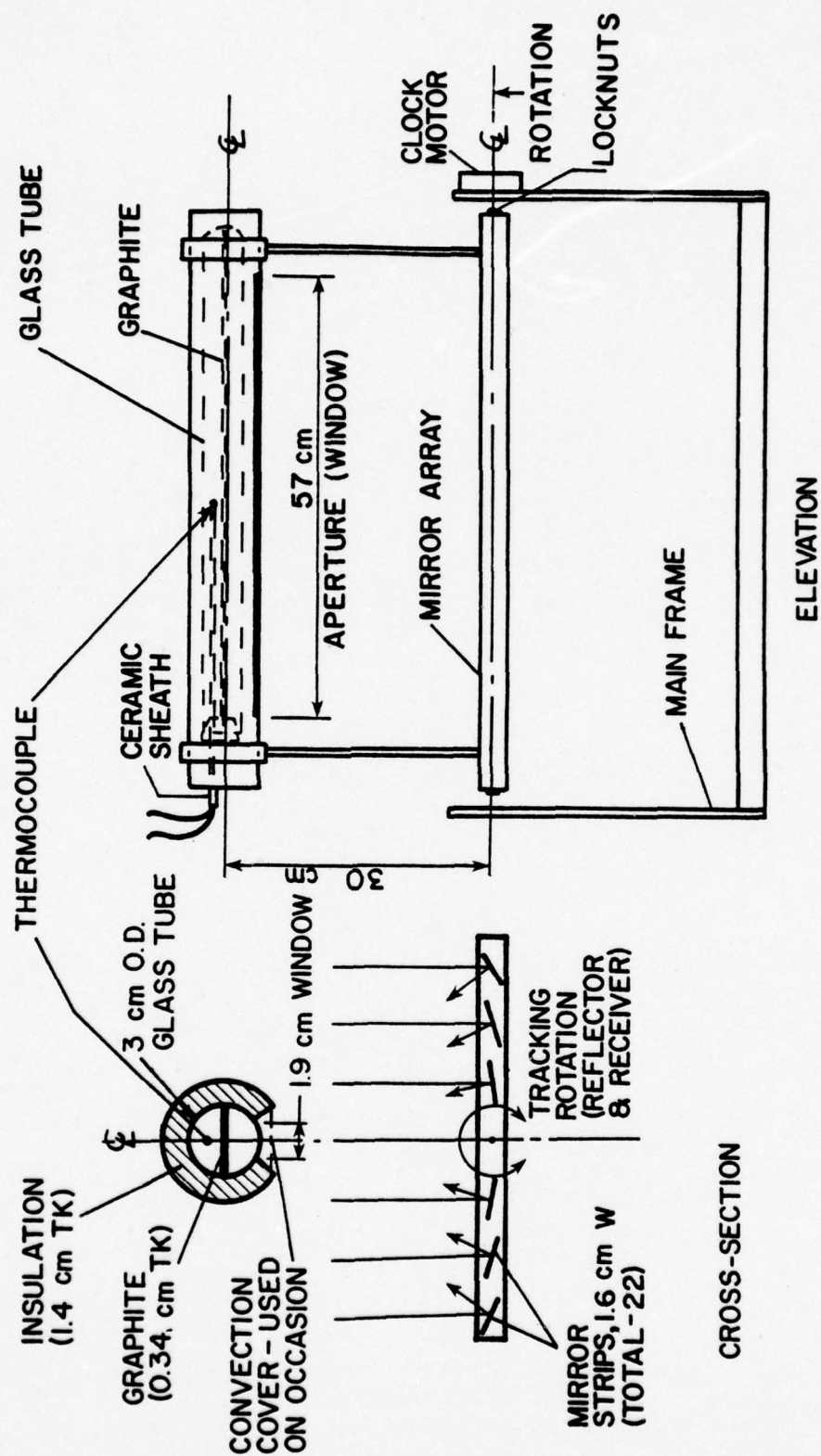
Figure 6. Main features of 1/11 scale experimental model.

Table 1. Materials description and properties.

_____

Receiver

  Absorber   Commercial graphite, 0.34 cm tk.

    $(\alpha_S)_{25°C}$ 0.87 (*see Chapter IV*)

  Pipe   Corning clear 1720 aluminosilicate
                                      glass

    $\varepsilon_{100°C}$ [34]   0.90
    $(\tau_S)_{25°C}$ [34]   0.91 (assumed same as 1723 glass:
                                      1720 glass not listed)

  Outside dia. x wall
    thickness   3.0 cm x ca. 0.1 cm

  Aperture L x W   57 cm x 1.9 cm (at the glass)
    Material   Johns-Manville Transite (i.e.,
                                      asbestos board)

    $\varepsilon_{100°C}$ 0.93 (see Chapter IV)

  Insulation   Carborundum Fiberfrax (bulk fiber)
    Thickness   1.4 cm (2.8 cm in some tests)
    $k_{100°C}$ [35]   ca. 3.8 W cm cm^{-2} °C^{-1}

Reflector

  Type   Archimedes
  Material   3-M back aluminized plastic
  Number of strips   22
  Strip dimensions   57 cm x 1.6 cm
  $(\rho_S)_{25°C}$ 0.67 (see Table 2 and Figure 7)

Miscellaneous

  Thermocouple   22 ga. Chromel-Alumel

  Temperature readout
    instrument   *Hoskins pyrometer, type AH*
  Heated medium   Atmospheric air

_____

Table 2. Reflectance of plastic mirror strip. Measured at 25°C with a Beckman DK-2A spectrore-flectometer (see Figure 7). A MgO reference standard was used, with ρ = 1.00 (see Chapter III).

λ, nm	Fraction solar energy in band (AM = 1.5)	Meas. ρ/MgO ρ	Diffuse reflectance component	Direct ρ component	Direct ρ x fraction solar energy
0 - 300	0	0	0	0	0
300 - 400	0.039	0.7 /0.9 =0.78	0.03	0.75	0.03
400 - 700	0.450	0.78/0.94=0.83	0.03	0.80	0.36
700 - 900	0.199	0.77/0.94=0.82	0.25	0.57	0.11
900 - 1600	0.223	0.85/1.0 =0.85	0.33	0.52	0.12
1600 - 2000	0.049	0.84/1.0 =0.84	0.32	0.52	0.03
2000 - 2500	0.028	0.7 /0.95=0.74	0.13	0.61	0.02
2500 - ∞	0.012	0.7 /0.95=0.74[a]	0.13[a]	0.60	0.01
	Σ = 1.000				Σ = $(\rho_S)_{25°C}$ = 0.67

[a] Extrapolated
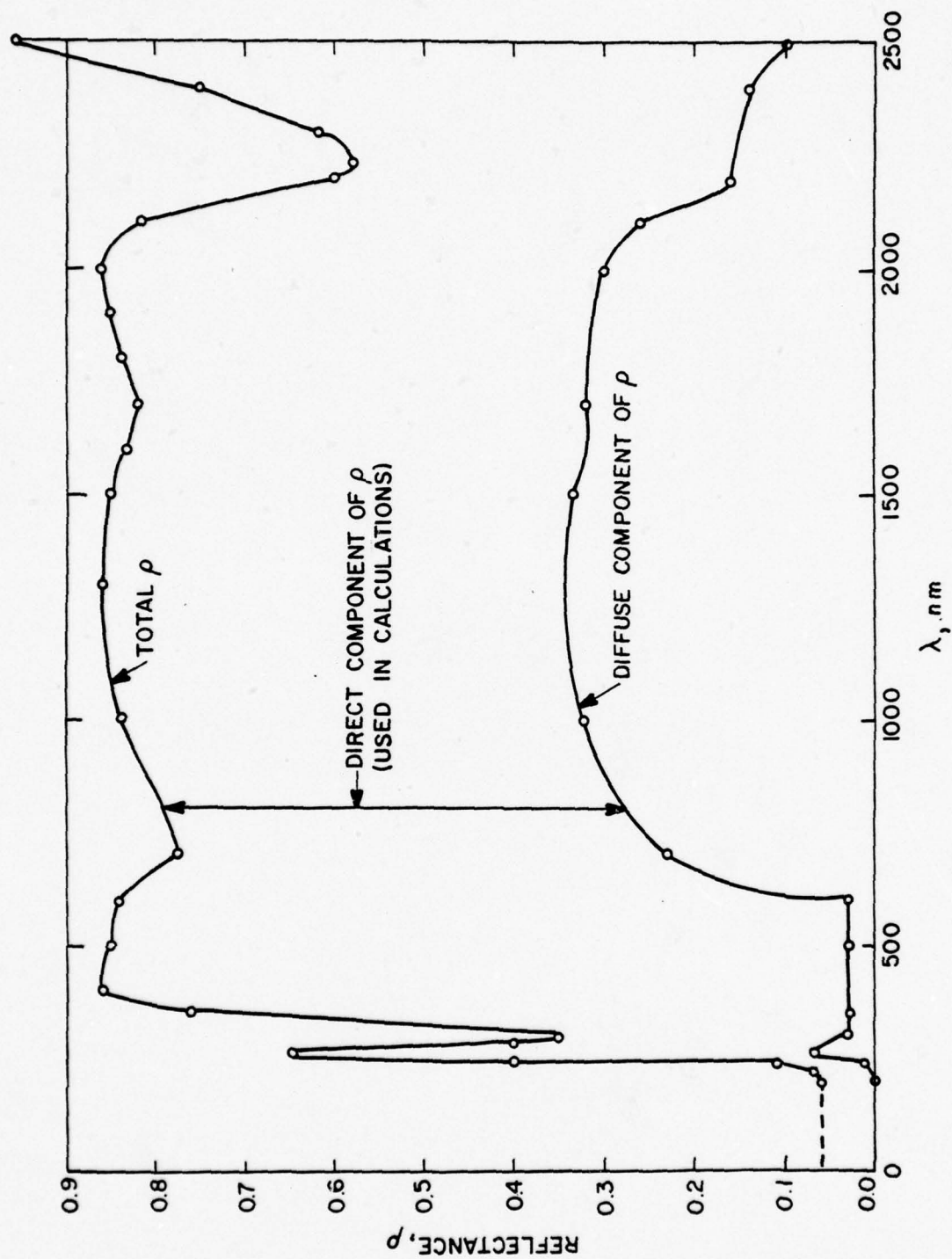
Figure 7. Reflectance of plastic mirror strip (measured).

the tube. A thin-walled outer fiberglass tube with a longitudinal
aperture supported the glass tube and its surrounding insulation;
the ends were well insulated also to minimize axial heat losses.

The mirror was made using reflective tape with an adhesive
backing, mounted on 0.3 cm thick Plexiglas support strips. Screws
and locknuts at the ends fastened the strips to an aluminum angle
frame; this frame also supported the receiver. A second metal
frame served as a base for the device.

Each mirror strip had to be individually aligned to correctly
reflect the solar beam onto the receiver aperture. The alignment
procedure was as follows:

(1) The receiver tube was placed in its holder over the
mirror array, with the aperture facing the central axis of the array.

(2) The mirror strips were rough-aligned by eye.

(3) The receiver was removed and a string placed where the
central axis of the aperture (in the plane of the glass window
surface) had previously been located.

(4) Two horizontal strings attached to heavy structures were
placed ca. 0.5 m apart vertically and aligned in a vertical plane by
means of a plumb bob.

(5) The device was placed under the two strings in such a
manner that these were centered over an individual strip (to be
aligned). The array was locked in a horizontal position.

(6) A sighting was then taken across the string which had replaced the aperture axis, toward the strip of interest.

(7) The strip was rotated until all three strings appeared to coincide along its longitudinal axis. After this was accomplished the locknuts holding the strip were tightened.

Some misalingment was present as a result of mirror strip flexure and waviness of the mirror surfaces. Hence, the actual width of the beam somewhat exceeded the 1.9 cm window aperture width: the measured beam width in the aperture plane was approximately 2.5 cm, a pointing error of about 32%. However, not all strips contributed equally to this error; it was chiefly produced by those strips farthest from the array center. Therefore, the true pointing error flux loss probably was significantly lower than the above value.

C. Experimental Method

The small experimental collector was placed on the roof of the Mineral Industries Building of The Pennsylvania State University, where it was tested approximately a dozen times in the period February-May, 1975 (Table 3). Bright, sunny days were chosen for the test runs. Tests generally lasted 1-2 hours near solar noon. The data collected consisted of temperature measurements of the still air within the collector. Orientation of the axis of the device was north-south (N-S). An electric clock motor was employed to rotate

Table 3. Experimental results.

Date	Comment	Asympt.T_g	T_∞	Total horiz. flux W m^{-2}	(c) δ,°	(d) $\psi-\delta$°	(g) Flux W m^{-2}	(e) H/H_o	(e) H_D/H	Direct flux, W m^{-2}	Environmental observations
2.II.75	Std. config.	200[f]	−2	488	−17	58	921	0.68	0.29	654	Slight haze, some wind
3.II.	Std. config.	245	0	648	−17	58	1223	0.90	0.2	978	Clear and windy
15.III.	Fogged[a]	210	0	864	− 3	44	1201	0.89	0.2	961	Some haze, windy
17.III.	2.8 cm insul.	249	+ 9	795	− 2	43	1087	0.80	0.22	848	Slight haze, calm
18.III.	2.8 cm insul.	241	9	822	− 2	43	1124	0.83	0.21	888	Some haze, windy
1.IV.	2.8 cm insul.	239	12	848	+ 4	37	1062	0.78	0.22	828	Some haze, windy
6.IV.	Std. config.	240	0	934	6	35	1140	0.84	0.21	901	Very clear, windy

Table 3. Continued.

Date	Comment	Asympt.T_g T_∞		Total horiz. flux W m^{-2}	(c) δ,°	(d) $\psi-\delta°$	(g) flux W m^{-2}	(e) H/H_o	(e) H_D/H	Direct flux W m^{-2}	Environmental observations
6.IV.	Cover[b]	251	0	934	6	35	1140	0.84	0.21	901	Very clear, windy
11.IV.	Std. config.	245	9	850	8	33	1014	0.75	0.23	781	Clear, little wind
11.IV.	Cover[b]	245	9	850	8	33	1014	0.75	0.23	781	Clear, little wind
28.V.	Std. Config.	258	25	955	21	20	1016	0.75	0.23	782	Very clear, some wind
28.V.75	Cover[b]	262	25	955	21	20	1016	0.75	0.23	782	Very clear, some wind

[a] Thin clear polyvinylidene chloride (Saran) cover over aperture.

[b] ca. 0.3 cm thick polymethyl methacrylate (Plexiglas) cover over aperture.

[c] δ = declination (i.e., angular position of the sun at solar noon with respect to the equator) north positive. Can be calculated by the approximate equation of Cooper (36), where $\delta = 23.5 \sin [360(284 + n)/365]$; n = day of the year.

$^d\psi$ = latitude (here, of State College, PA = 41°), north positive.

^{e}Ratios are used in determining the diffuse flux. See Chapter IV, Section B, for explanation.

^{f}Extrapolated; the measured temperature at the end of 1/2 hour (cloudy therafter) was 190°C (see Figure 9).

^{g}Total perpendicular flux.

the entire collector at 15°/h in order to track the sun. However, this motor often did not perform adequately, especially early in the year when the collector tilt from the horizontal (of the longitudinal axis, to correct for solar declination) was greatest. It was found easier to adjust the collector manually then, and thus maintain it normal to the incident solar rays, the preferred orientation of the collector axis being then an east-west (E-W) one. This orientation required fewer adjustments than the N-S, over a given time interval near solar noon. The thermocouple was normally placed in the upper semicircle of the receiver, opposite the aperture (see Figure 6).

The Pennsylvania State University Meteorological Observatory continuously measures the total solar insolation on a horizontal surface, with an Eppley pyranometer. For use in the experiments described herein, it was necessary to correct the insolation data for the solar angle from the vertical, and then to determine the direct component theoretically (see Chapter IV for a full discussion of the procedure).

D. Experimental Results (see Table 3)

Maximum (i.e., asymptotic) temperatures well in excess of 200°C were readily attained by the still air at the center of the receiver. A plot of these temperatures versus the direct solar flux incident on the concentrator (for a "standard configuration" without

extra insulation or convection covers) is shown in Figure 8. Some scatter is evident, but the trend toward higher asymptotic temperatures at higher flux levels is apparent.

While normally measurements were made of the temperature in the upper half of the receiver, placing the thermocouple in the lower half produced a gain of ca. 10°C. Most of this rise was no doubt caused by the solar flux now incident on the thermocouple itself. Other temperature measurements at several axial locations along the receiver indicated a temperature "droop" of ca. 70°C, as the ends were approached.

Figure 9 illustrates the time-dependent temperature variation and the fact that the asymptotic temperature was reached in approximately 50 minutes from the initial exposure of the device to the sun. Although for the test run illustrated a double thickness of insulation was used on the receiver, the results shown have a general validity. In every test run, irrespective of actual conditions of solar flux, insulation thickness, etc., asymptotic temperatures were attained in about 50 minutes.

Varying a number of experimental parameters had the following effects:

(1) Doubling the receiver insulation thickness, from 1.4 cm to 2.8 cm, resulted in a temperature increase of about 10°C. While the added insulation obviously reduced conduction losses somewhat, it also decreased the available flux by about 7%, since the extra insulation cast a larger shadow on the mirror-concentrator.
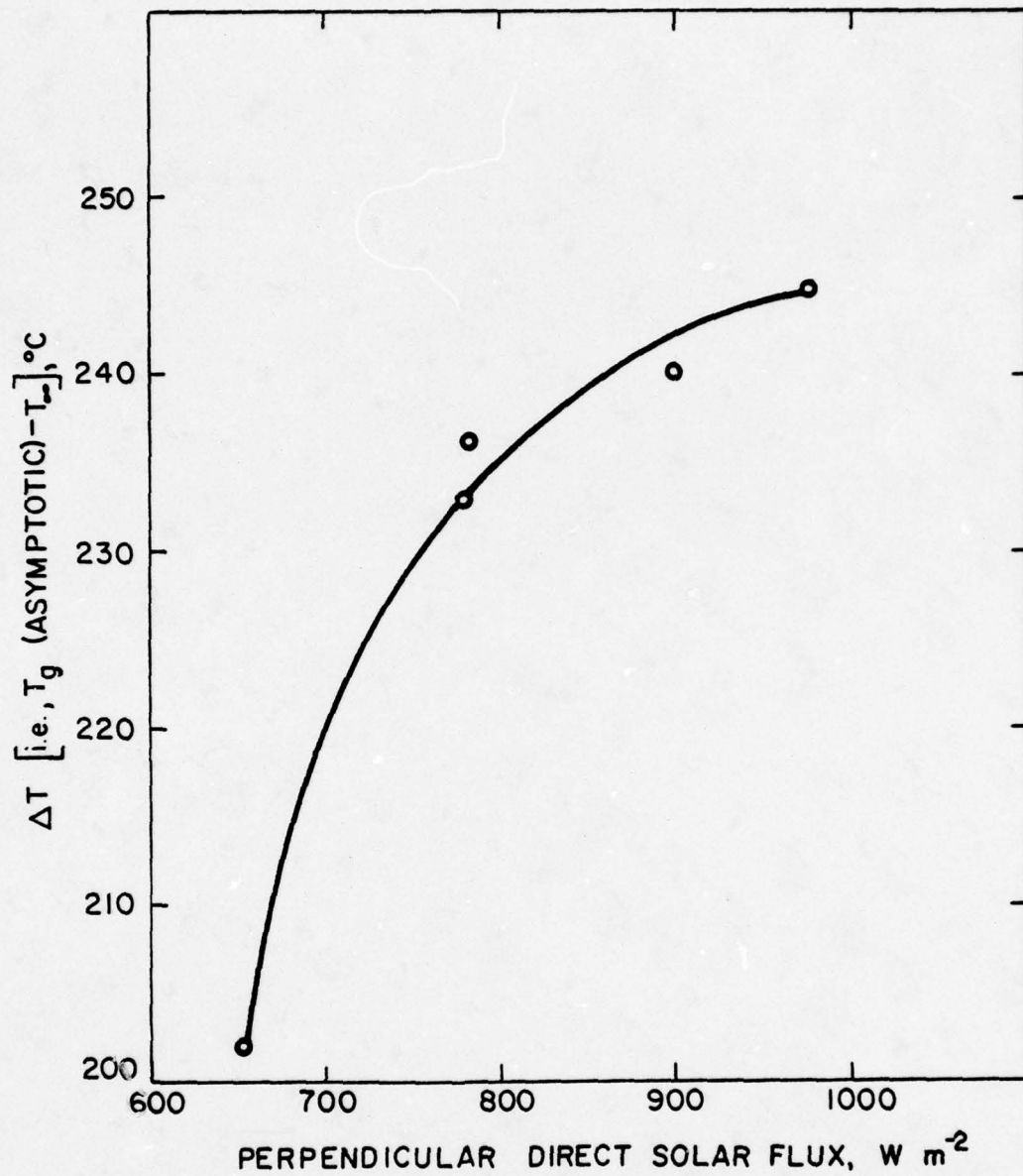
Figure 8.   Measured asymptotic temperature versus direct solar flux.
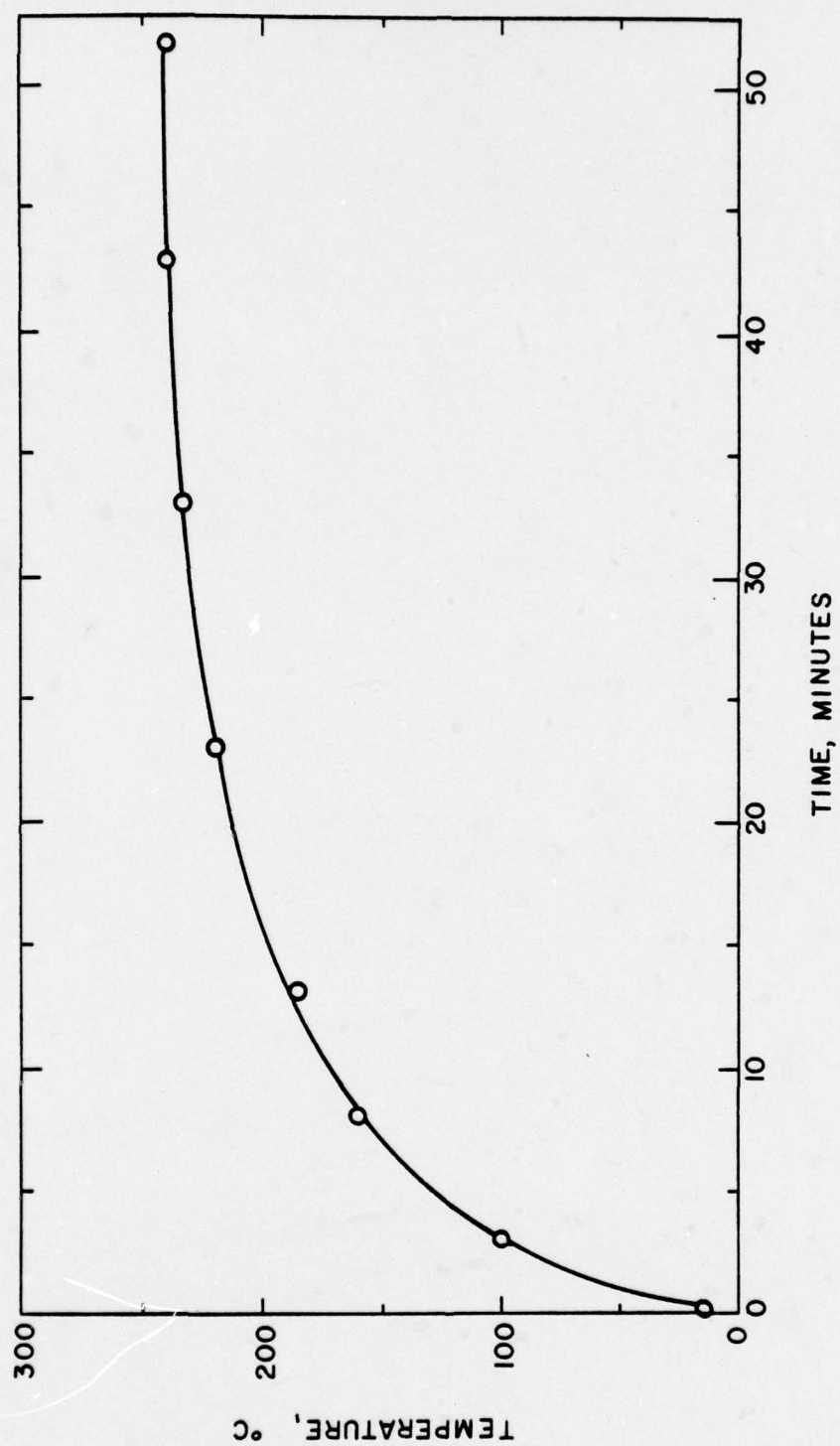
Figure 9. Time-dependent temperature response (measured).

(2) Sealing of the receiver-insulation aperture (see Figure 6) with a clear polymethyl methacrylate (Plexiglas) cover strip, ca. 0.3 cm thick, reduced convection losses and increased the asymptotic temperature by 0-10°C. The effectiveness of the cover in reducing convective losses appeared to depend on the wind velocity. Since the Plexiglas material grew quite warm and sagged considerably during testing, it seems that a significant amount of infrared flux was being absorbed. The I.R. spectrum of the material indicated high absorptance in a thickness of 0.15 cm, for $\lambda \geq 3$ μm (33). When a thin Saran film was placed over the aperture instead, severe fogging of the film occurred, and its use was discontinued after a brief trial.

E. Calculated Results

A direct perpendicular solar flux of 800 W m^{-2} s^{-1} is somewhat arbitrarily selected as a typical experimental condition from Figure 8. Thermal losses are assumed to consist only of radial ones, and any axial losses (end effects) are ignored here. The calculation is based on a 1 cm length of receiver (at its axial center) purely for ease in computation.

The total concentrated solar flux, per centimeter of receiver length is:

$$q_s = (\rho_M)(22 \text{ strips})(1.6 \text{ cm/strip})(1 \text{ cm length})$$

$$(10^{-4} \text{ m}^2 \text{ cm}^{-2})(800 \text{ W m}^{-2}) = 1.89 \text{ W}$$

At the steady-state (i.e., asymptotic) temperature the incoming flux is just balanced by the outgoing thermal losses. An energy balance is written:

$$q_S(1 - \gamma)(1 - F_3 \cdot \rho_G)(1 - \rho_P) = \epsilon_1 F_1 A_1 \sigma \cdot T_g^4 + \epsilon_2 F_2 A_2 \sigma \cdot \bar{T}_w^4$$

$$+ k \cdot \bar{A}_3(T_g - T_\infty)/(\text{insul.tk.}) + h \cdot A_4(T_g - T_\infty) \, ,$$

where the individual terms on the R.H.S. of the equation represent, respectively:

(1) radiative loss from the glass window, assumed to be at the temperature of the gas;

(2) radiative loss from the aperture sides (see Chapter IV for a discussion), at an assumed average wall temperature;

(3) conductive heat loss through the insulation (radial only), where the temperature of the insulation inside surface is taken $= T_g$;

(4) convective heat loss from the aperture (glass + sides), assumed to be at the same temperatures as in Items (1) and (2) above,

and the term on the L.H.S. is the flux actually available to the receiver. γ, the pointing error, is assumed to be equal to 0.5 of the excess beam spread at the aperture. Therefore, the pointing

error is set equal to 0.16 for the present calculation (see earlier discussion). Before the above equation can be solved, the various view factors (F's), the free convection coefficient (h), and the insulation area ($\bar{A}_3$) must be evaluated.

1. View Factors (F's)

The relevant receiver dimensions are shown in Figure 10. If one makes the assumption of two-dimensional radiative interchange, the "crossed-string" method (see Chapter IV for a full discussion) can be used to evaluate the required view factors. For a long enclosure (i.e., long relative to width),
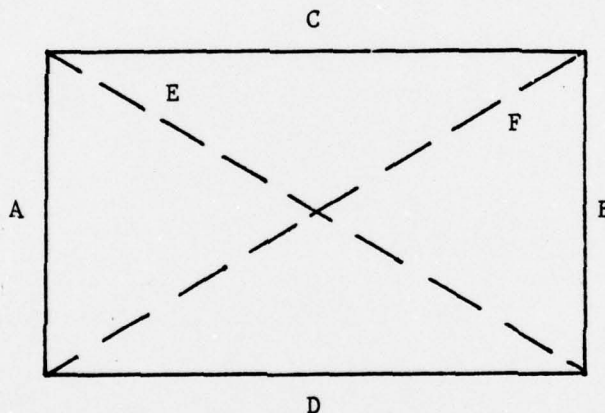
$$L_C F_{C-D} = [(L_E + L_F) - (L_A + L_B)]/2 ,$$

where L_A is the transverse length (width, actually) of side A, etc. as shown in the accompanying cross section of a long enclosure, and $L_A F_{A-D} = (L_A + L_D - L_E)/2$. Thus,

Figure 10. Receiver dimensions.

36

$$1.9 \cdot F_{Pyrex-Aperture} = [(2.7 + 2.7) - (1.3 + 1.3)]/2$$

$$\text{or } F_1 = 1.4/1.9 = 0.74 \ .$$

Similarly, $1.3 \cdot F_{Side-Aperture} = (1.3 + 3.5 - 2.7)/2 = F_2 = 0.81$, and

$$2.8 \cdot F_{Graphite-Aperture} = [(2.8 + 2.8) - (1.6 + 1.6)]/2 = F_3$$

$$= 0.43 \ .$$

(This slightly underestimates reflection loss from the graphite absorber; that loss is entirely diffuse and three-dimensional).

2. Free Convection Coefficient (h)

$h = f$ (Gr,Pr) in free convection. Equations are available for calculating h. First, however, Gr must be calculated to determine if the external flow past the aperture is laminar or turbulent (at an assumed wind velocity = 0). The relevant Grashof number is defined here as $Gr = (g \ \beta \ L^3 \ \Delta T)/2$, where $\Delta T = T_w - T_\infty$, and $L = z$, the axial length. Evaluation of the gas (air) properties at an average temperature $T_f = (T_w + T_\infty)/2$ corrects, with very little error, for the large ΔT (37). β is taken to be equal to $1/T_\infty$, although strictly speaking this is true only for an ideal gas; however, it is a reasonable approximation over the range $0.5 < T_w/T_\infty < 3.0$ (38). Assuming that the receiver (i.e., Pyrex + graphite + air) is isothermal radially, $T_g \simeq T_w \simeq 235°C$ at a flux of

800 W m^{-2} (see plot in Figure 8). Thus, if $T_\infty = 0°C$, then $T_w/T_\infty =$ $(273 + 235)/273 = 1.86 \rightarrow \beta = 1/273 = 3.66 \times 10^{-3}$ °K^{-1}, and $T_f =$ $(235 + 0)/2 = 118°C = 391°K$. At this T_f, ν air $\simeq 24.9 \times 10^{-6}$ m^2 s^{-1}, and $k_{air} \simeq 3.3 \times 10^{-2}$ W m^{-1} °K^{-1}, and Pr $\simeq 0.69$ (39). Therefore,

$$Gr = (9.8 \text{ m s}^{-2})(3.7 \times 10^{-3} \text{ °K}^{-1})(28.5 \text{ cm} \times 10^{-2} \text{ m cm}^{-1})^3$$

$$(235 - 0°K)/(24.9 \times 10^{-6} \text{ m}^2 \text{ s}^{-1})^2$$

$$= 3.18 \times 10^{-8} \text{ and the flow is laminar (40).}$$

For an inclined surface, the local Nusselt number Nu_z becomes

$$Nu_z = 0.508[Pr^2/(0.952 + Pr)]^{0.25} [(g \ \beta \ \Delta T \cos\alpha \ z^3)/\nu^2]^{0.25} \ (40),$$

where α = the angle from the vertical and is taken to be approximately 50°. Therefore, at the axial center of the device,

$$Nu_z = 0.508[0.69^2/(0.952 + 0.69)]^{0.25}[(9.8 \text{ m s}^{-2})$$

$$(3.66 \times 10^{-3} \text{ °C}^{-1})(235°C)(\cos 50°)(28.5 \text{ cm} \times 10^{-2} \text{ m cm}^{-1})^3/$$

$$(24.9 \times 10^{-6} \text{ m}^2 \text{ s}^{-1})^2]^{0.25}$$

$Nu_z = 44.5$, and since $Nu_z = h_z \cdot z/k \rightarrow h_z = Nu_z \cdot k/z$, and so

$h_z = (44.5)(3.3 \times 10^{-2} \text{ W m}^{-1} \text{ °K}^{-1})/(28.5 \times 10^{-2} \text{ m}) = 5.15 \text{ W m}^{-2} \text{ °K}^{-1}$.

3. Insulation Mean Area

For the insulation, $R_o/R_i = (1.5 \text{ cm} + 1.4 \text{ cm})/1.5 \text{ cm} = 1.93$; when this ratio is less than 2, the mean insulation area can be approximated with $A = (A_o + A_i)/2$ (Reference 40), and here $A_4 = \pi(5.8 + 3.0)\text{cm}^2/2 = 13.8 \text{ cm}^2$, for 360° coverage. Because the aperture occupies an approximate 75° sector, the correct area now becomes $A_4 = 13.8 \text{ cm}^2 (360° - 75°)/360° = 10.9 \text{ cm}^2$.

Upon substituting the above values into the energy equation, this now becomes

$$1.89(1 - 0.16)[1 - (0.43)(0.13)](1 - 0.09) \text{ W} \stackrel{?}{=}$$

$$0.9(0.74)(5.67 \times 10^{-8} \text{ W m}^{-2} \text{ °K}^{-4})$$

$$(235 + 273°\text{K})^4(1.9 \times 10^{-4} \text{ m}^2) + (0.93)(0.81)$$

$$(5.67 \times 10^{-8} \text{ W m}^{-2} \text{ °K}^{-4})(235/2 + 273°\text{K})^4(2.6 \times 10^{-4}\text{m}^2)$$

$$+ (3.8 \times 10^{-4} \text{ W cm}^{-1} \text{ °C}^{-1})(10.9 \text{ cm}^2)(235°\text{C})/1.4 \text{ cm}$$

$$+ (5.15 \text{ W m}^{-2} \text{ °K}^{-1})[(1.9 \text{ cm}^2)(235°\text{C}) +$$

$$(2.6 \text{ cm}^2)(235/2 \text{ °C})](10^{-4} \text{ m}^2 \text{ cm}^{-2})$$

or

$$1.36 \text{ W} \overset{?}{=} (0.478 + 0.258 + 0.695 + 0.387) \text{ W}$$

$$\neq 1.82 \text{ W} .$$

Clearly, the assumptions of radial isothermicity, and of skin temperature = T_∞ are overly conservative. It will now be assumed that:

(1) T_{skin} (which is the insulation exterior temperature, T_e) = T_∞ + 50°C. This was not measured, but the outside of the insulation felt warm (i.e., the temperature there was > body temperature, ca. 37°C).

(2) $T_p = T_g$ over the insulated portion of the pipe; at the window, $T_p = T_g$ - 50°C (not measured).

Now using T_g = 235°C, as before, and combining some of the constants, the energy equation becomes:

$$1.36 \overset{?}{=} (7.17 \times 10^{-12})(235 - 50 + 273)^4 + (1.11 \times 10^{-11})$$

$$[(235 - 50 + 50)/2 + 273]^4 + (2.96 \times 10^{-3})(235 - 50)$$

$$+ (5.15 \times 10^{-4})^a \{(1.9)(235 - 50 - 0) + (2.6)[(235 - 50 + 50)/2 - 0]\}.$$

a: h varies little with temperature and has not been recalculated. Its accuracy is at any rate probably no better than ± 20% (40).

$$1.36 \text{ W} \overset{?}{=} 0.32 + 0.26 + 0.55 + 0.34 \rightarrow 1.36 \text{ W} \approx 1.46 \text{ W} .$$

The result is acceptable, considering the assumed radial temperature distributions, pointing error, and the neglect of axial losses. The device could be more rigorously modeled, but since it was only the precursor of the desired larger, flowing-gas experimental model this was not undertaken. The first model served its purpose in verifying the flux-collection potential of the cavity receiver design. Furthermore, the chief heat loss terms had been identified and adequately characterized.

F. Conclusions

This first experimental model showed that moderately high temperatures were achievable, even with a very small version of the proposed design. The combination of experiments and calculations indicated that:

(1) The dominant loss was through the insulation, so this would have to be thicker in the next model.

(2) The radiation from the glass window was large and might become the largest loss term at higher temperatures. It would be best to keep the aperture as narrow as possible.

(3) The convective loss from the aperture was also large and presented the greatest uncertainty in calculations. Wind speed and

direction, aperture shape, collector tilt, and the amount of receiver rotation affect the magnitude of the loss by this mode. It is difficult to quantify the influence exerted by these parameters.

On the basis of the above, it was decided that the next model should be of approximately 1:6 scale, with a receiver ca. 6 cm in diameter, an aperture no wider than 2 cm at the glass pipe, ca. 2.5 cm of insulation, and a reflector of 40 x 1.6 cm-wide mirror strips. Very simplified calculations with these parameters indicated that an asymptotic temperature of ca. 400°C could be expected. For a receiver ca. 1.5 m long, one should attain a sufficiently steep axial temperature gradient for detailed study of heat transfer and collector thermal efficiency. Studies should be carried out at steady-state, at various laminar flow rates.

CHAPTER III

SECOND EXPERIMENTAL MODEL (FLOWING GAS)

A. Introduction

Work with the small model discussed in Chapter II provided guidance in design of the second experimental device. It was clear that the model should be substantially larger in cross section in order to more closely simulate a full-scale system and in order to reduce heat loss by conduction through the insulation. Restrictions on available space for installation, finances, and facilities for fabrication suggested that a reasonable size for the receiver pipe would be about 5 cm I.D. with a length of about two meters. The system should be designed for both flowing-gas and static-gas conditions. Also, provision for gas preheating should be incorporated into the system. The Archimedes mirror-concentrator should be more rigidly constructed and should have a reliable sun-tracking mechanism. Measurements on the system should at least include incident solar flux, flow rates, and the temperature distributions along the length of the graphite absorber, the gas, and the external surface of the glass. Information on optical properties of all materials, mirror reflectance, and thermal conductivity of the

insulation should be available either from the manufacturer, the literature, or by measurement.

The various measurements and information on properties should then permit development of a reliable mathematical model for describing the performance of the device, and subsequently, of the full-scale design. The mathematical model would serve to extend the necessarily limited scope of experimental study and allow general conclusions to be drawn.

Clearly, the most tractable formulation of the mathematical model would be for the case of turbulent fluid flow in the receiver. In that case, forced convective heat transfer would prevail over all other modes of internal heat transfer, and radial temperature gradients would be sufficiently small to be of no consequence. However, the difficulty in achieving fully turbulent flow (Re > 10^4 (41)) within such a small device precluded this approach. Very high flow rates, with a large and expensive pump, would have been required. Furthermore, turbulent flow would produce a rather flat axial bulk temperature profile, undesirable for the elucidation of the effects of various experimental parameters to which the profile should be sensitive.

Hence, although it was anticipated that analytical modeling would be more difficult for the laminar flow case than for fully developed turbulence, it was decided to perform experiments over the laminar flow range only, the pump and recirculating lines being sized accordingly.

B. Construction

Approximately one year (July, 1975–August, 1976) was required for construction of the model; the elapsed time covers the stages of preliminary design to completion of shake-down runs and modifications. In constructing the model, costs and other constraints led to the selection of readily available items and materials over more exotic articles.

The model has been designed to one-sixth scale (in cross section) relative to a system considered to be of practical dimensions for power generation (32). The solar-thermal concentrator-collector uses an Archimedes (i.e., Fresnel) mirror concentrator, 5 cm I.D. x 1.5 m long glass pipe receiver, 0.34 cm thick graphite absorber, and gaseous (Ar) heat transfer medium. An alternative 0.09 cm thick copper absorber with a selective oxide surface has also been employed. The absorbers were constructed slightly narrower than the pipe I.D., and simply rested within it; axial support was provided by a metal plate, of the same thickness as the absorber, which extended the length of the lower (i.e., inlet) end piece. Tabs on the plate kept the absorber immobile.

The mirror-concentrator consists of 40 suitably tilted reflective strips, each 1.6 cm wide by 1.5 m long; the strips are mounted with a flexible adhesive on metal support angles in a parallel planar array that travels E-W within two 1.67 m diameter tracks located near its ends. The glass receiver pipe holds the thin

material that absorbs the concentrated radiation focused on it and
transfers it as thermal energy to the flowing gas, which exits at
high temperature. The insulation (2.5 cm thick) surrounding the
pipe, except for a narrow (2 cm wide) longitudinal aperture, is
housed within a thin-walled metal tube which is attached to the
mirror array with angles. Thus, the insulation rotates in such a
manner as to always maintain alignment between the aperture and the
tracking concentrator. This last feature is one of the major strong
points of the design, since it obviates the need to rotate the
receiver pipe. Also, the small size of the aperture and internalized
flux absorption and heat transfer within the cavity receiver reduce
thermal and radiative losses substantially. A 0.25 mil (Mylar)
film over the aperture suppresses convective losses (see Figures
11-18 and Table 4).

The concentrator-collector assembly is tilted 41 degrees (the
latitude of State College, PA) from the horizontal so that the axis
of the collector is parallel to the earth's rotational axis, when
the device is oriented N-S. Mirror array tracking (and rotation
of the receiver insulation) is by means of a very accurate device,
a high-torque stepping motor which takes 400 steps/revolution. This
motor is connected through a chain drive to the array; a 30:1 reduc-
tion worm/worm gear combination multiplies torque and inhibits array
motion with the motor stopped. Control (no feedback loop) is by a
continuously variable solid-state timing circuit.

Figure 11. 1/6 Scale experimental model - side elevation.
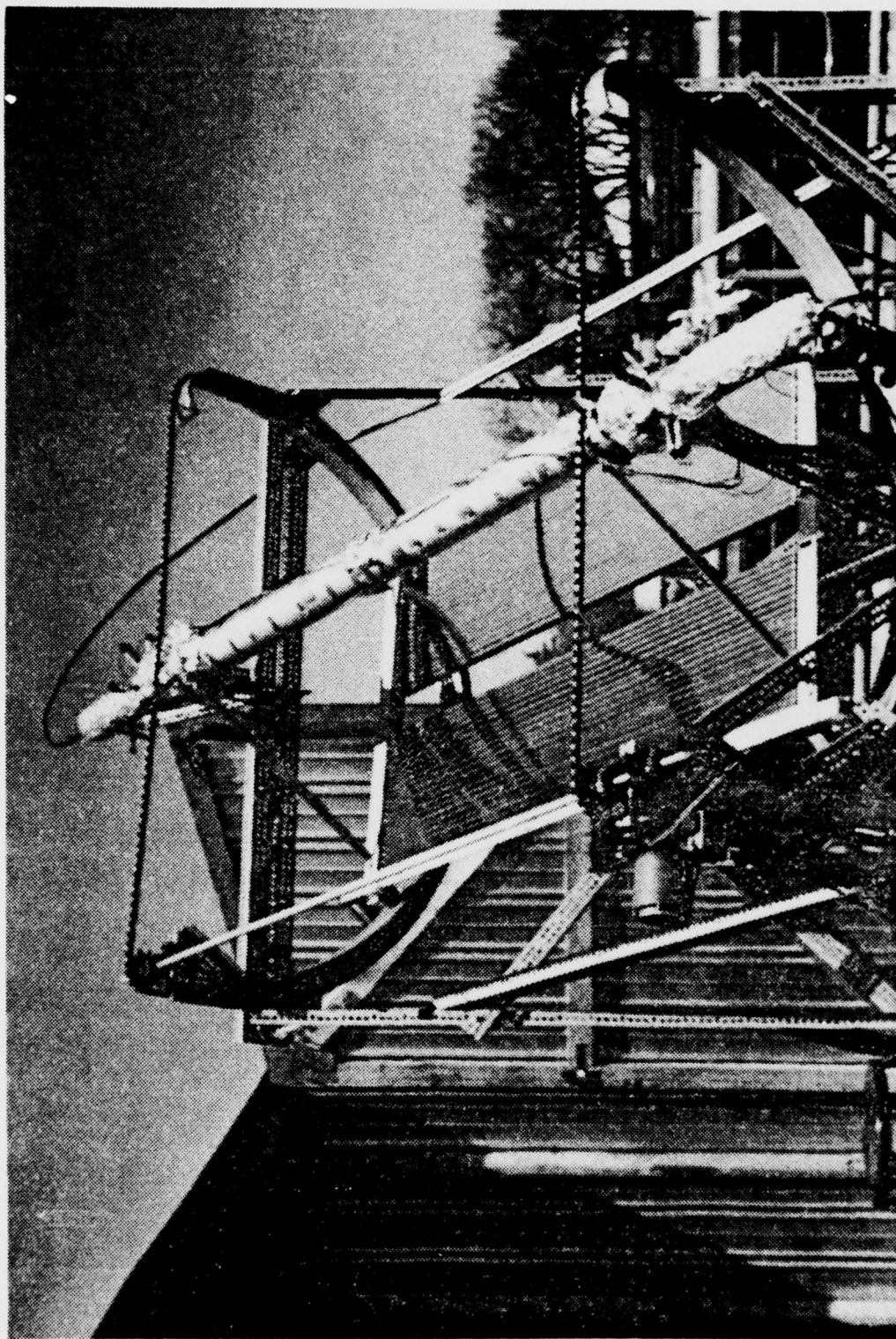
Figure 12. 1/6 Scale experimental model - front elevation.
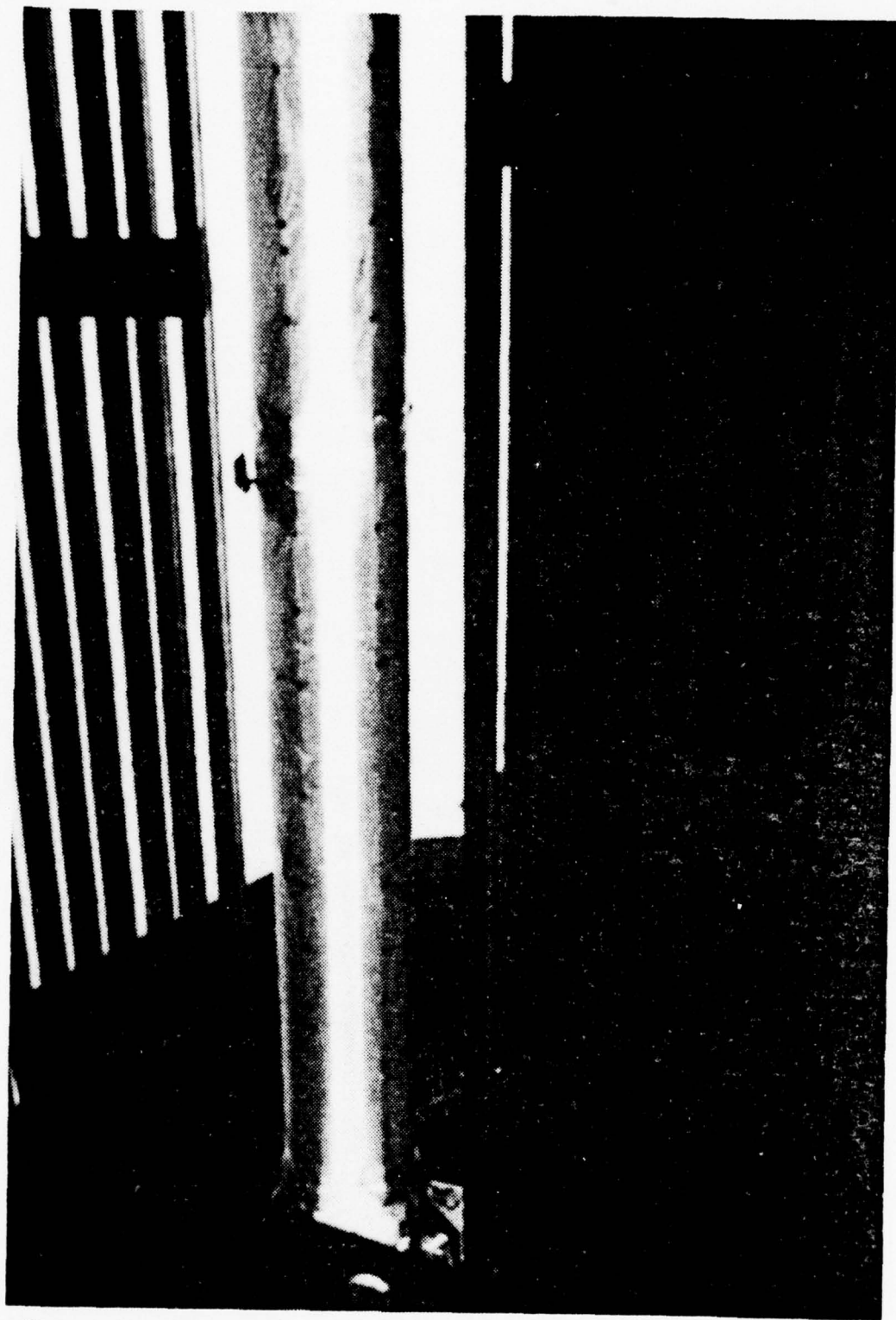
Figure 13. View into aperture.
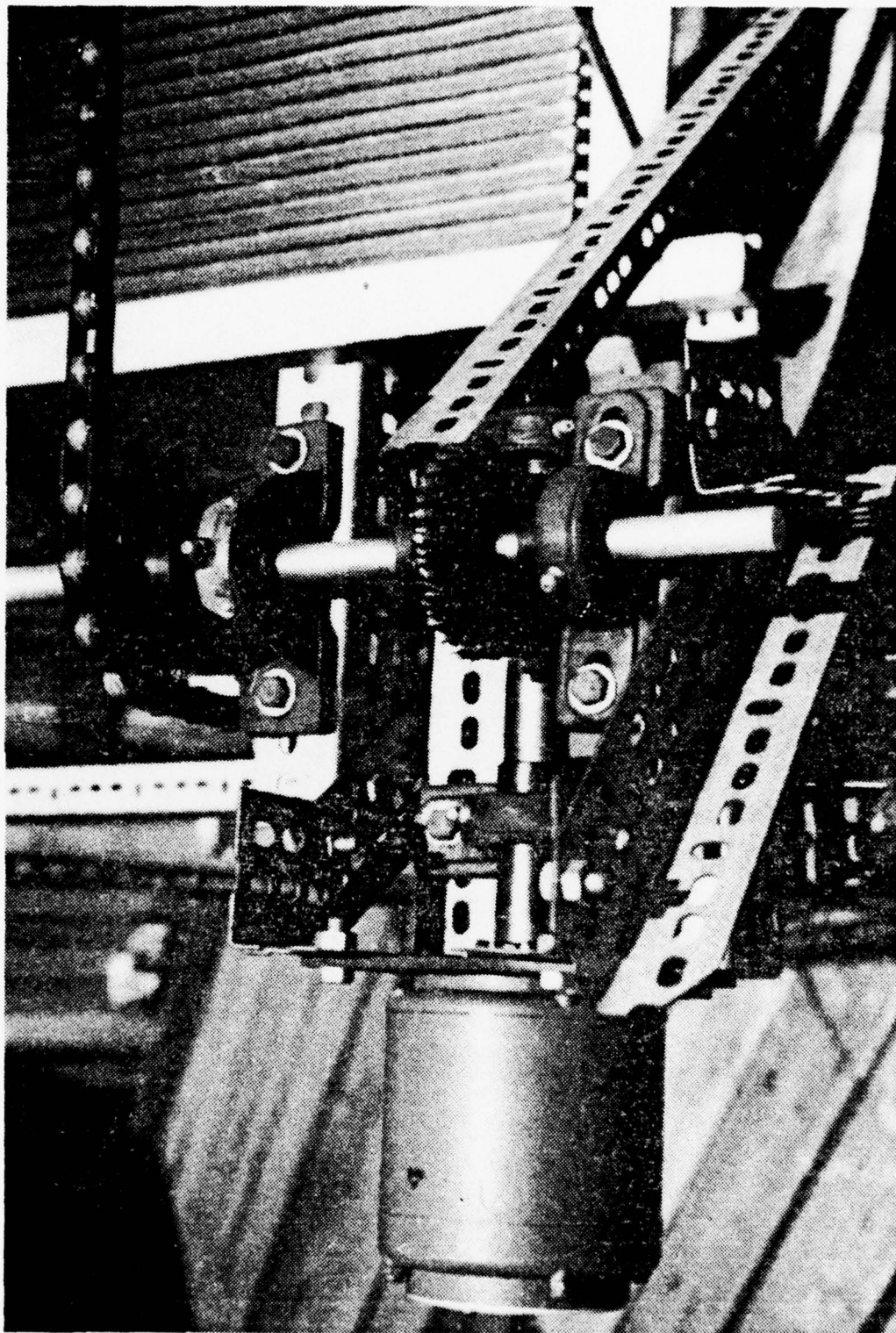
Figure 14. Drive detail.
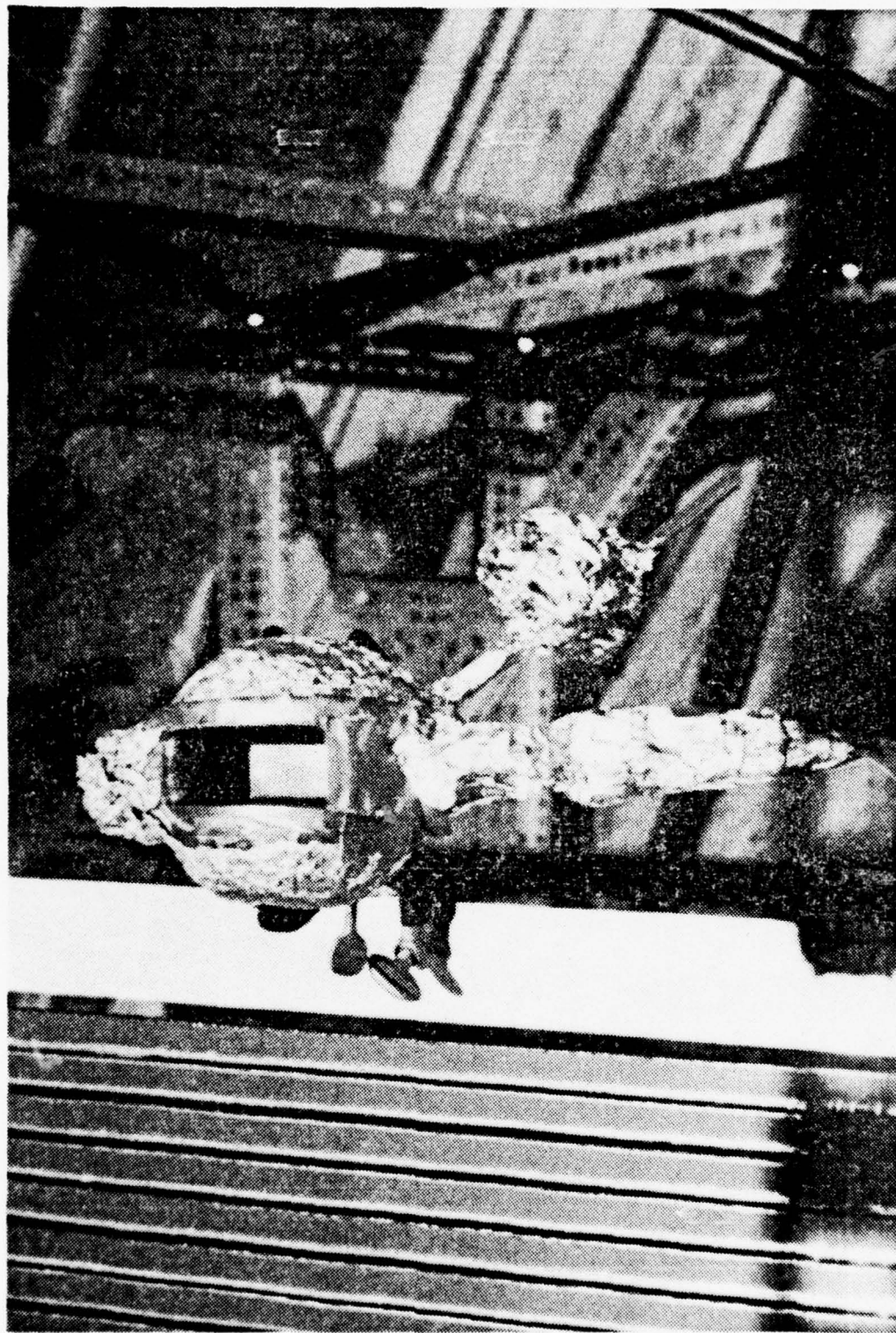
Figure 15. Flux bulb.
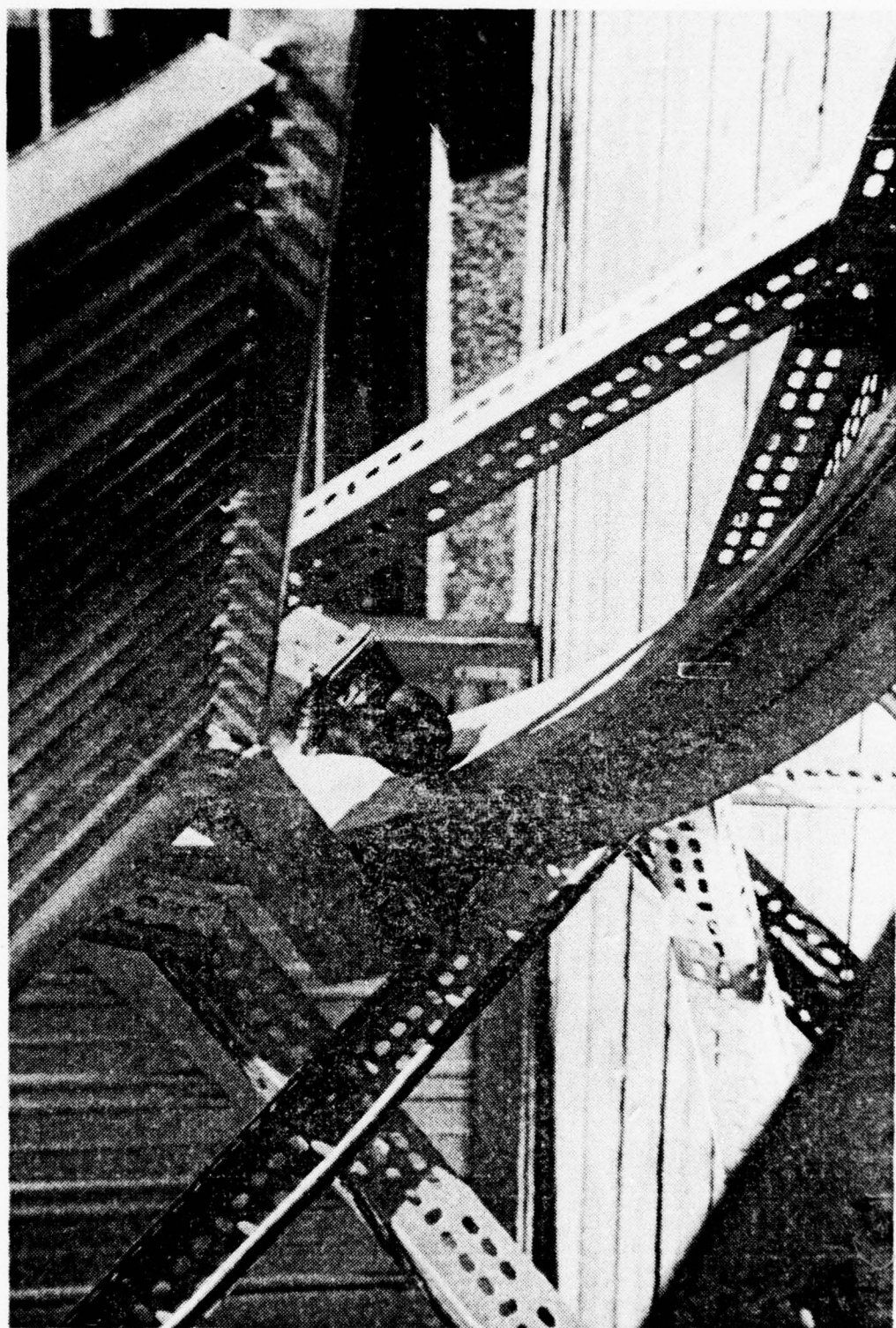
Figure 16. Wheels/track detail.
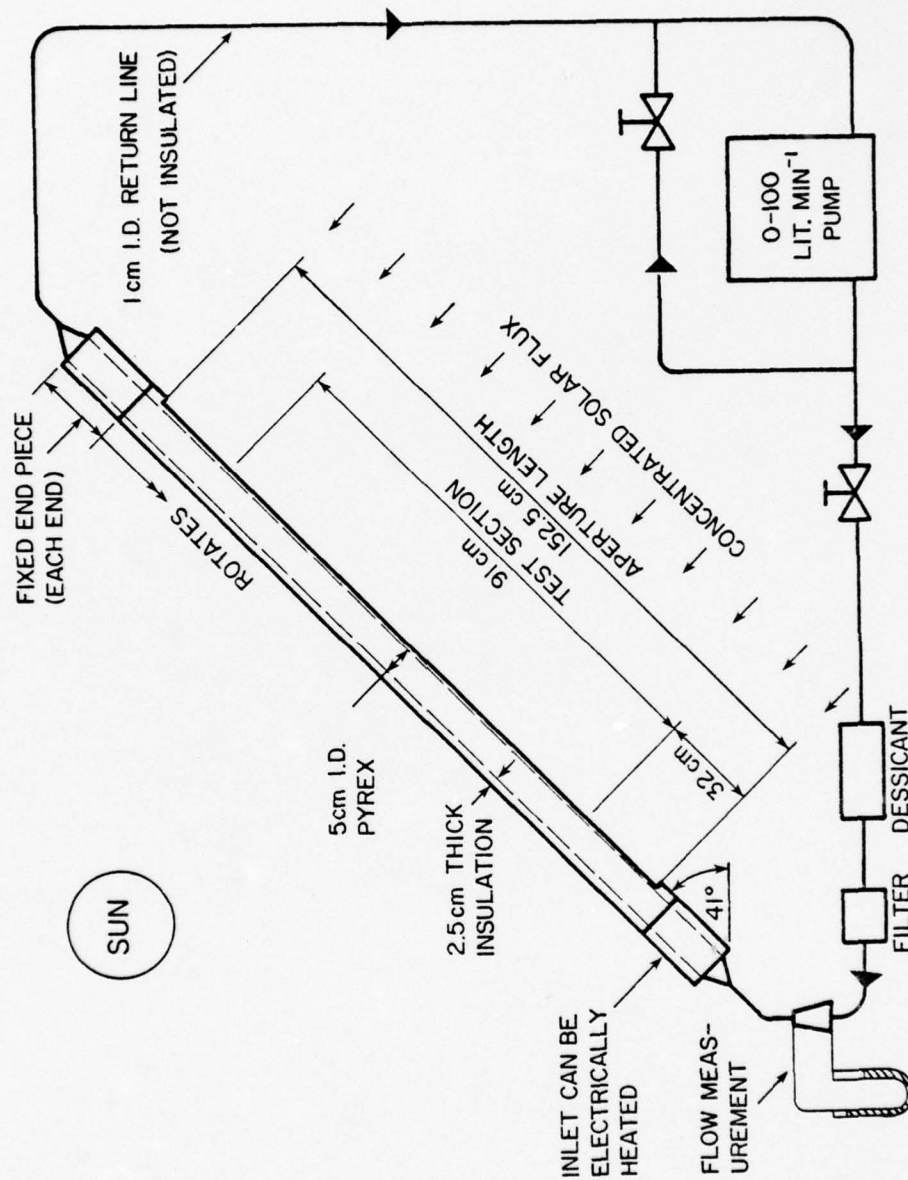
Figure 17. Equipment schematic
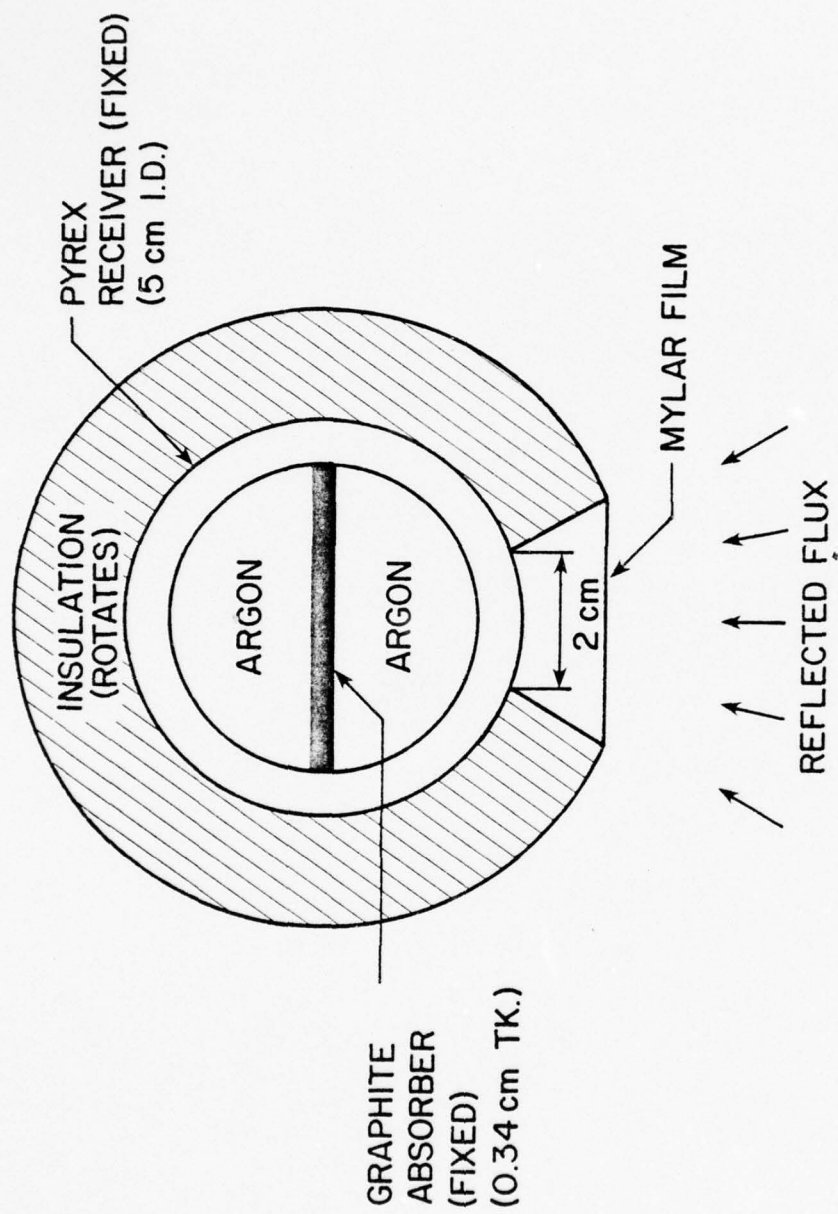
Figure 18. Receiver cross section.

Table 4. Materials description and properties.

_____

<u>Receiver</u>

Glass tube   Corning type 7740 clear
                                          borosilicate (Pyrex), with
                                          conical ends

  Size   50 mm I.D. x 5 mm wall x 1829 mm
                                          long

  Code   #72-7502

  $k_{25°C}$ (42)   1.09 W m^{-1} °K^{-1}

  $(\tau_S)_{25°C}$ 0.85[a]

  $\epsilon_{250°C}$ 1.00[b]

Flanges   Aluminum alloy, two required

  Size   50 mm

  Code   Corning #72-9062

Flange inserts   Hard, bonded asbestos, two required

  Size   50 mm

  Code   Corning #72-9058

Gaskets (standard)   Asbestos type A, two required

  Size   50 mm

  Code   Corning #72-9130

Gaskets (high temp.)   Silicone rubber

  Thickness   0.3 cm

Insulation   Carborundum ceramic fiber
                                          (Fiberfrax) blanket

  Size   2.5 cm x 96.1 kg m^{-3}

  Amount used   ca. 1 m^2

  $k_{100°C}$ (35,43)   3.8 W cm m^{-2} °C^{-1}

  $(\rho_S)_{25°C}$ ca. 1.00[a]

Insulation support tube   Aluminum

  Size   11.4 cm O.D. x 0.09 cm wall

Aperture L x W   152.5 cm x 2 cm

  Sides   Johns-Manville Transite (i.e.,
                                          asbestos board)

Table 4. Continued.

<u>Receiver</u>

Thickness	0.32 cm
$\epsilon_{200°C}$ (44)	0.94[b]
End pieces	Copper (outlet); st. stl. (inlet)
Size	ca. 5 cm O.D. x 0.15 cm wall x 46 cm long
Absorber support (inlet only)	0.34 cm thick stainless steel with tabs
Convective cover	DuPont Mylar
Thickness	0.25 mil
$(\tau_S)_{25°C}$	0.85[a]
Absorber (standard) (45)	Airco-Speer mold-stock graphite, commercial 787G Grade
$(\rho_S)_{25°C}$	0.13[a] (nearly 100% diffuse)
$(\alpha_S)_{25°C}$	1 - 0.13 = 0.87
$\epsilon_{250°C}$	0.87[b]
$k_{150°C}$	173 W m^{-1} °C^{-1} (with grain)[b]
Absorber (selective)	
Substrate material	Commercial copper
Thickness	0.09 cm
Selective surface	Cu_2O + CuO
Thickness	Not known
$(\rho_S)_{25°C}$	0.11[a]
$(\alpha_S)_{25°C}$	1 - 0.11 = 0.89
α_{IR} (46)	0.20
Pre-heat (inlet)	Heating tape (electrical resistance)
Catalog no.	Fisher Scientific #11-463-51D
Capacity	768 W
Size	2.5 cm x 244 cm
Control	Variac

Table 4. Continued.

<u>Receiver</u>

Heat transfer fluid	Argon
Purity	Standard commercial grade
Thermocouples (external)	Type K
Material	Chromel-Alumel
Gauge	28
Thermocouples (internal)	Type K
Material	Chromel-Alumel
Sheath	Stainless steel, 0.16 cm O.D.
Type	Omega Engineering Cat. No. CASS-116G and CASS-116E
Compression fitting	Omega Cat. No. BRLK-116
Thermocouple switching	2 rotary, 1 toggle, std. commercial

<u>Temperature readout instrument</u>
  (dial) — Hoskins

Type	AH
Accuracy	Note (b)
Internal resistance	50 ohm

<u>Temperature readout instrument</u>
  (digital) — Precision Digital Corporation

Model No.	7701-K
Accuracy (rated)	$\pm\ 2^\circ C^b$
Resolution-repeatability	$1^\circ C$
Lead resistance	To 1000 ohm for $< 1^\circ C$ error

<u>Reflector - concentrator</u>

Mirror	PPG back-silvered float glass
Size	1.6 cm x 153 cm x 0.32 cm tk.
Number	40
$(\rho_S)_{25^\circ C}$	0.80^a, direct only

Table 4. Continued.

Reflector - concentrator

Supports	2.5 cm x 1.3 cm x 0.3 cm tk. Al angles
Mounting	Screws and locknuts
Adhesive	Silicone sealant
Array frame	Aluminum angle
Size	5 cm x 5 cm x 0.8 cm tk.
Wheels	5 cm dia. Bassick #9389 casters

Track

	Aluminum tee, two required
Size	10 cm x 7.6 cm x 1.0 cm tk.
Dia. (rolled to)	1.67 m

Main frame

	Slotted steel angle
Size	5.7 cm x 3.8 cm x 0.16 cm tk.
Length required	ca. 60 m
Wheels	7.5 cm dia. Bassick #3619 casters

Tracking

Motor	Superior Electric Company stepping motor
Type	#M111-FD327, capable of 200 or 400 steps/revolution
Torque	28.8 kp cm at slow stepping speed and for 400 steps/rev (i.e., 0.9°/step)
Motor control	Superior Electric Company, solid state
Type	#STM1800DV translator module; also RC timing pulse circuit
Drivetrain	
Sprockets	Boston Gear No. 80, steel, two required
Size	2.5 cm pitch, 12 tooth
Shaft	1.9 cm dia. x 2 m long aluminum, with 1.6 cm dia. ends

Table 4. Continued.

<u>Tracking</u>

Bearings	Boston Gear Cat. No. 06904-3H ball brg. pillow blocks, 1.6 cm bore, 5 required
Chain	Boston Cat. No. C2042D, 2.5 cm pitch
Type	Roller, with oversize Delrin rollers
Gears	
Worm gear	Boston Cat. No. G1061 cast iron, 30 tooth, R.H. thread
Worm	Boston Cat. No. GH1066 soft steel

<u>Fluid flow system</u>

Pump	Graphite vane, centrifugal
Type	Gast model #0522-V103-G18D oil-less
Capacity	ca. 100 liters/minute
Max. press. (gauge)	ca. 1 atm.
Motor size	1/4 HP
Return line	ca. 1 cm dia. copper
Flow measurement	ca. 2.5 cm dia. constricting to ca. 0.5 cm dia. nozzle
Manometer fluids	
Absolute pressure	Hg
Nozzle ΔP	n-butyl phthalate ($\rho_{25°C} = 1.042$ g cm^{-3})
Filter	Whatman Gamma-12 unit with R40 - 2 μm filter tube
Dessicant	CaSO$_4$

<u>Flux measuring device</u>

Bulb	1 mm thick Pyrex
$(\tau_S)_{25°C}$	0.91
Absorber	10 cm^2 copper plate

Table 4. Continued.

<u>Flux measuring device</u>

$(\alpha_S)_{25°C}$	0.39^a
$\varepsilon_{25°C}$ (47)	0.03
Support rod	0.208 dia. x 10.3 cm long copper
$k_{25°C}$ (48)	3.89 W cm^{-1} °C^{-1}

[a]Measured here
[b]Discussed in text

The overall insulated length of the receiver pipe is approximately 2.7 m. This length includes a ca. 0.6 m long piece at each end which serves to minimize end effects and has 360° of insulation (i.e., no window aperture). The window aperture occupies 153 cm of length in the mid-section. Of this, only the 91 cm long portion beginning at 32 cm and extending to 123 cm (the distances refer to positions measured in the same direction as the flow, from the beginning of the aperture - refer to Figure 17) is normally studied. The mirror length is also 153 cm; hence, a shadow at either the inlet or outlet end of the aperture is present, its length a function of the solar altitude (i.e., day of the year). With the device tilted at a fixed angle of 41°, this shadow is longest at the solstices, measuring ca. 25 cm at those times. The 32 cm-123 cm central section remains fully illuminated during an experiment at any time of the year.

The pump used to circulate the fluid cannot operate at temperatures much in excess of ambient; thus the fluid, after traversing the exit flow-smoothing end piece (which is fully insulated), leaves at high temperature and is made to pass through an uninsulated copper return line, to re-enter the pump at near-ambient temperature. This restriction on receiver inlet temperature is removed by means of an electrical preheat section (770 W heating tape wrapped around the metal inlet end piece), which allows simulation of a longer receiver, under gas flow conditions.

The experimental device was located on the roof of the Mineral Industries Building at The Pennsylvania State University.

Because it was not fully weatherproofed, a shed was specifically constructed for it (part of which is visible in Figures 11 and 12), in which it was housed when not being tested. On a test day, the device was wheeled out of the shed and oriented with its longitudinal (i.e., flow) axis N-S.

In actual fabrication/construction of the device, three main constraints have been adhered to, since they are crucial to performance:

(1) The maximum tolerable concentrator array pointing error has been set at 10% of the aperture width of 2 cm, or 0.2 cm. With the array 55 cm below the aperture, the corresponding angular deviation θ is

$$\theta = \tan^{-1}(0.2 \text{ cm}/55 \text{ cm}) = 0.21°$$

(this assumes perfect mirror optics) and the permissible error in array tilt, for ca. 100 cm array width between the supporting wheels, is then

$$y/100 = \tan(0.21°) \rightarrow y = 0.36 \text{ cm} .$$

Therefore, the tracks have been constructed with a tolerance of $\pm$ 0.18 cm on the 83.8 cm track radius in order to maintain the pointing error within the specified limit.

(2) Infiltration of air into the receiver must be prevented; dilution of the heat transfer fluid would affect its heat capacity and transfer characteristics. Furthermore, the possibility of oxidation damage to receiver internals at the high temperatures encountered during experiments must be avoided. Thus, the system is hermetically sealed from atmospheric air and argon is employed as the working fluid, with the choice of fluid based on its inert nature, reasonable cost, and ease of preventing leaks.

(3) Temperature measurements of the fluid must be representative of its true energy level. For this purpose, a number of thermocouples, installed through compression fittings at both metal end pieces of the receiver, extend to five pre-selected measuring positions inside the glass receiver (see Figure 19 and Table 5).

Some difficulty has been encountered in meeting the second and third criteria. Gas leakage at the pump cannot be eliminated, so a plastic envelope with provision for feeding in a trickle of excess argon has been constructed around it. This arrangement functions well, at some additional cost in argon usage. The hard graphite vanes of the pump, in rubbing on the inside of the pump chamber, gradually grind away. The resulting very fine particulate matter is readily entrained into the flowing gas stream. Although the pump is provided with a felt filter (50 μm), this has proven ineffectual in preventing particulate carry-over into the receiver, where it coats internals. A 2 μm filter has been installed in the
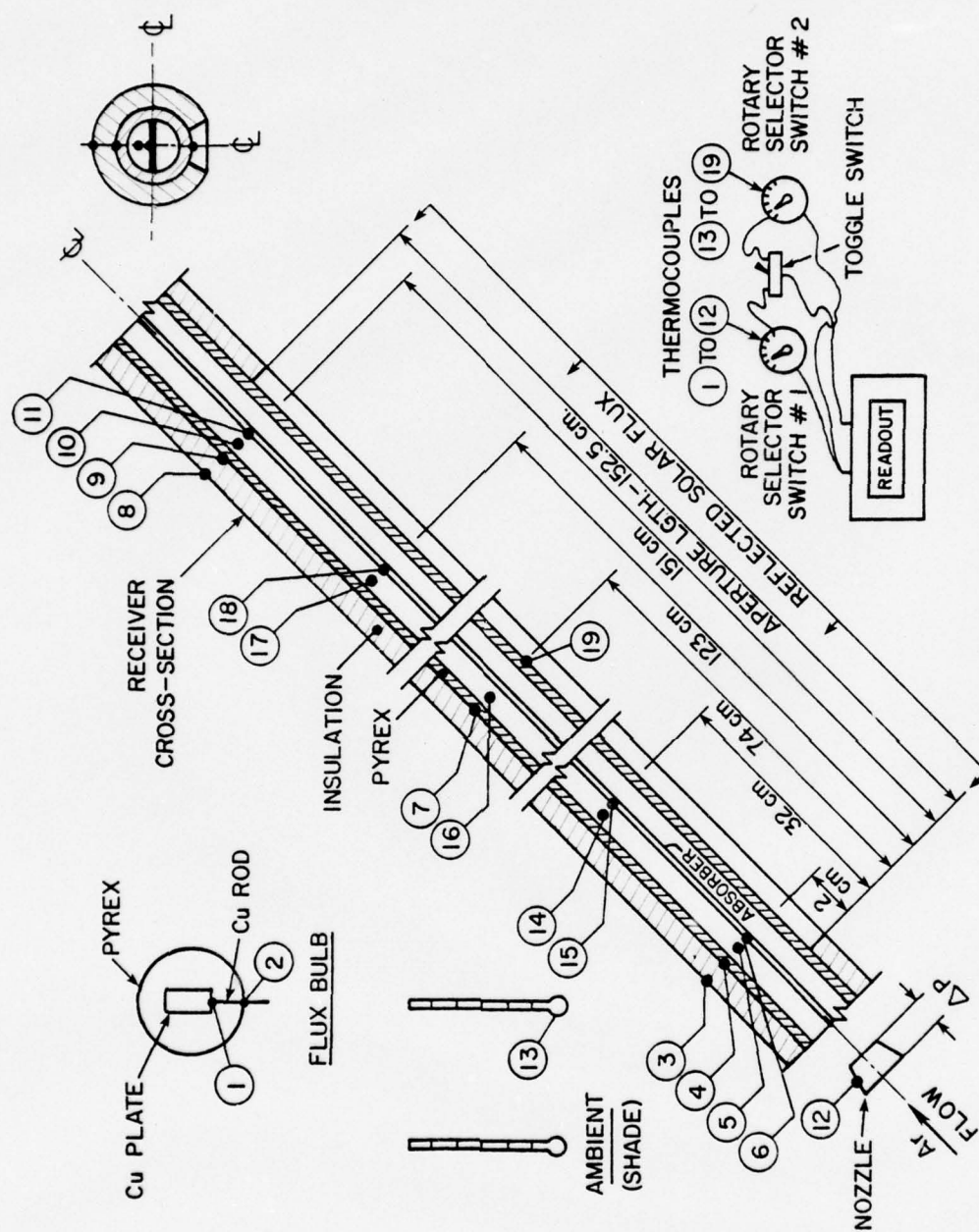
Figure 19. Thermocouple location.

Table 5. Thermocouple description.

No.	Type[a]	Position	Temperature Measured
T1	E	Inside flux bulb	Copper plate
T2	E	Outside flux bulb	Heat sink
T3	E	2[b]	Insulation exterior
T4	E	2	Pyrex exterior
T5	E	2	T_b, of gas
T6	G	2	Absorber
T7	E	74	Pyrex exterior
T8	E	151	Insulation exterior
T9	E	151	Pyrex exterior
T10	E	151	T_b, of gas
T11	G	151	Absorber
T12	E	Nozzle	T_b, of gas
T13	E	Thermometer	Ambient at collector
T14	E	32	T_b, of gas
T15	G	32	Absorber
T16	E	74	T_b, of gas
T17	E	123	T_b, of gas
T18	G	123	Absorber
T19	E	74	Pyrex at aperture

[a] E = exposed; G = grounded
[b] axial, from beginning of aperture at inlet end, cm (see Figure 19)

line (pressure drop across it is acceptable), and captures essentially 100% of the entrained particulates. Also, the binder in the asbestos gasket at the inlet metal/glass joint tends to vaporize at higher temperatures (e.g., when the heating tape is used to preheat the incoming flow) and has been replaced with silicone rubber. This can sustain the highest temperatures (probably > 400°C at the joint) without damage.

The preliminary design of the apparatus had only four thermocouples (two for the fluid, two for the graphite) placed inside the receiver. These, being located very near the receiver ends, gave temperature readings that were strongly influenced by end effects. After a few experiments, five additional internal thermocouples, extending farther into the receiver, were installed. Even with these, there is some question as to the representativeness of the measurements obtained. A full treatment of this complex topic is given in Chapter IV. All thermocouples have been fabricated and installed to comply with common practice (49,50).

To assure impingement of the concentrated solar flux on the graphite absorber, the absorber was initially constructed x-shaped in cross section. Thus, the receiver pipe was divided into quadrants. Problems were encountered with unequal heating in individual quadrants and large transverse heat conduction losses. A single flat absorber was subsequently installed, bisecting the receiver into two semicircles. It functions very satisfactorily.

A few experiments have been made with a selectively surfaced absorber replacing the graphite. The selective surface, an oxide

semiconducting layer, was formed on a brightly polished commercial Cu sheet. A number of oxidizing solutions of different concentration, plus varying exposure (immersion) times, were tried on small Cu samples in order to optimize the selective properties. Adhering to the recommendations of Christie (46) resulted in what appeared to be, visually, the best surface: a slightly glossy gray-blue surface. This surface, which had the highest α_S measured among samples, was produced by immersing a 5 cm x 120 cm copper strip (two such were used in the receiver at one time) in 2500 ml of solution containing 300 g NaOH and 150 g $NaClO_2$, maintained at 60°C and continuously stirred, for 10 minutes.

C. Material Properties

The properties of the relevant materials employed in the collector have a decided influence on its performance. Knowledge of them is a prerequisite for an understanding of the optical and thermal processes in the collector. These properties have been either measured here or taken from the literature.

1. Optical Properties

a. Solar range (ca. 300-2500nm)

On a clear day, at the bottom of the atmosphere, nearly 99% of the sun's energy spectrum lies between 300 and 2500 nm (51,52). Optical properties in this range can be readily measured with a Beckman DK-2A spectroreflectometer. This instrument does not measure

the absolute transmittance (τ) or reflectance (ρ), but compares the sample with an air/MgO or MgO reference standard. Because the MgO reflectance is very high, on the order of 0.97 (48,53,54), it is common to assume that it represents a perfect reflector, and use an MgO versus MgO calibration curve as representing total (i.e., 100%) reflectance (53). The measured sample properties are then corrected for any small departures of this curve from the 100% line on the graph. Both total and diffuse τ and ρ can be measured, but only at room temperature. The variation of these properties with temperature will be discussed in the next section.

Solar irradiance (defined as the solar flux on a unit area of surface, at the angle of incidence of the radiation, in $W\ m^{-2}$) varies with wavelength, and thus a further correction of properties is necessary to obtain a value applicable in solar experiments. Several irradiance curves have been determined; older works (55,56) have usually been based on the data of Moon (57). Thekaekara (51,52) has more recently done extensive experimental and theoretical work in this area. Solar irradiance spectra generated by a computer model of the atmosphere are available from NASA (52), and are used here.

The irradiance is a function of the air mass (AM), atmospheric ozone and precipitable water vapor content, the turbidity coefficient β, and the wavelength exponent α. A U.S. standard atmosphere with 20 mm of precipitable H_2O and 3.4 mm of O_3 is generally assumed to be present (51,52). The air mass is the ratio of the mass of air

in a column with unit cross section along the path of the solar rays, to the mass in a vertical column extending to the top of the atmosphere. For moderate z (i.e., where no account has to be taken of the curvature of the solar ray due to refraction in an increasingly denser atmosphere),

$$AM \simeq \sec z \ , \quad (51)$$

where z is the zenith angle (the angle between the vertical at a point on the earth and the line joining that point to the sun). Here, given the 41° latitude of State College, PA, and the fact that most experiments have been performed near the equinoxes, an AM = 1.5 is assumed throughout.

For atmospheric turbidity effects, Thekaekara (51) uses Ångström's equation. A. K. Ångström (58) developed an equation for the optical thickness $\tau_o(\lambda)$ due to aerosols in terms of α and β, as

$$\tau_o(\lambda) = \beta\lambda^{-\alpha} \ ,$$

where the optical thickness is defined as the number of mean free paths of a radiation photon. The exponent α is influenced by the atmospheric particle size distribution. Extensive observations indicate that a good average value is $\alpha = 1.3 \pm 0.2$ (58). The coefficient β is a measure of the turbidity, or haze content, of

the atmosphere (59). It varies widely, from several hundredths
(clear atmosphere) to several tenths (low atmospheric transparency)
(60). Values of α = 1.3 and β = 0.02, signifying a relatively clear
atmosphere (51), are selected as appropriate parameters. The inte-
grated direct perpendicular solar irradiance resulting from the
values selected is 870 W m^{-2} (52). An examination of the measured
irradiances during experiments performed here shows that this is a
reasonably good average value for a clear day in State College, PA.
Therefore, this irradiance spectrum is used in the present work
(see Table 6). It might be noted here that the solar spectral
energy partition is not very sensitive to departures in α and β
(and thus the integrated irradiance) from the chosen values (51),
and it is this spectral partition which is of interest in determining
averaged optical material properties in the solar spectral range
(see Table 6).

b. Thermal infrared (TIR)

An instrument for measuring optical properties at λ > 2.5 μm
was not available at The Pennsylvania State University. With one
exception (the graphite absorber) the values to be discussed are
taken from the literature. Quite often the published values are
not very useful because either full information on sample and source
temperatures is not presented, or the sample temperature is much
different from the anticipated application temperature.

For radiative heat exchange, two parameters are needed to
specify the desired material property. One is the temperature of

Table 6. Optical properties of materials. Measured at 25°C with a Beckman DK-2A spectroreflectometer. A MgO reference standard was used, with $\rho = 1.00$ (see text).

λ, nm	FSE, fraction solar energy in band (AM = 1.5)	1/4 mil Mylar $(\tau_{total} - \tau_{diff.})/(\tau_{air-MgO\ std.})$	FSE x τ
0 – 300	0	0	0
300 – 400	0.039	(0.8 – 0.05)/1.0 = 0.75	0.029
400 – 700	0.450	(0.81 – 0.03)/0.93 = 0.839	0.377
700 – 900	0.199	(0.81 – 0.01)/0.92 = 0.870	0.173
900 – 1600	0.223	(0.83 – 0.01)/0.93 = 0.882	0.197
1600 – 2000	0.049	(0.84 – 0.01)/0.95 = 0.874	0.043
2000 – 2500	0.028	(0.85 – 0)/0.96 = 0.885	0.025
2500 – ∞	0.012	ca. 0.8[a]	0.010
	$\Sigma = 1.000$		$\Sigma = \tau_S$ (direct) = 0.85

Table 6. Continued.

λ, nm	Mirror Strip[b]		Graphite Absorber	
	$\rho_{total}/(\rho_{MgO}$ std.)	FSE x ρ	$\rho_{total}/(\rho_{MgO}$ std.)	FSE x ρ
0 - 300	0	0	0	0
300 - 400	ca. 0.6	0.023	ca. 0.12	0.005
400 - 700	0.85/0.96 = 0.885	0.398	0.11/0.94 = 0.117	0.053
700 - 900	0.71/0.96 - 0.740	0.147	0.12/0.95 = 0.126	0.025
900 - 1600	0.68/0.97 = 0.701	0.156	0.15/1.0 = 0.15	0.033
1600 - 2000	0.76/0.98 = 0.776	0.038	0.18/0.99 = 0.182	0.009
2000 - 2500	0.80/1.01 = 0.792	0.022	0.21/0.93 = 0.226	0.006
2500 - ∞	ca. 0.85[a]	0.010	ca. 0.25[a]	0.003

$\Sigma = \rho_S$ (direct) = 0.80

$\Sigma = \rho_S = 0.13$

Table 6. Continued.

λ, nm	Lightly oxidized Cu plate (in flux bulb)		5 mm tk. Pyrex	
	$\rho_{total}/(\rho_{MgO}\ std.)$	FSE x ρ	$(\tau_{total} - \tau_{diff.})/(\tau_{air-MgO}\ std.)$	FSE x τ
0 - 300	0	0	0	0
300 - 400	0.11/0.93 = 0.118	0.005	ca. 0.7	0.027
400 - 700	0.40/0.96 = 0.417	0.188	(0.84 - 0.01)/0.93 = 0.892	0.402
700 - 900	0.77/1.0 = 0.770	0.153	(0.78 - 0.01)/0.92 = 0.837	0.167
900 - 1600	0.81/0.98 = 0.827	0.184	(0.76 - 0.01)/0.93 = 0.806	0.180
1600 - 2000	0.84/0.95 = 0.884	0.043	(0.81 - 0.01)/0.94 = 0.851	0.042
2000 - 2500	ca. 0.95	0.027	(0.73 - 0.01)/0.95 = 0.758	0.021
2500 - ∞	ca. 0.95[a]	0.011	ca. 0.65[a]	0.008
		↓		↓
		$\Sigma = \rho_S = 0.61$		$\Sigma = \tau_S = 0.85$

Table 6. Continued.

λ, nm	1 mm tk. Pyrex		Selective Cu absorber	
	τ^c	FSE × τ	$\rho_{total}/(\rho_{MgO}$ std.$)$	FSE × ρ
0 - 300	0	0	0	0
300 - 400	0.90	0.035	ca. 0.12	0.005
400 - 700	0.92	0.414	0.11/0.92 = 0.12	0.054
700 - 900	0.91	0.181	0.10/1.00 = 0.01	0.020
900 - 1600	0.90	0.201	0.09/0.99 = 0.09	0.020
1600 - 2000	0.91	0.045	0.12/0.97 = 0.12	0.006
2000 - 2500	0.90	0.025	0.13/0.93 = 0.14	0.004
2500 - ∞	ca. 0.8^a	0.010	ca. 0.15^a	0.002
		$\Sigma = \tau_S = 0.91$		$\Sigma = \rho_S = 0.11$

[a]Extrapolated

[b]Diffuse ρ is only ca. 0.01

[c]Corning data (42)

the source (or the wavelength corresponding to the maximum emissive/absorptive flux of a blackbody at that temperature, as determined by Wien's displacement law). Since radiative properties of a given material can vary appreciably with temperature of the material (not to be confused with the wavelength dependence mentioned above), the temperature of the material in question is also important.

A consistent nomenclature will be adopted here; thus

$$(\varepsilon_a)_b \text{ or } (\tau_a)_b \text{ or } (\rho_a)_b$$

will be taken to signify a source temperature or wavelength "a" (or the symbols S and IR will be used to denote a property averaged over the solar or infrared wavelengths, respectively), while "b" will correspond to the temperature of the material in question at which the property was actually measured. If b = a, only one subscript will be shown. Also, unless specified otherwise, directional dependence will be assumed negligible and the properties measured perpendicular to a surface will be used, when available.

c. <u>Data</u>

Neuroth (61) reports little change in the infrared transmittance ($\lambda > 2.5$ µm) of borosilicate glass at high temperature, while Markin and Sobolev (62) indicate that the infrared reflectances of B_2O_3 and SiO_2 (the main constituents of Pyrex glass) remain unchanged to 1000°C. Touloukian (53) shows a near-constant

transmittance of Pyrex to 800°K; thus, the value measured here at 25°C will be used as applicable to the much higher temperatures of the receiver pipe. The manufacturer measured $\varepsilon_{25°C}$ = 0.89 in one instance (34), but recommends ε = 0.94, without specifying any temperature or wavelengths, in another booklet (63). The sample thickness is not stated in either case.

Touloukian (53) reports $\varepsilon_{250°C}$ = 0.84 for a 1.3 cm-thick sample, with almost no temperature dependence of ε to 900°K. Pirani (64) measured Pyrex emittance in the 250-800°C range and gives $\varepsilon_{250°C}$ = 0.94 (no sample thickness stated, but 6.9 mm quartz standard used), again little affected by higher temperatures. Extrapolation of the manufacturer's data on transmittance yields $\varepsilon_{250°C}$ = 1.00 for a 5 mm thick sample (63). Because of the uncertainty involved, and since the aperture actually radiates from a width somewhat greater than its nominal width of 2 cm (the aperture sides do not quite touch the glass pipe, thus allowing a larger area to radiate than is available for the entering flux), a conservative $\varepsilon_{250°C}$ = 1.00 will be assumed. The 250°C temperature above has been selected as an average value, representative of the entire collector pipe length, for all experiments.

The reflectance can be calculated from the well-known modified Fresnel equation (65)

$$\rho = [(n - 1)/(n + 1)]^2 ,$$

where n is the index of refraction. Pyrex has n = 1.474 (63),

which can be considered a constant to 750°C (66), and hence

$(\rho_S)_{250°C}$ = 0.037/interface, or ca. 0.07 for both surfaces. Thus,

$(\alpha_S)_{250°C}$ = 1 - τ - ρ = 1 - 0.85 - 0.07 = 0.08. Only the reflected

flux, 0.07 of the concentrated solar flux, is taken as lost; the

absorbed component (0.08) is included in the energy balance on the

receiver (see Chapter IV).

The reflectance of the insulation material is very high, about

equal to that of the MgO reference standard, and nearly 100% diffuse.

It is assumed to be temperature-independent over the range of interest,

i.e., $(\rho_S)_{250°C}$ = ca. 1.00. The characteristic temperature is again

taken as 250°C. Singham (44) lists the integrated hemispherical

emittance of asbestos paper (the ε of asbestos board being nearly

identical at other temperatures, but not shown for temperatures of

interest here) as $\varepsilon_{200°C}$ = 0.94, and $\varepsilon_{100°C}$ = 0.93.

The graphite absorber material presents more difficulties.

The measured $(\alpha_S)_{25°C}$ of 0.87 is in good agreement with the value

$(\alpha_{6000°K})_{25°C}$ = 0.85 measured by Sieber (67) for a graphite material,

but is lower than the $(\alpha_S)_{25°C}$ = 0.91-0.92 of "7087" graphite in

Touloukian (53). With a few exceptions, most graphites exhibit

optical properties that are nearly independent of wavelength and of

sample temperature to at least 1000°C (53,68,69). Data on the tempera-

ture dependence of α_S for the 787G graphite used here are apparently

not available. It will therefore be assumed that $(\alpha_S)_{25°C}$ = 0.87

is valid at 250°C, the assumed typical operating temperature. Because

the view factor from the graphite to the aperture (i.e., the out-side) is so small, any inaccuracy in the absorptance, and hence the reflectance, will have little bearing on calculated results.

The infrared emittance of Speer "7087" graphite has been measured (53,68) (Speer does not manufacture a 7087 graphite; 787G was probably intended (70)). The reported value, $\varepsilon_{250°C}$ = 0.85-0.9 (53,68) is also valid for some other graphite types (68,69). A sample of the absorber was sent to the W. B. Meinel Laboratory (71), which tested emittance to sample temperatures of 200°C, and over $2 < \lambda < 15$ μm. The results, which indicate strongly selective properties (i.e., high α_S and low ε_{IR}), conflict both with extrapo-lated trends of the measurements made here and also with the literature cited (except Sieber (67), and even there the selectivity is much less).

The measured $(\alpha_S)_{25°C}$ = 0.89 of the selective Cu absorber is in good agreement with the measurements of Christie (46) and with Hottel and Unger (72). The one available measurement of emittance, $\varepsilon_{65°C}$ = 0.20, is by Christie. Temperature effects are not known, although some of Singham's (44) data suggest that they may be negli-gibly small.

Tien et al. (73) have measured the τ_{IR} of 1/4-mil Mylar; it remains quite high except for some strong resonances in the 8-10 μm region. Therefore, the Mylar absorbs little energy and probably operates here at temperatures only slightly above ambient; hence, its measured $(\tau_S)_{25°C}$ = 0.85 should apply. For the reflector and flux bulb, ambient operation is assumed.

2. Thermal Properties (Conductivity)

The required thermal properties of the materials used either
are taken from the literature or are available from the manufacturers.
Although the conductivity is a function of temperature, it is so con-
sidered only for the insulation and for the argon gas (the viscosity
and density of the gas are also taken as variable); the density of
n-butyl phthalate in the flow measuring manometer is also considered
a temperature-dependent property. The conductivities of graphite, Cu,
and Pyrex (and the Hg density in the pressure manometer) are taken as
constants here because resulting errors in the mathematical analysis
will be slight, and the analysis (see Chapter IV) will become more
tractable thereby.

As in the case of optical properties, difficulties were
encountered in characterizing the graphite. The manufacturer (45)
was unable to provide date on the thermal conductivity, but did
supply information on the resistivity (which is known to vary
inversely with the thermal conductivity), and the coefficient of
thermal expansion (CTE). 787G graphite is anisotropic; its proper-
ties vary because of the extrusion process used in its manufacture.
The electrical resistivity is 7.1×10^{-4} ohm-cm measured parallel to
the grain (i.e., extrusion), and the CTE is $2.4 \times 10^{-6} \, °C^{-1}$ (parallel)
and $4.3 \times 10^{-6} \, °C^{-1}$ (perpendicular to the extrusion axis), yielding a
CTE anisotropy ratio of $2.4/4.3 = 0.56$. The Kirk-Othmer Encyclopedia
(74) gives data on many graphite types: an AGOT graphite has a resis-
tivity (parallel to the extrusion axis) of 7.35×10^{-4} ohm-cm and a

CTE ratio of 0.57, closely matching similar properties of the 787G graphite. Its thermal conductivity is 173 W m^{-1} °C^{-1}. Touloukian (53) gives data on the conductivity of grade "7087" (i.e., assumed to be 787G, as discussed earlier) Speer graphite, but only over the temperature range 800-1900°K. Extrapolating this to 300°K gives k ≈ 210 W m^{-1} °C^{-1}, decreasing rapidly to 136 W m^{-1} °C^{-1} by the first data point at 800°K. Because of the uncertainty in the conductivity, and graphite temperatures above 300°K in the present work, a value of k = 173 W m^{-1} °C^{-1} is selected as typical.

D. Operation

1. Preliminary Alignment and Calibration

Before experiments could be performed with the device, the following tasks had to be performed:

(1) Calibration of the flow-rate-determining nozzle. This had been constructed with a diameter ratio (constriction diameter/ upstream diameter) well under the maximum of 0.5 recommended (76) for accurate metering at low Re. The nozzle was also made suffi- ciently long for flow perturbations to be minimal (76,77). It was calibrated against a wet test meter (Precision Scientific) using the actual pump of the experimental device. Various flow rates, to a maximum deliverable 108.5 liters/minute of air at ambient con- ditions, were used. The flow was then corrected to provide a

calibration for argon flow at standard temperature and pressure (STP, 25°C and 760 torr here) (see Table 7 and Figure 20).

(2) For accurate E-W tracking at a constant 15°/h, the receiver axis has to be parallel to the earth's axis of rotation (i.e., N-S). The required alignment was accomplished as follows: the time of solar noon was determined from a solar ephemeris tabulation (these are available from several sources, e.g., K and E Company). The shadow cast by a vertical structure is at that instant in the true N-S plane. The shadow position was marked (for minimum error, this procedure was repeated a number of times, on widely spaced days) and the receiver axis was aligned along the markings.

(3) Each mirror strip of the Archimedes concentrator was focused onto the receiver aperture. The method was straightforward: all the strips except one were first covered with opaque material. The device was oriented N-S, and the mirror array positioned (motor-driven) perpendicular to the plane defined by the receiver axis and the sun. The single uncovered strip was quickly rotated until its reflected beam fell onto the aperture, meanwhile tracking the sun with the step motor. An accurate tracking speed (i.e., pulse/ time by the timing circuit to the stepping motor, ca. 2.5 pulse/s at a motor step increment of 0.9°/pulse) was then determined by trial-and-error over long time periods. No provision was made for feedback of tracking error to the timing circuit, so this had to be

Table 7. Nozzle calibration.

ΔP, cm H_2O[a]	Flow rate[b], air, liter min^{-1}	Equivalent ΔP of $C_{16}H_{22}O_4$[c]	Flow rate[d], Ar liter min^{-1}
14.5	108.45	13.9	97.31
11.6	96.56	11.1	86.64
9.0	86.65	8.6	77.73
6.8	76.17	6.5	68.32
5.0	67.11	4.8	60.20
4.7	65.70	4.5	58.93
3.8	60.31	3.7	54.10
3.3	56.35	3.2	50.55
2.5	49.84	2.4	44.71
1.6	41.34	1.5	37.08
0.6	32.56	0.6	29.21
0.4	20.10	0.4	18.03

[a] Measured, see Figure 20

[b] Measured average over 5 min., at ambient conditions (T = 24.5 °C, P = 729 torr, P water vapor in wet test meter = 23.2 torr, rel. humidity = 87%)

[c] n-butyl phthalate, cm, at 25°C

[d] i.e., at 760 torr, 25°C, determined by: (flow rate, air) [(729 + 23.2)/760](0.905)(298/297.5), where Reuther (75) recommends a factor of 0.905 to correct for air/argon differences. Ideal gas behavior is assumed.
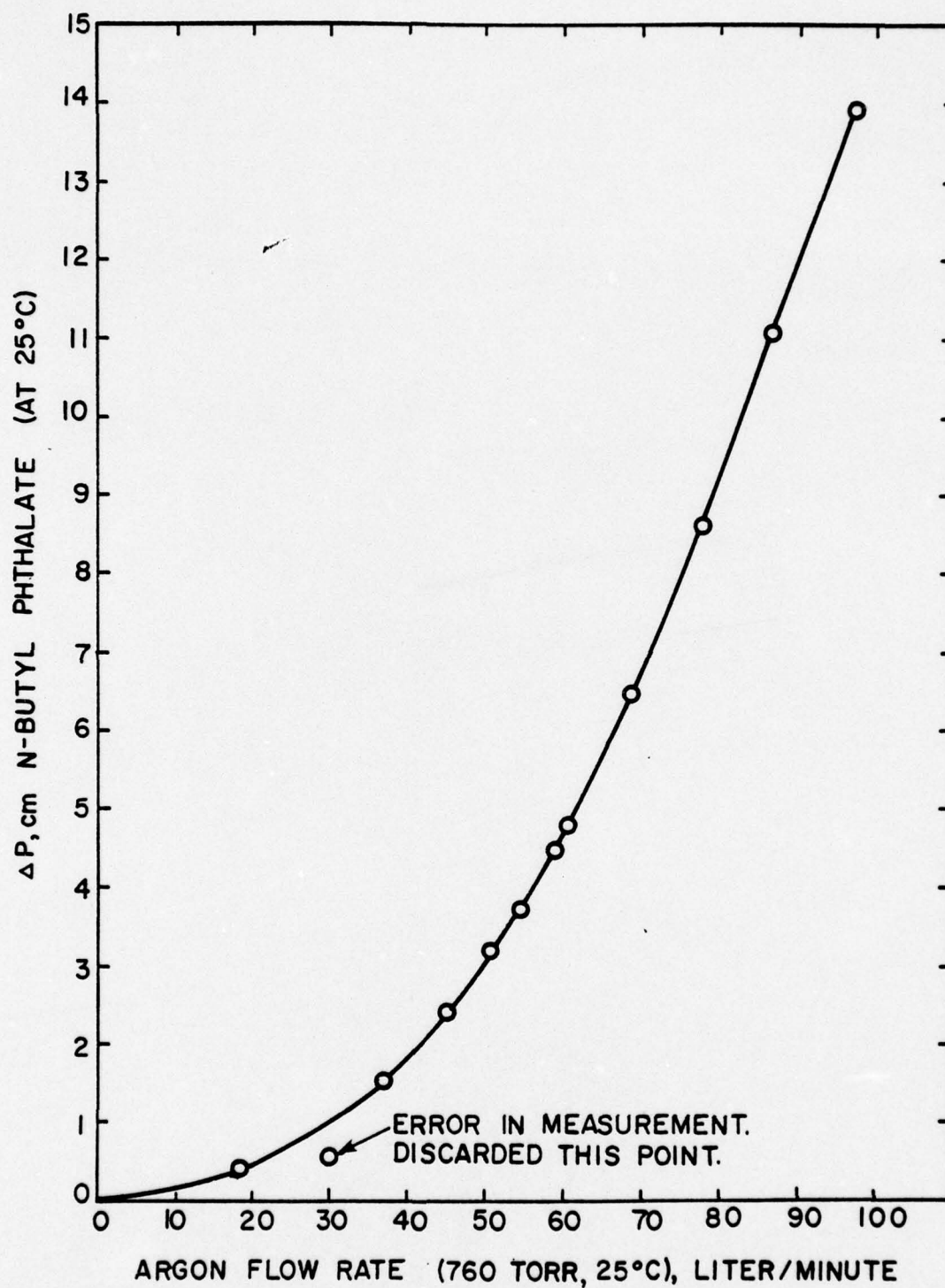
Figure 20. Nozzle calibration.

done quite carefully. After what was considered acceptable tracking accuracy had been achieved (i.e., no manual corrections were necessary for a period of 2-3 h), the remaining mirror strips were aligned singly by uncovering each separately, focusing its beam, tightening the locknuts fixing it to the array frame, and then covering it again while continuously tracking the sun. As an additional precaution, the mirror strip which had been aligned first was kept uncovered throughout, and its focus monitored. The focusing was performed several times, at different array positions on the track, as the optimum alignment for a particular position was not the best for all positions; a compromise focus was the result, with an estimated 5% (i.e., 2 mirror strips/40) loss of the flux from misalignment (see Figure 13). It is assumed that all of the flux missing the window is lost, even though it impinges on the aperture sides. Once the mirrors were properly aligned, no further corrections were required thereafter as long as the receiver position did not alter, as after changing absorbers - which minutely displaced the receiver axis.

(4) Taking advantage of the selective radiative properties of copper, a thin 10 cm^2 plate was mounted within an evacuated Pyrex glass bulb. When this device is exposed to sunlight, the plate warms. The only important thermal loss occurs by conduction along a copper support rod, hence the incident direct solar flux can be calculated from the difference between the measured plate and ambient temperatures. The device was mounted on the tracking mirror array, and was masked so the plate only "saw" a small angle of the sky (see Figure 15).

2. Experimental Procedure

The concentrator, which focuses only the direct component of
the solar flux onto the receiver aperture, limits operation to cloud-
less days. Tracking was initiated ca. 3 hours prior to solar noon.
The receiver required approximately 90 minutes to attain its asymp-
totic temperature. The first set of readings was taken at the end
of this time period. Flow was started thereafter with attainment
of steady-state conditions within 30-60 minutes (depending on the flow
rate selected). Appropriate temperature, pressure, and solar flux
measurements were then made every 30 minutes until the end of the
experiment. In greater detail:

(1) The collector was wheeled out of its shed and its axis
aligned N-S. The entire device was light enough so that this was
easily performed by one person.

(2) The receiver was filled with argon (or still contained
argon from a recent past experiment).

(3) The reflector was cleaned with a commercial cleaner
(Windex) and acetone, in that order.

(4) The mirror array was positioned on the tracks such that
the reflected and concentrated solar beam was focused onto the
aperture. A fast-forward provision in the timing circuit allowed
this to be done quite rapidly; the stepping motor, although small,
had sufficient torque (ca. 29 kp cm max. in its 0.9°/step mode)

for this maneuver. The track diameter and array width combine to
restrict permissible array travel to ca. 45° off-horizontal, or
to ca. 6 hours total operation when centered about solar noon.
The normal tracking speed (pulse rate) was set, and tracking began.

(5) After attainment of steady-state stagnation conditions
(Figure 21), temperature readings were taken and recorded. This
was done to check thermocouple response (the switches could affect
this, if not cleaned frequently). Also, the asymptotic temperatures
gave some indication of the solar flux level; if a wide discrepancy
between the two solar flux measurements was observed, one could
have an indication as to which was the more accurate measurement
by comparing these measurements with previous experimental flux
and asymptotic temperature measurements.

(6) The system was re-charged with Ar for ca. 2 minutes at
a gauge pressure of ca. 100 torr. The pump was run at a low flow
rate (ΔP = 2 cm phthalate) for ca. 15 s during this interval.

(7) The pump was started and the flow rate set. A trickle
of Ar was fed into the envelope around it, keeping that gently
inflated.

(8) If used, pre-heat was set and maintained at some chosen
level on the Variac. T5 and T6 monitor the preheat and attainment
of steady-state conditions with it operational.
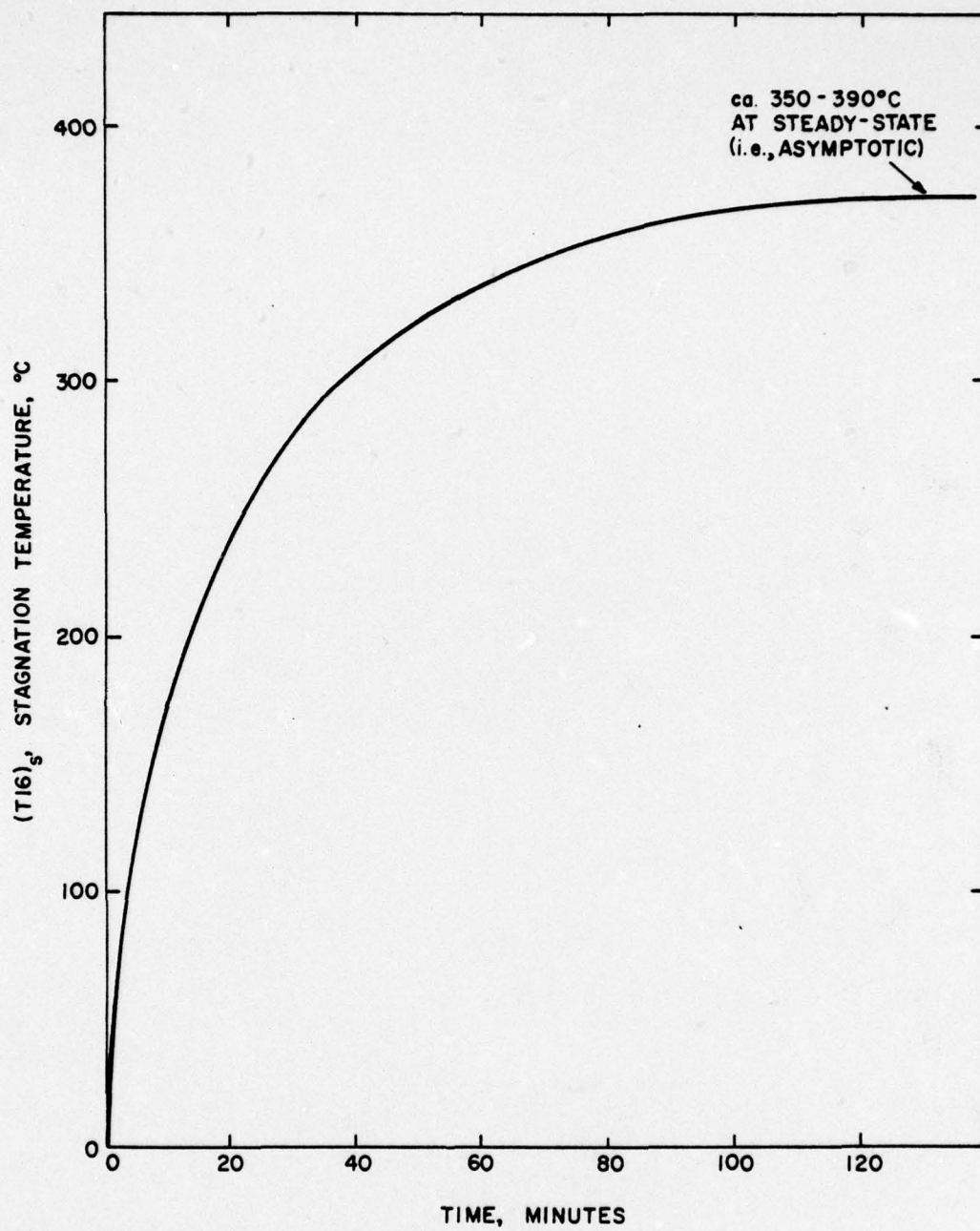
Figure 21. Time-dependent temperature response (measured).

(9) Readings of temperatures, pressures, and other parameters were taken every 30 minutes thereafter (Table 8). Although steady-state conditions were achieved within, at most, an hour after initiating flow, the flow rate was generally maintained the same throughout the day as a check on reading accuracy, etc. Occasionally, two or even three different flow rates have been employed on the same day to take advantage of the infrequent occurrences at State College, PA, of bright, clear skies.

E. Experimental Results

1. Flow Range Restrictions

One complication in studying a small thermodynamic model is that various effects, such as end losses, transverse temperature gradients, etc., which may play a negligible role in a full-scale device, often exert a strong influence on the experimental results. In the present study, it is found that at flows much greater than 40 liters min^{-1} (ca. Re = 800, or ca. 40 cm s^{-1} mean velocity in the receiver, STP) flow disturbances near the receiver outlet cause anomalous temperature profiles in the downstream half of the receiver. The effect worsens with increasing flow rate, although examination of the data (see Table 8) reveals that the heat transfer rate is not affected. The disturbances are most likely caused by the too-short exit end piece, and the abrupt constriction at the small-diameter copper return line. This causal hypothesis can be readily tested

Table 8. Experimental results (flowing gas).

Date*	19.IX.76		23.IX.76		24.IX.76		29.IX.76[a]
Time	1:45	2:30	2:00	3:00	1:45	2:45	3:30
Angle, cm	78.5	91.5	89	114.5	84	102	131
$\Delta P_{phth.}$, cm	2.8	11.7	1.9	10.9	0.8	5.4	3.1
ΔP_{Hg}, cm	-1.6	5.1	-2.9	5.1	-1.6	1.2	-0.7
P_∞, cm	72.3	72.3	72.5	72.5	72.8	72.7	72.3
T_∞, °C	28	27	22.5	23	21	20	20
Flux, ly min^{-1}	1.16	1.06	1.06	0.96	1.12	1.02	0.81
Shadow, cm	0	0	1.5	1.5	1.5	1.5	4
Wind, m s^{-1}	0	0	4	4	1	1	2
T1, °C	--	--	44.5	45.5	49	47	40.5
T3	47	42	36	37	50	43	37
T4	93	68	70	60	96	77	153
T5	55	43	45	37	68	43	229
T6	102	74	92	66	127	84	226
T14	163	83	170	87	235	127	257
T15	233	172	231	173	296	232	300
T7	220	168	210	175	283	231	245
T19	128	113	122	118	208	147	135
T16	238	130	233	138	319	215	278
T17	270	150	271	158	340	246	290
T18	298	228	300	228	350	295	316
T8	60	55	46	46	63	66	48
T9	216	172	211	177	264	237	224
T10	270	180	267	189	315	272	286
T11	272	228	273	238	309	292	286
T12	45	53	35	46	31	46	31
$(T16)_s^g$, °C	331		342		372		352

Table 8. Continued.

Date*	3.X.76[a]		4.X.76[a]		11.X.76		12.X.76	
Time	1:15	2:45	1:50	3:00	2:15	3:15	1:15	2:30
Angle, cm	91.5	114.5	99	119.5	114.5	140	101.5	120.5
$\Delta P_{phth.}$, cm	11.4	8.5	1.2	6.1	1.5	3.1	12.3	5.9
ΔP_{Hg}, cm	5.6	3.8	-3.1	2.2	3.3	4.9	15.0	8.5
P_∞, cm	72.4	72.4	72.8	72.8	73.4	73.4	73.2	73.1
T_∞, °C	23	24	23	22	14	15	16	16.5
Flux, ly min^{-1}	1.02	0.92	0.97	0.85	0.95	0.79	1.00	0.90
Shadow, cm	5	5	5	5	8.5	8.5	9	9
Wind, m s^{-1}	2.5	3	2	2.5	1.5	1.5	3	3
T1, °C	47	45	47	45	42	40	42.5	42
T3	43	49	57	43	29	29	26	28
T4	131	136	162	152	35	40	36	40
T5	166	182	259	197	28	27	35	31
T6	176	187	240	206	65	55	45	51
T14	196	208	270	224	95	71	60	64
T15	257	260	296	276	206	145	145	158
T7	224	210	259	239	216	184	160	170
T19	145	135	172	123	115	115	106	85
T16	224	235	299	251	219	168	111	138
T17	228	240	313	260	271	208	125	164
T18	283	282	326	294	300	250	169	206
T8	58	62	74	56	59	56	48	45
T9	226	207	250	223	251	227	193	201
T10	246	245	302	271	285	237	141	192
T11	278	265	292	282	298	289	226	248
T12	48	51	36	45	32	37	54	39
$(T16)_s^g$, °C	-		331		361		370	

Table 8. Continued.

Date*	15.X.76[b]		23.X.76		14.XI.76	19.XI.76[c]	
Time	1:30	2:45	1:30	2:30	1:00	12:30	1:50
Angle, cm	105	131	118	140	164	161	203
$\Delta P_{phth.}$, cm	3.0	12.1	1.4	6.0	12.7	0.25	0.9
ΔP_{Hg}, cm	5.3	14.8	3.2	8.6	15.4	0.9	2.2
P_∞, cm	72.1	71.9	73.1	73.1	72.5	71.9	71.9
T_∞, °C	24	25	12	13	6	14	14
Flux, ly min^{-1}	0.91	0.79	0.90	0.80	0.74	0.67	0.53
Shadow, cm	10	10	12.5	12.5	20.5	21.5	21.5
Wind, m s^{-1}	8	8	3	3.5	5.5	8.5	8.5
T1, °C	46	45.5	34	33.5	28	32	30
T3	31	30	19	22	9	17	16
T4	39	34	27	25	14	25	19
T5	31	34	19	23	17	22	17
T6	47	43	36	32	19	33	26
T14	67	52	56	42	26	71	35
T15	157	119	139	115	77	128	90
T7	180	126	182	125	102	205	127
T19	173	145	170	140	123	174	130
T16	157	102	172	103	66	212	133
T17	202	107	228	126	82	272	193
T18	240	147	263	166	122	292	223
T8	49	38	43	40	22	32	30
T9	223	154	226	170	143	206	164
T10	227	126	251	149	98	267	219
T11	265	200	275	222	193	259	231
T12	36	45	23	37	28	15	18
$(T16)_s$[g], °C	353		333		348	ca. 300	

Table 8. Continued.

Date[*]	14.XII.76	11.II.77	2.III.77	9.III.77	11.III.77
Time	12.:45	1:15	1:30	1:15	1:00
Angle, cm	193	135	109	96.5	91.5
$\Delta P_{phth.}$, cm	2.0	12.6	5.9	6.0	4.4
ΔP_{Hg}, cm	3.9	15.9	9.0	9.0	7.4
P_∞, cm	73.1	72.9	73.4	73.2	73.3
T_∞, cm	1	14	5	20	23
Flux, ly min^{-1}	0.66	0.84	1.03	1.04	1.01
Shadow, cm	25.5	15	9	5	4.5
Wind, m s^{-1}	2.5	6	6.5	5	2.5
T1, °C '	22	35	29	45	45
T3	7	19	15	28	36
T4	9	21	18	40	47
T5	5	24	13	29	33
T6	10	28	28	52	61
T14	17	35	42	63	76
T15	72	101	102	155	174
T7	136	111	141	160	173
T19	138	133	156	150	184
T16	109	73	116	134	158
T17	175	98	152	161	187
T18	207	135	133	214	231
T8	25	30	34	41	57
T9	200	146	185	195	215
T10	210	111	176	186	214
T11	249	189	239	242	261
T12	10	37	23	36	46
$(T16)_s^g$, °C	--	340	379	367	366

Table 8. Continued.

Date[*]	17.III.77	19.III.77	23.III.77	29.III.77	30.III.77
Time	1:00	1:30	1:45	1:15	12:25
Angle, cm	85	89	87.5	75	68.5
$\Delta P_{phth.}$, cm	2.0	1.35	1.1	0.65	2.5
ΔP_{Hg}, cm	4.1	3.2	2.7	2.4	5.2
P_∞, cm	72.4	72.6	72.4	72.5	72.5
T_∞, cm	11	7.5	8.5	27	29
Flux, ly min^{-1}	1.19	1.16	1.17	1.12	1.15
Shadow, cm	2	1	0	0(2)[e]	0(3)
Wind, m s^{-1}	6	3	8	5.5	5
T1, °C	33.5	31	32	53	54
T3	24	25	21	44	42
T4	45	48	54	75	73
T5	23	26	29	49	44
T6	71	83	99	115	100
T14	94	120	143	177	111
T15	194	216	231	253	205
T7	203	221	232	249	208
T19	195	216	215	230	195
T16	196	226	245	273	201
T17	245	281	298	316	239
T18	282	318	336	346	281
T8	46	51	44	57	55
T9	238	249	253	244	222
T10	271	302	315	313	260
T11	292	310	316	296	269
T12	24	23	21	37	41
$(T16)_s$[g], °C	372	358	388	367	365

Table 8. Continued

Date[*]	1.IV.77	12.IV.77[a]	15.IV.77	17.IV.77[a]	8.V.77[a]
Time	12:45	1:45	2:15	1:45	1:35
Angle, cm	67.5	71	81	68	42
$\Delta P_{phth.}$, cm	3.0	1.55	2.5	1.45	1.5
ΔP_{Hg}, cm	5.8	3.8	4.4	3.0	3.3
P_∞, cm	73.3	73.5	73.0	73.1	72.3
T_∞, cm	14	30.5	25	26	22
Flux, ly min^{-1}	1.22	1.09	1.15	1.16	1.38
Shadow, cm	0(4)	0(7.5)	0(9)	0(10)	0(16)
Wind, m s^{-1}	1.5	7.5	4	2	7.5
T1, °C	39	50.5	50	49	43
T3	30	54	45	64	28
T4	61	152	75	226	95
T5	30	206	42	333	99
T6	82	219	99	321	149
T14	94	240	114	343	169
T15	196	287	213	364	250
T7	191	222	190	256	167
T19	200	213	189	248	195
T16	187	272	206	356	238
T17	228	288	241	355	265
T18	271	315	283	372	287
T8	48	59	59	65	34
T9	226	210	196	228	177
T10	253	281	250	321	248
T11	268	256	242	278	215
T12	36	46	39	43	30
$(T16)_s^g$, °C	388	364	390	378	358

Table 8. Continued.

Date[*]	14.V.77[a]		26.V.77[d]		
Time	1:45	2:45	1:30	2:30	3:30
Angle, cm	39.5	53.5	33	43	66
$\Delta P_{phth.}$, cm	2.9	2.85	0.65	1.0	1.5
ΔP_{Hg}, cm	5.3	5.2	2.0	2.8	3.3
P_∞, cm	72.6	72.6	72.9	72.9	72.9
T_∞, cm	30	33	33	34	32
Flux, ly min^{-1}	1.36	1.27	1.34	1.28	1.19
Shadow, cm	0(18)	0(18)	0(20)	0(20)	0(20)
Wind, m s^{-1}	4	4.5	4	4	4
T1, °C	53	55	53	56	53
T3	49	58	49	51	49
T4	105	149	80	77	74
T5	95	182	58	51	47
T6	150	209	141	133	122
T14	152	221	173	164	151
T15	250	287	264	248	230
T7	216	238	242	232	216
T19	214	225	218	210	188
T16	235	263	278	256	220
T17	245	272	305	288	262
T18	276	297	326	315	289
T8	51	56	56	59	56
T9	183	189	189	182	174
T10	241	262	246	253	244
T11	218	231	218	226	221
T12	46	46	38	43	42
(T16)$_s$[g], °C	375		384		

Table 8. Continued.

Date[*]	3.VI.77[d]			4.VI.77[d]		
Time	1:30	2:30	3:30	1:30	2:30	3:30
Angle, cm	30.5	42	63.5	30.5	42	63.5
$\Delta P_{phth.}$, cm	2.0	2.5	3.0	1.0	1.5	2.0
ΔP_{Hg}, cm	4.1	4.7	5.4	2.6	3.3	4.0
P_∞, cm	73.2	73.2	73.2	73.2	73.2	73.2
T_∞, cm	25	26	27	33	34	36
Flux, ly min^{-1}	1.41	1.36	1.22	1.36	1.31	1.19
Shadow, cm	0(23)	0(23)	0(23)	0(23)	0(23)	0(23)
Wind, m s^{-1}	4	4	4	3.5	3.5	3.5
T1, °C	48	49	50	55	56	57
T3	39	40	42	47	44	44
T4	66	61	64	74	72	70
T5	38	36	39	52	46	45
T6	107	103	98	129	117	109
T14	127	113	100	165	144	126
T15	219	206	193	234	217	200
T7	227	203	193	247	224	212
T19	198	187	173	222	207	193
T16	210	194	181	256	228	205
T17	247	230	212	284	260	237
T18	274	258	244	306	289	261
T8	45	46	48	55	54	54
T9	172	160	153	181	170	162
T10	233	221	209	242	237	224
T11	213	207	198	216	215	207
T12	38	40	41	40	43	44
$(T16)_s$[g], °C		359[f]			333[f]	

*The terms and symbols in this column of Table 8 have the following significance:

date   The date of the experiment.

time   The time the data was recorded.

angle   Horizontal length of shadow cast by a vertical 91.5 cm high rod.

$\Delta P_{phth.}$ Pressure drop across the flow measuring constriction. The manometer fluid was n-butyl phthalate.

ΔP_{Hg} Fluid static pressure at the flow measuring constriction. The manometer fluid was mercury; one side of the manometer was open to the atmosphere.

P_∞ The ambient atmospheric pressure, in centimeters of mercury.

T_∞ The ambient temperature.

flux   The total solar flux on a horizontal surface in langley min^{-1} (langley = gram calorie cm^{-2}). Measured by The Pennsylvania State University Meteorological Station.

shadow   Length of aperture shadow, at the receiver inlet end.

wind   Wind velocity. Measured by The Pennsylvania State University Meteorological Station.

T1 – T18   Temperatures measured by various thermocouples (see Figure 19 and Table 5).

[a] Preheat used

[b] Mylar cover installed over aperture; all subsequent experiments had this feature

[c] New digital pyrometer used here and thereafter

[d] Selective absorber used here instead of the graphite

[e] No shadow at inlet hereafter; in parentheses is the length of aperture shadow, now at the outlet end

[f] Low reading; probable cause is absorber buckling in the vicinity of the thermocouple, bringing it close to the relatively colder glass tube

[g] Steady-state stagnation temperature, T16, measured just prior to the start of flow

by installation of a longer exit end piece, and/or a larger-diameter return line. However, the size of the storage shed, which was barely large enough for the collector as is, prevented such a test.

This perturbed condition limits the upper flow range available for experiment and analysis. No attempt has been made to formulate the perturbed behavior in mathematical terms, because it appears to be too complex to treat. Very low flow rates are also ruled out, since below Re · Pr = 300 axial conduction in the gas may no longer be negligible (78); it is certainly a factor at Re · Pr ≤ 100 (79).

2. Temperature Reading Accuracy

Temperatures were at first measured with an old instrument, a Hoskins pyrometer. These readings were found to be inaccurate because the instrument:

(1) Was not temperature-compensated. A correction was made by attaching a thermocouple to a calibrated thermometer in the ambient environment. This became, in effect, the reference temperature.

(2) Above 100°C readings were higher than actual, the difference (even as a percentage) increasing with higher temperatures. The error was considerable: for example, at 511°C the instrument read 558°C.

(3) The instrument had a low internal resistivity. The electrical resistivity of 28 ga. Chromel-Alumel wires (the thickness used here) is about 12.5 ohm/double m (i.e., for both wires; the value is a sum of individual resistivities). Wire lengths of up to 5 m were used and the readings from the longer wires were thus significantly lowered.

A digital readout instrument has therefore been used for most measurements. It was calibrated at 0°C, 100°C, and 511°C; its internal cold junction reference was also calibrated, as prescribed. The high internal impedance of this instrument permits accurate measurement even with the longest wires used here. As a check on accuracy, a voltage corresponding to 689°C was fed into the longest lead (which went through two switches). The instrument error then was on the order of 1°C. When all the experiments had been completed, this check was repeated, with similar results. Also, an ice bath was employed on several occasions (as well as the previously-mentioned thermocouple/thermometer combination for ambient temperature comparison, which was used throughout) to check zero drift and internal compensation accuracy. The readings were generally within 1°C of actual, with an occasional maximum error of 3°C. Considering the prevailing operating conditions - outside environment, with varying sun, wind, and temperature - this was very good performance. Repeatability was excellent, always within 1°C.

The old instrument was calibrated against the new one, thermocouple-by-thermocouple, and at various temperatures. The data acquired by means of the old instrument were then corrected, and are so shown here (Table 8).

3. Material Degradation

At the end of the experiments, all materials whose optical properties had been previously measured (Table 6) were measured again to determine the effect of operation at high fluxes and/or high temperatures. After ca. 200 hours of operation, the graphite absorber exhibited no measurable change in its properties. The total reflectance of the mirrors, as well as the total transmittance of the Mylar cover also remained unchanged. The diffuse properties of the mirror and the Mylar did show some slight degradation: the diffuse reflectance of the mirror increased by ca. 3 percentage points, and the diffuse component of transmittance in the Mylar increased by about 4 percentage points. These values are over the wavelength range $400 < \lambda < 1600$ nm, which contains ca. 90% of the solar energy. The Mylar cover was replaced several times (e.g., to clean the Pyrex window), and this particular sample had been subjected to a concentrated flux for ca. 72 hours.

Because degradation was so minuscule, and its effect on performance difficult to quantify (also, the degradation rate may not have been constant), it was not incorporated into the calculations of Chapter IV. The Pyrex was not remeasured since no acceptable method had been found to expose a small sample to the environment

"seen" by the glass receiver pipe, while the copper absorber surface
was so badly degraded (after only ca. 20 h of operation) that measure-
ments would have been pointless.

F. Conclusions

The experimental device achieves high temperatures and performs
essentially as expected. Stagnation temperatures show that the
32-to-123 cm axial section of the aperture exhibits a quite flat
temperature profile near the equinox (Figure 22). Off-equinox
operation, when significant shadowing occurs over one aperture end
section, indicates some end-effect penetration into the 32-123 cm
section (Figure 23). The influence is not great, and would probably
be even smaller under gas flow conditions. Its effect on the axial
gas bulk temperature profile is considered negligible; i.e., the
32-cm gas bulk temperature (the starting temperature for calcula-
tions) already incorporates any such effect, if present, while the
123-cm thermocouple position, being upstream of any shadow at the
outlet, would be negligibly affected thereby. Examination of the
experimental results (Table 8) reveals large variations in tempera-
tures with flow rate; ambient temperature, aperture shadowing (at
the inlet), and the solar flux also exert an influence. A full
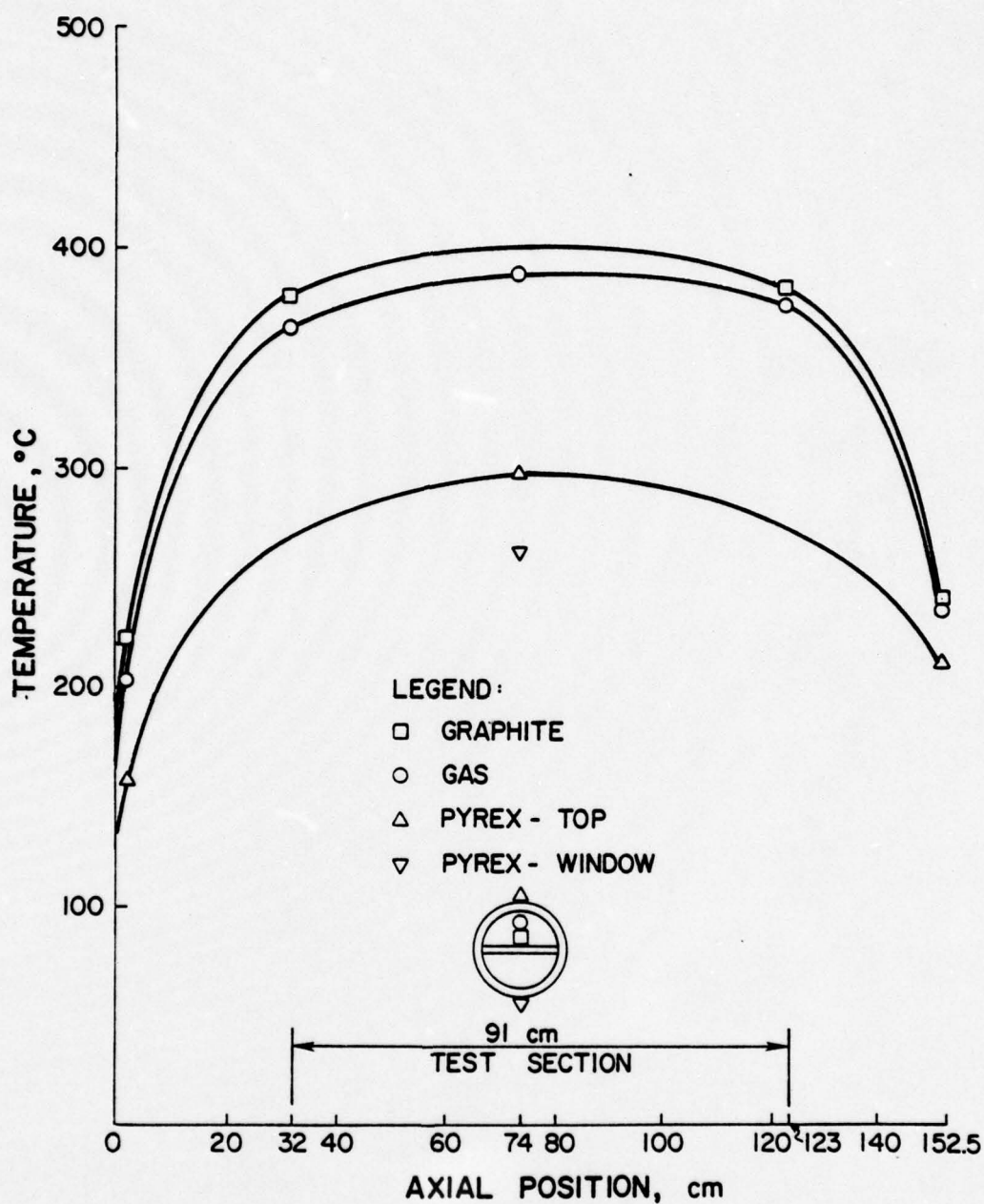discussion of these is reserved for Chapter IV.

Figure 22. Steady-state stagnation temperatures of receiver
measured on 23.III.77, 12:00 p.m. The direct
solar flux was ca. 870 W m^{-2}, and the ambient
temperature was 7°C.
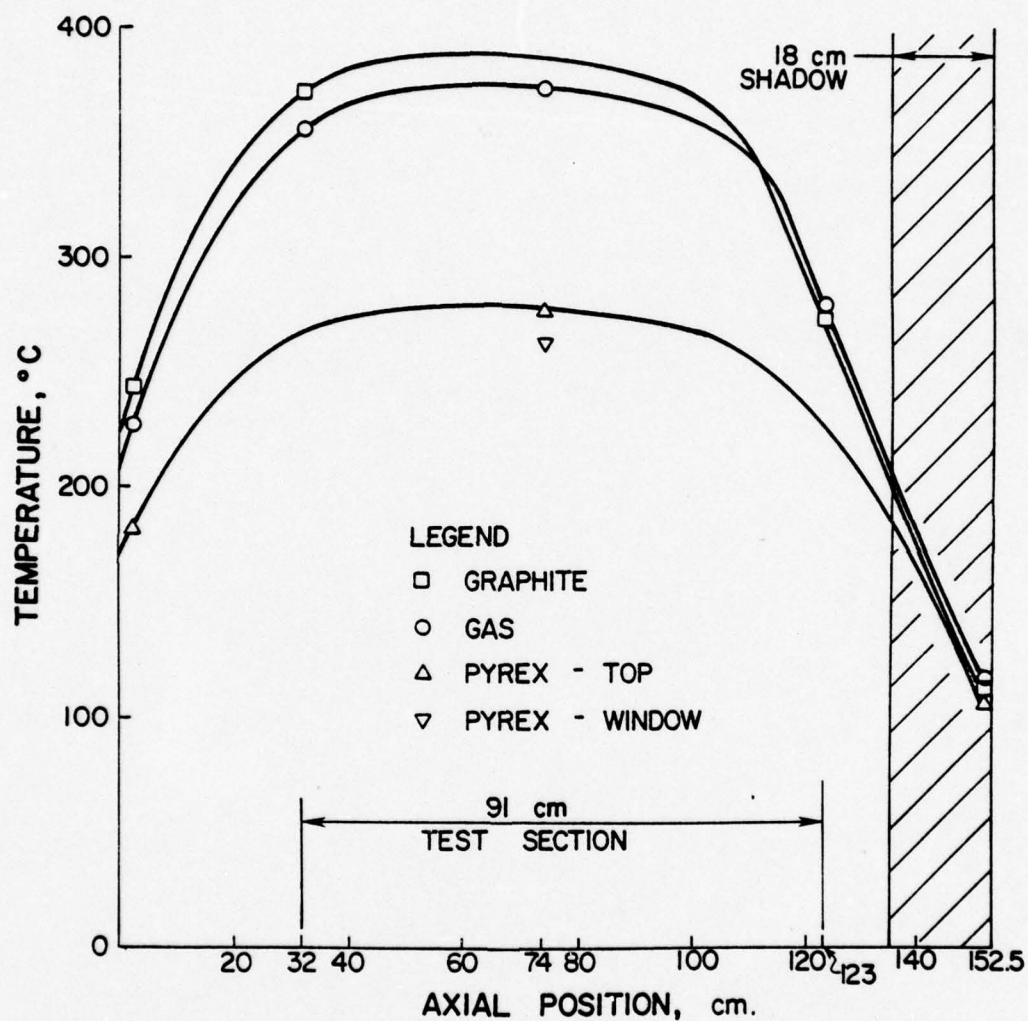
Figure 23. Steady-state stagnation temperatures of receiver measured on 14.V.77, 12:15 p.m. The direct solar flux was ca. 800 W m^{-2}, and the ambient temperature was 25°C.

CHAPTER IV

MATHEMATICAL MODEL (FLOWING GAS)

A. Introduction

One would like to be able to accurately predict the performance of this collector design in all possible configurations. Prior to such an attempt, a mathematical model of the device must be developed that adequately accounts for its observed behavior. In practice, the mathematical model was formulated in successive stages of complexity and refinement. William of Ockham's principle (i.e., the simplest model to account for observed phenomena is the most likely to represent the true situation) was observed.

As in Chapter II, the calculation method for asymptotic conditions is straightforward. This temperature occurs when the incoming solar flux is just balanced by the various thermal losses (i.e., there is no net heat gain by the gas which implies either gas exiting from an infinitely long collector or a static gas). Two principal loss terms were considered: radial heat conduction through the insulation surrounding the glass receiver, and re-radiation by the aperture, both by the glass and the asbestos sides.

A more detailed mathematical formulation is required for handling gas flows at various rates. Internal heat transfer modes

and their magnitudes must be considered. The laminar flow regime, tilt, and short length of the model create a situation far more intricate than that within the long full-scale device with its highly turbulent flow and small temperature gradients.

B. Stagnation (V = 0) Calculations

A number of subsidiary calculations and operations must be performed before formulating an expression for heat transfer within the device. These are discussed below.

1. Solar Flux Computation

The solar flux available to the device is determined as follows:

a. Flux bulb

The temperature difference across this instrument (described in Chapter III) is proportional to the direct solar flux at the reflector. Since the bulb is masked so that the absorber plate within it only "sees" the sun, and is at the same angle as the reflector, no corrections for the diffuse flux and tilt are necessary. Thus, using the one-dimensional heat conduction equation for the copper support rod (of the exposed plate):

$$q = (A_1 \, k \, \Delta T)/[A_2 (\alpha_S)_{25°C} \, L_1 (\tau_S)_{25°C}] \, ,$$

where the first area is the cross-sectional area of the support
rod, and the second is the area of the plate; the absorptance is
for the plate, while the transmittance is for the Pyrex bulb;
$\Delta T = T1 - T_\infty$.

Substituting in the appropriate values (see Table 4),

$$q = (\pi/4)(0.208 \text{ cm})^2 (10^4 \text{cm}^2 \text{m}^{-2})(3.89 \text{ W cm}^{-1} \text{ °C}^{-1})(\Delta T)/$$

$$(10 \text{ cm}^2)(0.39)(10.3 \text{ cm})(0.91)$$

$$= 36.4 \ (\Delta T) \text{ W m}^{-2} .$$

The selective radiative properties of copper have been used to
advantage here. The very low ε_{IR}, and near-ambient plate tempera-
tures permit neglecting the radiative loss from the plate.

b. Eppley pyranometer

Since it is essential to define the flux as accurately as
possible, an alternative approach is taken. The Pennsylvania State
University operates a U.S. Weather Bureau Station and measures the
total (2π steradian) horizontal flux with an Eppley pyranometer.
The accuracy of the particular instrument used is currently estimated
to be of the order of 95% (80), which is fairly typical (51). With
the horizontal flux reading one can calculate the perpendicular
flux from the solar altitude (defined here as the angle of the sun
above the horizon, i.e., 90° minus the zenith angle), and then the

direct component from an empirical correlation. A further overall
correction for non-perpendicularity of the array to the solar flux
is also made.

More specifically:

perpendicular total flux = (horizontal total flux)/sin θ

where the angle θ is the pertinent solar elevation in the vertical.
Here, a vertical rod and its shadow are used to find θ, i.e.:

$$\theta = \tan^{-1}(91.5 \text{ cm, vertical rod ht.})/$$

(measured rod horizontal shadow length, cm) .

The flux available at the mirror then becomes:

available direct flux =

(perpendicular total flux) · (1 – diffuse component) ·

(angular correction for non-perpendicular collector) .

The flux of diffuse sky radiation reaching the ground may be
computed by solving the equation of radiative transfer for a turbid
atmosphere. However, the problem is a demanding one (81) and theoret-
ical predictions of the diffuse component are inadequate at this time

(60,82). The relationship between diffuse and total radiation is best determined from empirical correlations. Liu and Jordan (82) developed such a correlation for Blue Hill, MA. This correlation has been widely used. Since it is based on data from only a single site, and employs the older value of the extraterrestrial solar constant (2.00 ly min^{-1}, which is ca. 3% higher than the more accurate current measurement (51)), it results in an underprediction of the diffuse component, when compared with other sites with similar climatological/geographical features (83). Some error also results (82) from the use of a monthly average to account for daily variation in the extraterrestrial solar constant.

More recently, Ruth and Chant (83) have suggested forming a correlation based on local conditions; the requisite data are not available for State College, PA. Their standard correlation, developed from four Canadian sites, can be used with only small error at other locations. Additional slight error is introduced when applying the correlation, which is based on daily fluxes, to hourly fluxes near noon here. But Orgill and Hollands (84) have shown, in their study of hourly diffuse/total solar flux radiation for Toronto, that the difference between daily (83) and hourly ratios is insignificant.

Tuller (85) found a linear relationship adequate for a similar Canadian data base, but only over a restricted range of values. To cover the full range of conditions encountered during the experiments

at The Pennsylvania State University, a computer program that calculates a polynomial expression to fit data by the method of least squares was employed. Ruth and Chant's standard correlation (83) was fitted to:

$$K_D = 3.01 - 6.85(K_T) + 4.19(K_T)^2 ,$$

with a reduced chi-squared value of 0.83×10^{-5}, for $0.65 \leqslant K_T \leqslant 0.83$, where the nomenclature is as in the references cited above, i.e.:

H = total insolation on a horizontal surface (measured here),

H_0 = extraterrestrial insolation on a horizontal surface,

H_D = diffuse insolation on a horizontal surface,

$K_T = H_D/H_0$,

and

$$K_D = H/H_0.$$

H_0 varies somewhat ($\pm$ 3%) from its annual average of 1353 W m^{-2} (51) because of the annual variation in the sun-earth distance. Although the plot of the flux over a year appears as a sinusoid (2), it will be represented here by a linear relationship, to sufficient accuracy for computing K_D.

2. Natural Convection Within Enclosed Aperture

During most experiments the receiver aperture was covered with a transparent Mylar film, for two reasons: to reduce convective losses from the hot aperture surfaces, and to permit a more accurate mathematical formulation. Although incorporation of a natural convection term in the heat loss equation for the first experimental model did not present any insuperable difficulties, it was a source of large error. The influence of the wind on a complex, tilted shape is difficult to quantify even if the wind direction and velocity are accurately measured.

With an enclosed aperture, there still exists the possibility of enhanced heat loss across it from natural convection cell formation within it. However, the presence of the hot Pyrex at the top of the enclosure tends to produce a stable system, i.e., no appreciable air motion.

Catton et al. (86) solved the two-dimensional equations of motion governing natural convection. A decrease in heat transport at the top of an enclosure was observed, when it was heated from above. The likely cause is density stratification, creating a stagnant, constant temperature layer adjacent to the heated top wall. While equations were developed for a finite Prandtl number fluid, a solution was determined only for a large Pr (i.e., high kinematic viscosity) fluid. Examination of the results for a slot of aspect ratio (length/height) of 20, at an angle of tilt = 60° shows that the Nusselt number = 1 to a Rayleigh number of ca. 10^4,

then the Nu climbs linearly (on a log-log plot) to ca. 4.5 at
Ra = 2 x 10^6 ((86), Figure 3).

The experimental investigations of Arnold et al. (87) and
Ozoe et al. (88) with inclined channels tend to corroborate the
analytical approach. Arnold et al. looked at several fluids, over
the Pr range of 4.5 (water) to 2000 (silicone oil), at various tilt
angles and aspect ratios. For a 45° tilted region, Nu = 1 at
Ra ≤ ca. 3 x 10^3, reaching about 4 at Ra = 4 x 10^6 on a log-log
plot. No effect of Pr on Nu was observed. Nu decreases with
increasing aspect ratio, up to the maximum aspect ratio of 12 inves-
tigated, with a 152 mm length.

Ozoe et al (88) performed experiments with air (Pr = 0.7),
at aspect ratios of 8.4 (2.15 cm height) and 15.5 (1.16 cm height)
and at many tilt angles, over 1770 < Ra < 37,150. Again, Nu began
increasing at Ra ≃ 3 x 10^3, reaching ca. 2 at Ra = 37,150 for the
8.4 aspect-ratio channel. The channels were quite wide, the width
being equal to the length. Eckert and Drake (89) report the results
of numerous experiments, but with the fluid apparently heated from
below, and find that geometry exerts only a minor influence on Nu.

Rayleigh numbers will now be calculated, for two extreme
temperatures observed in the present work. T19 was 261°C on
March 23, 1977 (stagnation condition), and 130°C on November 19,
1976 (flowing gas); these temperatures correspond to T_h, the tempera-
ture of the hot surface. A temperature of 25°C as T_c, the cold
surface temperature (Mylar), will be assumed. Ra is defined here as

$$Ra = Pr \ g \ \beta \ L^3 \ \Delta T/\nu^2 \ ,$$

where the properties of the air trapped within the aperture are evaluated at T_{film} (37), which is equal to $(T_h + T_c)/2$ here; $\beta = 1/T_\infty = 1/T_c$ (38), as in Chapter II.

Substituting in the appropriate values,

$$Ra_{T_f} = 143°C = (0.7)(9.8 \ m \ s^{-2})(143 + 273 \ °K)^{-1}(0.025 \ m)^3$$

$$(261 - 25°C)/(26.9 \ x \ 10^{-6} \ m^2 s^{-1})^2$$

$$= 8.4 \ x \ 10^4$$

and

$$Ra_{T_f} = 78°C = (0.7)(9.8)(78 + 273)^{-1}(0.025)^3(78 - 25)/(21.8 \ x \ 10^{-6})^2$$

$$= 3.41 \ x \ 10^4 \ .$$

The effect of the Transite sides has been ignored, and the height of the aperture (L in the definition of Ra) has been conservatively taken as 2.5 cm.

The two calculated Ra's, when compared with the above analytical and experimental results, indicate that probably $1 < Nu < 2$ ($Nu = 1 \rightarrow$ pure conduction). Thus, natural convection effects are small, and given the somewhat higher conductivity of the insulation

(compared to the conductivity of the air trapped in the covered aperture enclosure) they will be ignored here. That is, for the purpose of determining radial thermal losses, the receiver will be considered as if surrounded by 360° of insulation.

3. Radial Conduction Loss

A very efficient insulation was placed around the Pyrex receiver. Its conductivity varies appreciably with temperature, and a least-squares polynomial expression was fitted to the data (35) on its properties, i.e.:

$$k, W \text{ cm m}^{-2} °K^{-1} = 2.87 - 4.15 \times 10^{-3}(\bar{T}) + 1.76 \times 10^{-5}(\bar{T})^2 ,$$

where $\bar{T}$ is the mean insulation temperature, °K. This expression yields a reduced chi-squared value of 0.124×10^{-1}.

Since $R_o/R_i = (2.5 + 0.5 + 2.5)/(2.5 + 0.5) = 1.83$ is less than 2, an arithmetic average insulation area can be an acceptable approximation for use in computing the heat transfer. For greater accuracy, the logarithmic mean area, devined by Kreith (40) as:

$$\bar{A} = (A_o - A_i)/\ln(A_o/A_i)$$

$$= 2\pi(5.5 - 3.0 \text{ cm})(1 \text{ cm length})/\ln(5.5 \text{ cm}/3.0 \text{ cm})$$

$$= 25.9 \text{ cm}^2/\text{cm receiver length}$$

will be used here. The radial temperature drop across the 0.5
cm-thick Pyrex is very small and is ignored.

4. Radiation Losses

The so-called view factor characterizes the influence of
geometry on radiative heat exchange between two surfaces. The
diffuse view factor F_{A-B} from finite surface A to finite surface B
is defined by Özisik (90) as:

F_{A-B} = (Radiative energy leaving surface A that strikes B directly)/

(Radiative energy leaving surface A in all

directions in the hemispherical space)

For a very long enclosure where each surface is an isothermal,
diffuse reflector and diffuse emitter, the radiative exchange along
the longitudinal axis is negligible and the exchange becomes two-
dimensional. The stagnation condition approximates such a situation
quite well (Figures 22 and 23). Under flowing gas conditions there
is an axial temperature gradient, but it is too small (and the abso-
lute temperatures involved are too low) for appreciable axial radiative
exchange to be present. The low aspect ratio of the enclosed aperture
also precludes significant axial radiation (see following discussion).
Therefore, the approximation of essentially two-dimensional radiative

losses from the aperture surfaces will be extended to all cases. Hottel and Sarofim (91) present a simple method for calculating the two-dimensional view factors for an enclosure, and suggest its use in approximating a real engineering system.

This "crossed-string" method is applied to a long four-sided enclosure as follows (90,91). Imaginary strings are stretched between the corners (transverse section) and the view factor from surface A to B becomes:

F_{A-B} = [(sum of lengths of 2 crossed strings) -

(sum of lengths of 2 uncrossed strings)]/2 x length of side A

This is illustrated on Figure 24, which also shows the important receiver dimensions. Thus,

$$F_{A-B} = [(L_E + L_D) - (L_F + L_C)]/2 \cdot L_A$$

or

$$F_{A-B} = [(4.1 + 4.1) - (2.0 + 5.0)]/2(2.5) = 0.24 = F_{B-A} ,$$

by reciprocity. Similarly, $F_{A-C} = F_{B-C} = 0.68$, $F_{F-A} = 0.1$, $F_{F-C} = 0.80$, $F_{A-F} = 0.08$, and $F_{G-F} = 0.28$.
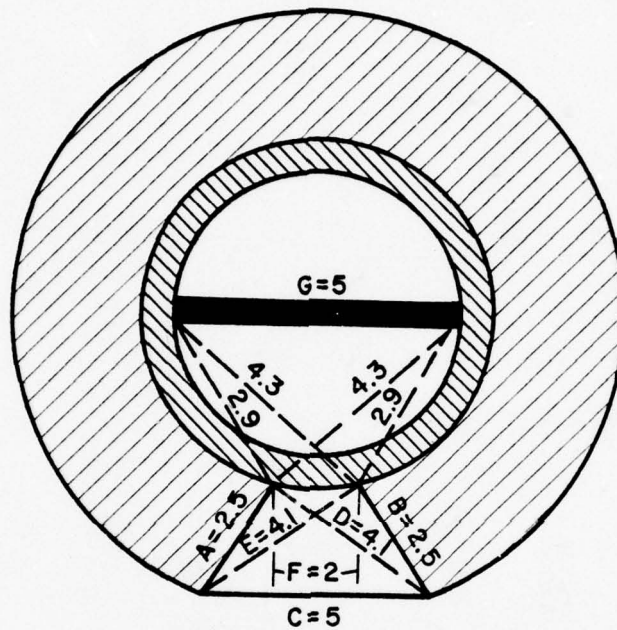
NOTE: ALL DIMENSIONS ARE IN CENTIMETERS (cm)

Figure 24. Receiver dimensions.

5. End Effects and One-Dimensional Approximation

The calculation is performed only at the center (axially) of the device where the temperature profile is flat, and the cooler ends are both distant. The effects of the axial dimension are therefore negligible. On the further approximation of peripherally isothermal conditions (at the Pyrex exterior, by use of an average temperature), the problem reduces to one dimension, with the view factor effectively incorporating two dimensions into one.

6. Energy Balance

The calculation is again (as in Chapter II) based on a 1-cm length of receiver. The total concentrated flux per cm of receiver length is:

$$q_S = (\rho_M)(W_M)(\text{no. mirrors})(1 - \text{pointing error})(1 - \rho_P)(1 - \rho_G \cdot F_G)$$

$$(\tau_{Mylar})(\text{meas. direct perpendicular flux at mirror}) \ .$$

This effectively delimits one control volume surface as the Pyrex aperture. The tilt of individual strips is not taken into account, since the maximum tilt is only 18°. Substituting in the proper values,

$$q_S = (0.80)(1.59 \text{ cm})(40)(1 \text{ cm length})(10^{-4} \text{ m}^2 \text{ cm}^{-2})(1 - 0.05)$$

$$(1 - 0.07)(1 - 0.13 \cdot 0.28)(0.85)(\text{flux, W m}^{-2})$$

= (3.67×10^{-3}) (direct perpendicular flux), W, per centimeter of length, which is available to the Pyrex receiver. At steady-state this is counterbalanced by the thermal losses, where

$$q_S = \sigma(\epsilon \ F \ A \ T^4)_P + \sigma(\epsilon \ F \ A \ \bar{T}^4)_w + k_{\bar{T}} \ \bar{A}(\bar{T}_p - \bar{T}_e)/\text{insulation tk.} \ ,$$

and where the first RH term represents the radiative heat loss from the glass window, the second term is the radiative loss from the aperture sides, and the last term is the loss by conduction through the insulation. It is assumed that $\bar{T}_w = (T_p + \bar{T}_e)/2 = (T19 + \bar{T}_e)/2$, where $\bar{T}_e = (T3 + T8)/2$, provides an adequate measure of the temperature of the aperture walls. This (linear) assumption probably somewhat underestimates the actual loss (because of the exponential), but this is mitigated by the poorer view factor of the hotter (i.e., nearer the glass) parts of the walls. Radiative exchange in the form of wall reradiation to the glass is ignored. The view factor is very small (0.08), and a conservatively high ϵ_p for the glass was selected (1.00), partly in order to compensate for any absorbed reradiation. $\bar{T}_p$, the average peripheral glass temperature, is taken as $(T16 + T7)/2$; i.e., the glass temperature is assumed to vary in linear fashion from its hottest points, where the graphite rests against it (taken as ca. = T16, at 9 and 3 o'clock) to the coolest points (T19, which = T_p, and T7) at 6 and 12 o'clock. The graphite temperature at the axial center of the device was not measured, but is probably only slightly higher than

T16, the gas temperature there (see Figures 22 and 23). Given its high thermal conductivity, the graphite ought to be isothermal, in the transverse direction.

The measured stagnation temperatures on March 23, 1977, at 12:00 p.m., were: T7 = 297°C, T19 = 261, T16 = 388, T3 = 25, and T8 = 30. That day was very windy, which lowered the T19 (i.e., glass window) reading, the thermocouple being relatively exposed. Thus T19, which is usually = T7, is here nearly 40°C lower, and will not be used in the calculation. Substituting the appropriate values,

$$(872 \text{ W m}^{-2})(3.67 \times 10^{-3}) \overset{?}{=} (5.67 \times 10^{-8} \text{ W m}^{-2} \text{ °K}^{-4})(1.00)(0.80)$$

$$(297 + 273°K)^4 (2 \text{ cm}^2)(10^{-4} \text{ m}^2 \text{ cm}^{-2})$$

$$+ (5.67 \times 10^{-8} \text{ W m}^{-2} \text{ °K}^{-4})(0.94)(0.68)(5 \text{ cm}^2)(10^{-4} \text{ m}^2 \text{ cm}^{-2})$$

$$[(297 + 28)/2 + 273°K]^4$$

$$+ (4.66 \text{ W cm m}^{-2} \text{ °C}^{-1})(2.6 \times 10^{-3} \text{ m}^2)[(388 + 297)/2 -$$

$$(30 + 25)/2]/2.5 \text{ cm}^2,$$

3.2 W ≃ 3.14 W, which is quite close.

If one attempts to calculate the convective loss from the receiver insulation to the ambient environment, a large error results. For example, with the above temperatures and a wind velocity = ca. 8 m s^{-1} (measured, at the Meteorological Station), the calculated convective heat loss from the external skin is 2.47 W. A well-known empirical equation (8) was used in obtaining this value; a cross-flow condition was assumed.

Since the true skin loss is seriously overpredicted, this loss has not been calculated in subsequent analyses. That loss should, of course, be equal to the conduction loss through the receiver insulation; the latter is readily and accurately determined. Because skin temperatures are generally only ca. 25°C above ambient (see Table 8), it is evident that the convective loss from the skin is not a limiting factor on receiver performance.

Selecting another date at random (but near the equinox, for minimal aperture shadowing/end loss), as March 9, 1977 at 12:00 p.m., with T7 = 281, T19 = 263, T16 = 367, T3 = 34, and T8 = 40, and again using T7 exclusively results in

$$3.17 \text{ W} \simeq 2.86 \text{ W} .$$

The losses (RHS) are a bit low for the flux, but the flux reading discrepancy between the two measurements was somewhat high (90 W m^{-2}). On another day, on which the two flux measurements were nearly equal, as on April 1, 1977, at 11:45 a.m., with T7 = 288, T19 = 281, T16 = 388, T3 = 44, and T8 = 45, one calculates

$$3.18 \text{ W} \simeq 2.94 \text{ W} .$$

The above calculations, using the actually measured stagnation temperatures, show that the main heat loss mechanisms have been correctly characterized. Agreement between the available solar flux and the sum of the losses is good, always within 10%. Considering the assumptions/approximations which have been made, and experimental error, this agreement is adequate for the purpose of calculating some of the losses under gas flow conditions.

C. Flowing Gas Calculations (Axial Bulk Temperature Profile)

1. Introduction

At steady-state, the three parameters that almost wholly determine the axial temperature profile of the fluid (i.e., T_b) along the receiver are gas inlet temperature, gas flow-rate, and available solar flux. The mathematical model that faithfully represents the experimental device should succedd in predicting the temperature profile from these initial conditions.

Two complications are now encountered:

(1) The axial temperature gradient present with gas flows provides a thermal driving force, so that axial conduction losses can no longer be ignored.

(2) An appreciable thermal resistance is offered by the laminar flow of the gas, resulting in a significant transverse temperature gradient.

These mechanisms must be elucidated and incorporated into the mathematical model. Because this flowing-gas model considers much of the receiver's (relatively short) total length, end effects/losses can exert an influence and must be thoroughly examined. Thus, the spectrum of heat transfer mechanisms that will now be investigated in detail includes:

(1) axial conduction;

(2) radiative end loss;

(3) effects of shape (semi-circular receiver) and tilt;

(4) development of velocity and temperature profiles;

(5) forced convection;

(6) natural convection.

Before proceeding further, some general remarks on the approach taken here are in order. A closed-form solution to the problem under consideration is clearly not available. The full set of mass, momentum, and energy conservation equations, under the conditions of developing flow and with buoyancy effects included, has not been solved at present, even by employing numerical techniques and adopting constant boundary conditions and other simplifying assumptions (92). Hence, it appeared pointless to attempt this approach, particularly in view of the coupled boundary

conditions and end effects in the experimental device. The solution
presented here has been constructed by utilizing investigations of
particular and separated aspects of the total problem. As these
interact to some extent, assumptions had to be made that would
take this interaction into account where necessary.

2. Axial Heat Conduction

The absorber and the glass receiver are relatively thick, and
the absorber has a high thermal conductivity. Axial heat conduction
by these two parts constitutes a significant loss at the inlet,
especially at low flows (high axial temperature gradient). It can
be computed by an iterative technique from the temperature profile,
which is first calculated without inclusion of this loss. The
conductivities are taken as constant; the absorber conductivity
is not accurately known, while the Pyrex has a relatively low
conductivity.

3. Radiation End Loss

Both the graphite absorber and the glass receiver have high
emittances at the temperatures attained by the collector. There is
therefore some heat radiated from the receiver test section to the
cooler end pieces, and the magnitude of the loss must be estimated.

Usiskin and Siegel (93) solved the applicable integro-
differential energy equation by three methods, but only for the
limiting case of pure radiation in a tube. Siegel and Perlmutter

(94,95) used part of this analysis in approximating the geometrical shape factors with a separable kernel, while considering combined convective and radiant heat transfer in a tube. This approach changes the energy equation to a second-order ordinary differential equation, which can be readily solved by numerical methods. Both tabulated and graphical solutions are provided (94,95), for a variety of conditions.

Thorsen (96), and Thorsen and Kanchanagom (97) performed experiments with air in narrow, long (L/D = 50) tubes at laminar flows and high heating rates (e.g., $T_w/T_{gas\ inlet}$ = 5 at the entrance and ca. 9.5 near the exit, while $T_{gas\ exit}/T_{gas\ inlet} \simeq 4.5$; the temperatures are in °F, with an inlet temperature of 500°F. Axial wall heat conduction and temperature profile development were studied simultaneously. The results are close to the theoretical predictions of Siegel and Perlmutter (94,95): internal wall radiation exchange with the tube ends is limited to ca. the first and last 20% of tube length (L/D = 50), with the greater loss near the exit. The influence on the Nusselt number over the first 80% of the tube length is slight (96,97). The high Nu resulting from flow development near the entrance reduces the wall temperature, and decreases the radiative end loss there.

Now an experiment with high inlet and outlet temperatures and a high solar flux is selected, as on March 19, 1977, 1:30 p.m. (Table 8), where T14 = 120°C, T17 = 281, and the flux was 872 W m^{-2} with a flow rate of 32.3 liter min^{-1}. Here the temperatures and

other parameters at the 32 and 123-cm axial positions are chosen
as representative of the receiver inlet (0-cm position) and outlet
(152-cm position), respectively, and are used in the calculations
that follow. The reason for this approximation is that the 32 and
123-cm parameters are well-known from computer results. This approx-
imation is conservative at the receiver inlet, because the temperature
at the 32-cm position is considerably higher than that at 0-cm; at
the receiver outlet, the 123-cm and 153-cm temperatures differ only
by a small amount, so the approximation is quite valid there (Table 8).
The influence of four parameters, as defined in (95), must be
examined:

a. Stanton number

The Stanton number, S, is defined as $4\ Nu/Re \cdot Pr$. Here,
$Re = 554$, $Ra = 354 \rightarrow Re \cdot Ra = 1.96 \times 10^5$ (taken from computer
results; see Appendix II) and $(Nu_c)_{45°}/(Nu_f)_{0°} = 0.27(Re \cdot Ra)^{0.16}$
(see discussion on combined convection, below). Thus
$(Nu_c)_{45°}/(Nu_f)_{0°} = 1.90$, indicating a 90% enhancement of heat
transfer by natural convection effects. Also, $z^+ = z/D_h\ Re_D\ Pr =$
32 cm/$(2.86\ cm)(554)(0.67) = 0.030$, resulting in a $(Nu_f)_{0°} \simeq 5.2$
(see discussion on developing flow, below), versus 4.36 without
development effects, in a circular tube. Therefore the actual
Nusselt number = $(5.2)(1.90)(4.09/4.36) = 9.3$, where the fraction
corrects for a lower Nu (i.e., 4.09) in a semicircular sector tube.
The Stanton number can now be computed:

$$S = 4(9.3)/(554)(0.67) \simeq 0.10$$

When this value is compared with the results of Perlmutter and Siegel (95), it is evident that radiant losses are low. Although only the range of $0.005 \leq S \leq 0.02$ is shown ((95), Figure 4(a)), the radiative end loss is relatively insensitive to variation in the Stanton number over this range. The loss is negligible in the 60% central length of tube; extrapolation to $S \simeq 0.10$ should yield similar results. Near the receiver exit, S would be ca. 0.05 because of a lower Nu at that position. Also, the results (95) are given for a tube with L/D = 50, whereas the experimental device had L/D = 152 cm/ca. 1.5 cm → L/D > 100. Furthermore, the wall temperature shown (95) is approximately double the measured wall temperature here. Thus, the receiver's length and (relatively) low wall temperature serve to decrease the Stanton number influence on the theoretically predicted (95) radiative end losses, for the date selected. Since the variation in the Stanton number for all experiments is small, it can be assumed that the radiant loss over the central 60% of the receiver tube can be neglected.

b. Dimensionless heat transfer coefficient

The dimensionless heat transfer coefficient, H, is defined as $H = (h/q)(q/\sigma)^{0.25}$. Here, $q = (872 \text{ W m}^{-2})(3.67 \times 10^{-3} \text{ m}^2 \text{ cm}^{-1})$ $(0.53) = 1.7 \text{ W cm}^{-1}$ length (the 0.53 is the calculated Solar Utilization Factor, or SUF, defined here as q_N/q_S; the above calculation yields q_N). $h = \text{Nu} \cdot k/D_h = (9.3)(2.23 \times 10^{-4} \text{ W cm}^{-1} \text{ °K}^{-1})/2.86 \text{ cm}$ $= 7.25 \times 10^{-4} \text{ W cm}^{-2} \text{ °K}^{-1}$. H can now be calculated:

$$H = [(7.25 \times 10^{-4} \text{ W cm}^{-2} \text{ }^\circ\text{K}^{-1})(25.7 \text{ cm}^2 \text{ cm}^{-1})/1.7 \text{ W cm}^{-1}] \cdot$$

$$(1.7 \text{ W cm}^{-1}/25.7 \text{ cm}^2 \text{ cm}^{-1} \cdot 5.67 \times 10^{-12} \text{ W cm}^2 \text{ }^\circ\text{K}^{-1})^{0.25} = 3.6$$

This high (95) convective heat transfer coefficient reduces the potential radiative loss and again limits it to 20% of the tube length, at the inlet and outlet ((95), Figure 4(b)). The possible variation (experimental) in H is small, so this conclusion holds for all experiments.

c. Dimensionless gas inlet temperature

The dimensionless gas inlet temperature, $T_{g,i}$, is defined $T_{g,i} = (\sigma/q)^{0.25} T_i$, where T_i is the gas inlet temperature. Here,

$$T_{g,i} = (5.67 \times 10^{-12} \text{ W cm}^{-2} \text{ }^\circ\text{K}^{-1} \cdot 25.7 \text{ cm}^2 \text{ cm}^{-1}/1.7 \text{ W cm}^{-1})^{0.25}$$

$$(120 + 273^\circ\text{K}) = 1.2$$

As before, the effect of this parameter is small, and it exerts an influence only over the first and last 20% of tube length ((95), Figure 4(c)). Because of the exponential, little variation is possible in $T_{g,i}$ over the range of experimental measurements.

d. Dimensionless reservoir temperature

$T_{r,e}$, the dimensionless reservoir temperature at the exit (assumed in (95) to be equal to the gas exit temperature), is defined by

$$T_{r,e} = (\sigma/q)^{0.25} \, T_{g,e} \; .$$

Here,

$$T_{r,e} = [(5.67 \times 10^{-12})(25.7)/(3.2)(0.12)]^{0.25}(281 + 273) = 2.5$$

(the 0.12 above is the SUF). Again, the influence of this parameter is low, limiting radiative losses to the entrance and exit ((95), Figure 4(d)). The exponential limits excursions from the particular value calculated.

The combined effect of all four of these parameters, at about the values calculated above, results in a radiative loss at the inlet of probably < 6%, and < 10% at the outlet ((95), Table 2(b)). These losses are mainly radiated by the first and last ten tube diameters. A selective absorber in the receiver produces even lower losses (94). Since subsequent analysis is restricted to the central 60% (i.e., 32-to-123 cm length) of the receiver, radiative end losses over this receiver portion can be neglected with very small error. Both the heat transfer surface (wall) and fluid temperatures in the central portion of a long tube (L/D > 50) have been shown to be nearly equal to those in pure convection, even for a wall emittance = 1 (94).

Because the radiative (I.R.) properties of the absorber and Pyrex are not known with sufficient accuracy to warrant consideration of radiative exchange within the receiver, this added complexity has

not been included in the mathematical formulation. On purely
theoretical grounds incorporation of the radiative interchange is
desirable, since only in this manner can the peripheral wall tempera-
ture distribution be determined. A single, average peripheral wall
temperature will therefore be used in the present formulation, to
determine the heat transfer both to the gas and to the ambient
environment. This approximation slightly overestimates the losses
(see Figure 25).

4. Receiver Shape

Of all the simple geometric shapes, a circular cross section
in a tube yields the highest convective heat transfer coefficient.
Exact analytical solutions for the coefficient are extant. Under
the conditions of fully developed laminar flow of a constant-property
fluid, with constant peripheral wall temperature, the Nusselt number
for a constant axial heat input is 4.36. Under the same conditions,
but with a constant axial wall temperature instead of a constant
axial heat flux, Nu = 3.64 (98). The lower Nu results from the
decreasing temperature difference between the wall and fluid, as the
latter proceeds through the tube.

A semicircular cross section evinces poorer overall heat
transfer because of relatively stagnant flow in the corners. With
conditions as before, and a constant axial heat flux, a closed-form
analytical solution for Nu is available. Sparrow and Haji-Sheikh (99)
obtained a solution of the momentum and energy equations from analogous
torsion and thin-plate deflection solutions, respectively, in solid

Figure 25. Typical temperature profiles of receiver. Measured on 17.III.77, 1:00 p.m., at a direct solar flux of 852 W m^{-2}, a flow rate of 38.7 1 min^{-1}, and an ambient temperature of 11°C.
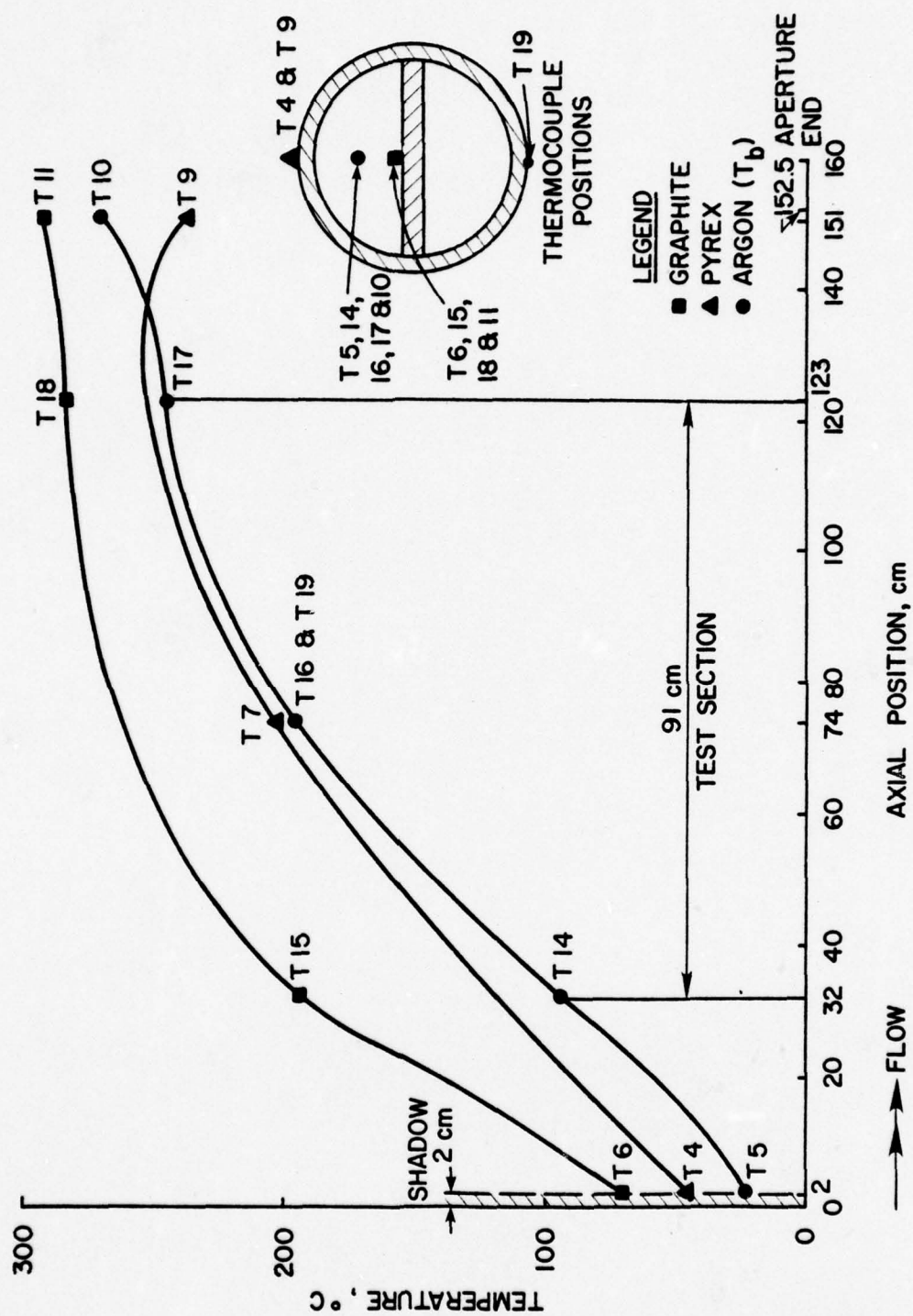
mechanics (98). These equations have also been solved by an alternate approach, employing a computer routine that constructs orthonormal functions (100). Both solutions gave identical results: Nu = 4.09. Solutions for circular sector ducts with an opening angle < 180° are in excellent agreement with the experimental data for air (101). As the circular-sector opening angle approaches 180° (a semicircle), two effects are noted: an increasing symmetry of the velocity and temperature profiles in the half-angle plane (99,100), and a decreasing difference in the Nusselt numbers obtained for the cases of peripherally varying heat flux and peripherally varying wall temperature (100).

Before the above results can be used with confidence, the three assumptions that were made in the solutions must be justified. These are:

a. Constant peripheral wall temperature

The Pyrex and graphite are relatively thick, and the graphite has a high thermal conductivity. The graphite strongly reradiates the solar flux incident on it; any portion of the incident flux striking the insulation is diffusely reflected. The Pyrex also reradiates strongly. With these high heat transfer rates in the transverse plane of the receiver, any variations in the peripheral temperature distribution should be small. The peripheral temperature variation was not measured per se, but comparison of T7, T19, and T16 (this last approximates the graphite temperature near the axial center of the receiver) under flow conditions gives some idea of its magnitude (Figure 25 and Table 8).

Reynolds (102) considered a circular tube, as described previously. The governing differential energy equation is linear. This permits superposition of simpler solutions for the solution of a complex circumferential heat flux variation. For example, for $q = q_0 (1 + 0.1 \cos \alpha)$, describing a $\pm$ 10% sinusoidal heat flux variation, the computed circumferential temperature variation $T_{max}/\bar{T} = 1.22$, with a local (i.e., circumferentially varying) Nusselt number. If, instead, the computation is repeated with $Nu = 4.36$ (constant circumferential wall temperature assumed), $T_{max}/\bar{T} = 1.10$, for an error of $(1.22 - 1.10)/1.22 \simeq 10\%$. The experimental peripheral temperature variation observed (again, compare T7, T19, and T16) is generally less than the $T_{max}/\bar{T} = 1.22$, above, so any error introduced by this approximation should be small. In any case, an average wall temperature is used in the flow calculations, reducing this potential error to negligible proportions.

b. Constant axial heat flux

Although the solar flux entering the receiver, per unit length, is constant axially, the actual flux input into the flowing fluid is not. As the fluid heats, losses mount so that eventually an asymptotic condition is reached with no net heating taking place. Over the central 91-cm portion the temperature rise of the heat transfer surfaces is fairly linear (Figure 25); however, the convective coefficient varies. Still, this condition approximates more closely, over the studied length, a constant axial heat flux boundary condition than a constant axial wall temperature (the only other case

extensively studied (103)). The error introduced by this simplifi-
cation is difficult to quantify. The effect of a decreasing heat
flux in the flow direction, as in the experimental device, is to
yield a somewhat lower heat transfer coefficient (i.e., higher
actual wall temperature → greater losses). Kays (104) shows that
the effect, qualitatively, for a sinusoidally (0 → maximum → 0)
varying axial heat flux is relatively minor. It will be ignored
here.

c. Fully developed flow

A fluid entering a pipe at uniform temperature and velocity
requires many tube diameters before the fully developed velocity
and temperature profiles become established; the profiles are
invariant thereafter if either the heat flux or the wall tempera-
ture are constant axially. For laminar flow, the approximate length
necessary for a fully developed velocity profile is equal to
$D \cdot (Re/20)$ (105). For a gas (Pr = 0.7), the temperature profile
develops somewhat more rapidly. Thus, a significant amount of
profile development takes place over the receiver length and must
be evaluated separately.

5. Development of Velocity and Temperature Profiles

Although the classical analysis of temperature profile develop-
ment in laminar flow was made by Graetz in 1885 (106), little
additional work on this topic was performed until the mid-1950's.
Sellars et al. (107) extended the classical solution to allow

consideration of more complex boundary conditions. Kays (108)
was the first to treat this problem in detail.

An exact analytical solution for a developing velocity field
in a circular tube has not been derived (109). Hence, solutions
of the temperature and velocity fields in forced convection are
derived from approximate analytical or numerical techniques.
Langhaar (110) obtained a solution for the developing axial
velocity profile (in the radial, or transverse, plane) by linear-
izing the nonlinear inertia terms in the momentum equation. Kays
(108) introduced this velocity profile into the energy equation
and solved it by a finite difference (i.e., numerical) method.
Nusselt numbers versus length are given for constant axial wall
temperature and constant axial heat flux, and for both fully
developed and developing velocity profiles, for the case of a
constant-property fluid in a round tube. A uniform circumferential
wall temperature was assumed. Sparrow and Lin (111) refined
Langhaar's (110) approximations, but obtained a velocity field
that closely matches that of the earlier solution.

The boundary layer equations can be solved with fewer assump-
tions than were made above if axial transport of vorticity is
neglected, and the pressure is taken as a function only of axial
length. Finite difference techniques were employed by Hornbeck
(112), Christiansen and Lemmon (113), and Schmidt and Zeldin (114)
to obtain the developing velocity profile. The results are in good
agreement with each other and with Langhaar's profiles, establishing
confidence in their validity.

Ulrichson and Schmitz (115) considered heat transfer with simultaneous development of temperature and velocity profiles of an incompressible viscous (Newtonian) fluid (Pr = 0.7, i.e, a gas). The boundary conditions of constant axial heat flux and constant axial wall temperature were used. The solution represents a refinement of the work of Kays (108), who ignored the radial velocity component. Langhaar's (110) axial velocity profile was employed, together with the radial profile obtained form the continuity equation, in a numerical solution of heat transfer rates. The results show that the local Nusselt number near the entrance is overestimated by about 6% if the radial velocity is neglected, for the case of constant axial heat flux.

Manohar (116) solved the non-linear momentum equation by an iterative technique to obtain the velocity profile. This velocity distribution was inserted into the energy equation, which was solved numerically for the temperature profiles. The computed heat transfer closely matches that of Ulrichson and Schmitz (115) and experimental data. Very recently Hong and Bergles (117) treated a semicircular tube problem by the methods of successive over-relaxation and finite differences. However, their heat transfer investigation was limited to the condition of a fully developed velocity profile.

The work of Manohar (116) is the most recent and apparently provides the most accurate results, and will be used here. A least-squares-fit equation to Manohar's Nusselt numbers for a constant axial heat flux condition is:

$$Nu = 4.18 + 3.17 \times 10^{-2}(z^+)^{-1} - 3.67 \times 10^{-5}(z^+)^{-2}$$

$$+ 1.91 \times 10^{-8}(z^+)^{-3}$$

for a reduced chi squared value of 1.81×10^{-2}.

An additional comment can be made now, on the constant axial heat flux assumption discussed previously. The boundary condition of the receiver, although closer to the constant axial flux case, is actually delimited by this and the constant axial wall temperature case. Over the experimental range, Kays' (108) values of Nusselt number for the constant wall temperature case were only ca. 15% lower than for the constant heat flux case. Manohar's (116) constant wall temperature solution deviates appreciably from that of Kays: Nu for the constant wall temperature is ca. 30% lower than for constant heat flux. Therefore, use of the more recent data, under the above assumption, carries a somewhat higher risk of error. At any rate, the error from this assumption is probably << 30% of the Nusselt number. The computed Nusselt number is used to calculate the difference between the gas and wall temperatures, with losses determined from the latter. Thus, the axial temperature profile is relatively insensitive to an error in the Nusselt number.

6. Combined Forced-Free Convection

Fluid motion may be on occasion strongly influenced by the presence of gravity, with the magnitude of the induced body force

field proportional to the local fluid density. The classical example is free convection, where fluid motion in an otherwise quiescent fluid occurs as a consequence of distortions in the body force field caused by density gradients. At the other extreme is the type of flow referred to as (pure) forced convection, whose behavior is unaltered by gravity. Most real forced flows are influenced to some extent by the gravity force. When the gravitational effect is significant, this flow is classified as combined forced-free convection. A measure of the relative magnitudes of forced and free convection can be obtained by comparing the Reynolds number with the Rayleigh number, as these are defined in the nomenclature. When the Rayleigh number is of the same order of magnitude as the Reynolds number, free convection effects are significant and cannot be ignored in a precise heat transfer analysis (118).

Combined free and forced laminar convection has been studied extensively in the past only for the two limiting cases of vertical and horizontal tubes. The paucity of inclined-tube studies obligates a discussion of the vertical and horizontal results.

a. Combined convection in vertical tubes

The orientation of the tube axis is important in combined forced and free convection. Combined convection in vertical tubes can be considered a special case of combined convection in inclined tubes. In vertical tubes the buoyancy forces are parallel to the direction of forced motion and some form of axial symmetry (rotational symmetry, for the round tubes generally studied) of the velocity and

temperature fields is retained, as in pure convection. This considerably simplifies the heat transfer analysis, and approximate analytical solutions are possible, just as for the forced convection condition (119).

Most of the theoretical studies posited constant axial heat input, constant peripheral wall temperature, fully developed flow, the usual flow idealizations, constant (both transverse and axial) fluid properties, and laminar flow. Only the density, and that solely in the buoyancy terms of the momentum equation, is taken as variable. The last is a common simplification of the governing equations, and is considered acceptable when the density is primarily a function of temperature (120). Iqbal and Stachiewicz (121) considered a fully variable density in the analytical expressions and determined that this has an insignificant effect on the resultant heat transfer coefficients (Nusselt numbers).

Hallman (122) performed an analysis and compared it with experimental data obtained by others; his theoretical Nusselt numbers were about 20% higher than the experimental ones. Tao (123) formulated a solution in terms of Bessel and associated functions, and found the heat transfer coefficients for circular and semi-circular tubes to be about the same. Iqbal et al. (124,125,126, 127) obtained solutions by the methods of finite differences (124), variational calculus (124,125,126), and a point matching method in terms of a series containing Bessel functions (127). Aggarwala and Iqbal (128) utilized analogous solutions from membrane vibration

problems. The duct shapes considered (124-128) included triangular, rectangular, rhombic, and others; Nusselt numbers were obtained for $0 <$ Rayleigh number $< 10^5$ (based on D_h, i.e., eight times that used in this thesis). It was found that as the Ra_D increases, the Nusselt number becomes relatively insensitive to the duct shape. When $Ra_D > 10^3$, all solutions converge rapidly (124,127). Incorporation of a wall (i.e., heat transfer surface) of finite thickness and peripheral (axial ignored) conductivity into the analysis indicated that the Nu decreases as the peripheral wall heat conductivity decreases (125).

Nayak and Cheng (129) solved the applicable equations by a finite element method, with results for triangular and square ducts as above. Muntjewerf et al. (130) performed experiments with two different oils in rectangular ducts, but only at very low Reynolds numbers (Re ≤ 100).

A more complex treatment, including developing flow and temperature profiles, was given this problem by a number of researchers. Worsøe-Schmidt and Leppert (131) solved the boundary-layer equations via a finite difference scheme, and found only slight improvement in heat transfer due to free convection in the developing flow region. Lawrence and Chato (132) used a finite difference method to solve the equations, and also performed experiments with water. The theoretical and experimental results correlate well; to obtain this good correlation, both the density and the viscosity had to be considered as nonlinear functions of the temperature. From the results, it

was concluded that the temperature and velocity profiles never become fully developed.

Experiments with nitrogen gas at high temperatures (900°K) over $10^3 < Re < 3.5 \times 10^3$ and Grashof number (based on D^3 and $\Delta T = T_w - T_b$) over 3×10^4 to 8×10^5 were performed by Biggs and Stachiewicz (133). A comparison of the experimental Nusselt numbers with Kays' (108) forced convection solution showed that at values of $z^+ < 0.008$ (corresponding to a z/D of about 18) there is good agreement. It was therefore concluded that, in this inlet region of developing flow, the effects of free convection are largely suppressed. At values of $z^+ > 0.008$ the Nu increased sharply above that given by Kays, which is indicative of significant free convection effects in this region. Maitra and Raju (134) wrote the momentum and energy equations for an annulus in terms of Kelvin functions, then approximated these by polynomial expressions. Experiments were also performed with water in a brass-glass annulus over $2 \times 10^3 < Ra < 3 \times 10^5$ (based on D_h) and Re from 200-1200. The experimental Nusselt numbers were about 45% greater than theoretical at $z/D_h > 10$. In the entrance region, experiments showed that fully developed flow was established at $z^+ \simeq 1.5 \times 10^{-3}$. In the same region, at high Rayleigh numbers, the experimental Nusselt number was greater than the theoretical Nu by a factor of approximately five. This runs counter to the conclusions of Biggs and Stachiewicz (133) discussed above.

b. Combined convection in horizontal tubes

In a horizontal tube with appreciable heating (of a low-viscosity fluid) the warmer fluid near the wall is less dense than the rest of the fluid and an upward motion near the tube wall is imposed on the forced axial motion. The fluid far from the wall is cooler and denser, so it has a downward component of motion. For the vertically oriented tube, this results only in a distortion of the forced-convection axial velocity profile. But for a horizontal tube a secondary motion is established which is symmetrical about a vertical plane passing through the tube axis (Figure 26). The resultant flow is helical, and additional mixing takes place within the fluid. Heat transfer is enhanced thereby.

Ede (135) was probably the first to gather experimental data from many sources, including his own work, for combined convection of water and also air, in tubes of various diameters. The water data is fairly consistent, but large errors are present in the air data so that no meaningful results were obtained. Two effects were noted: a consistent relation between the Nusselt and Grashof numbers, and a substantial variation in the temperature over the tube periphery.

An early attempt at a theoretical analysis of combined horizontal convection was made by Morton (136), using a perturbation method with $Nu \cdot Gr/Re$ as the expansion parameter. Truncation error was large, ca. 10% by $Re \cdot Ra = 3000$, and only low heating rates were assumed. Even so, the velocity and temperature distributions, and
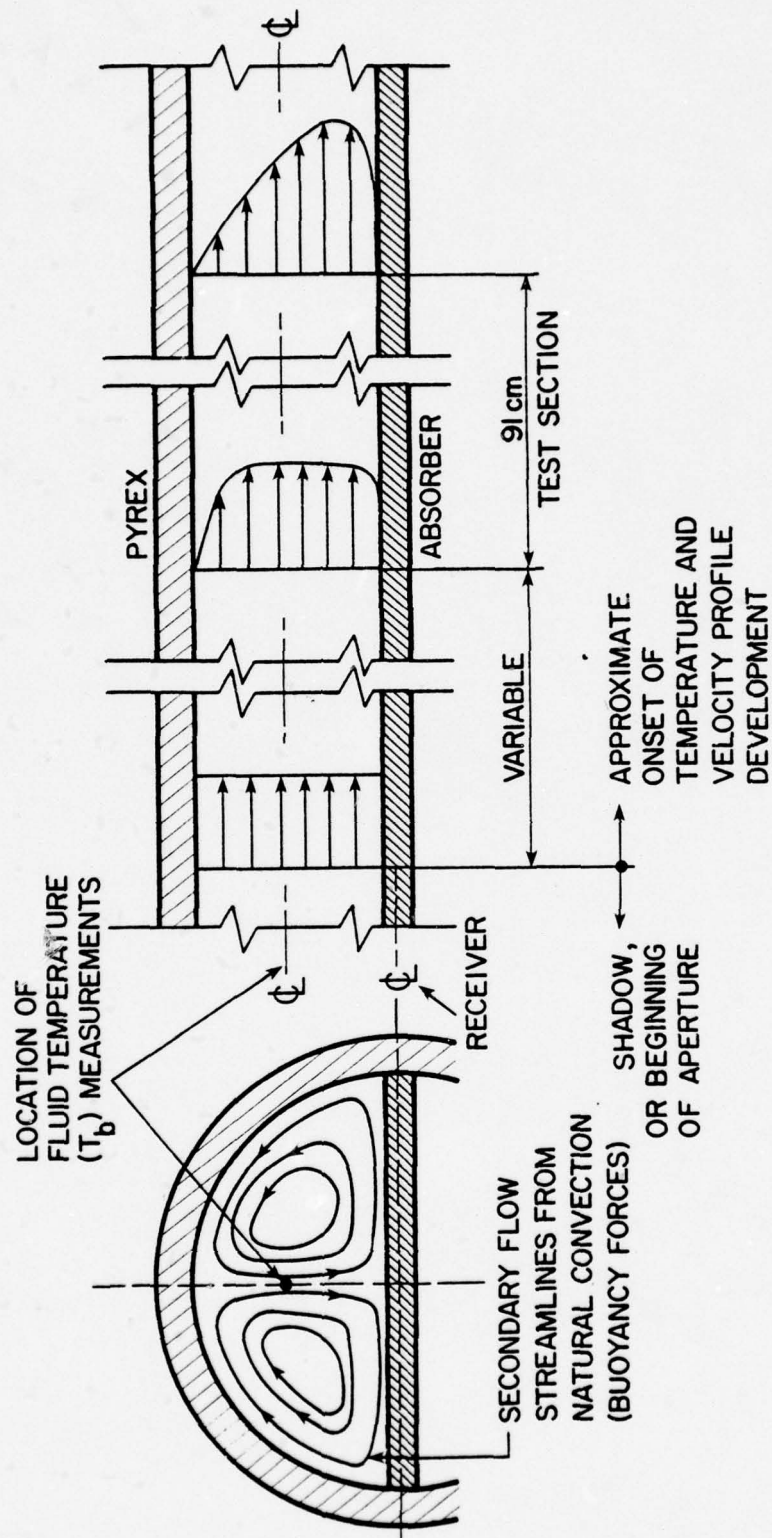
Figure 26. Temperature and velocity profiles (theoretical).

the Nusselt number, were found to be functions of the product of the Reynolds number and the Rayleigh number, for a given Prandtl number. The inadequacy of the pure convection solution for low laminar flow rates, even at a small heating rate, was demonstrated; distortion of velocity and temperature profiles was also observed.

The above-noted aspects of combined convection were extensively studied by Mori et al. (137) in an experimental program that included laminar and turbulent flows. A 35.6 mm I.D. tube was used, with air as the fluid; its properties were taken as variable in calculating Re and Ra. A Rayleigh number of ca. 40 resulted from a heating rate on the order of 0.1°C/(cm tube length), which is much less than that measured during the solar collector experiments here. Significant distortions in the temperature and velocity profiles were noted, with the temperature profile affected to a greater extent. Turbulent flow at Re > 10^4 overwhelmed the incipient secondary flow, so that the profiles and heat transfer were essentially unaffected by buoyancy. In laminar flow, enhanced heat transfer from free convection appeared at about Re $\cdot$ Ra = 10^3, and increased substantially thereafter. An empirical correlation formula for calculating the combined convection Nusselt number was determined.

Mori and Futagami (138) continued this study, on a theoretical basis. A boundary layer approximation was applied, yielding axial temperature and velocity profiles that are distorted by buoyancy forces but deviate somewhat from the experimental values. However, the approximation was considered valid as Re $\cdot$ Ra becomes very large;

the calculated Nusselt numbers agree quite well with the experimental data reported by Mori et al. (137). The calculated equation for the enhanced Nusselt number is

$$Nu = Nu_0(0.1634)(Re \cdot Ra)^{0.2} \text{, for } Pr = 0.72 \text{ .}$$

The perturbation analysis of Faris and Viskanta (119) gave very similar Nusselt numbers; however, the analytical transverse profiles of the axial velocity and temperature components were flatter than the experimental profiles of Mori et al. (137). But the Nusselt numbers from experiments with water in small (2.5 cm dia.) tubes obtained by Newell and Bergles (120) are considerably lower than those of Mori et al. (137) for air.

The typical downward distortion and flattening of the transverse profiles as a result of free convection were shown to take place in similar fashion in non-circular channels. Cheng and Hwang (139), using a method of successive over-relaxation of the governing finite difference equations (this approach diverges at low Re · Ra), analyzed rectangular and square channels. The velocity and temperature profiles evinced the expected distortion. Also, Hong and Bergles (140) in their analysis found that temperature-dependent viscosity (i.e., Pr) can exert a strong influence on theoretical heat transfer results.

The problem of combined free and forced convection and entrance effects (i.e., thermally and hydrodynamically developing

flow) has received some attention in the last decade or so. All the studies unfortunately assume (theoretical), or have (experimental), fully developed velocity profiles, so that only thermal development is treated. These studies were severely limited in scope and by their assumptions, and disagree widely. Therefore, the study results cannot be utilized here directly. Still, some trends are evident and must be taken into account, at least qualitatively.

Shannon and Depew (141,142) performed experiments with both water and ethylene glycol, in small (< 1 cm dia.) tubes, and at Grashof numbers (based on D^3) to 2.5×10^5. Their heat transfer results, based on locally-measured fluid properties, indicate that the Nusselt number begins to depart from the pure convection case quite early. The Nu reaches a minimum as flow progresses yet remains above the pure convection value, and then deviates sharply from the latter (which becomes asymptotic) by reversing its previous trend and now increases with the axial dimension. The effect is more pronounced at higher Gr. The Nusselt number test data scatter was $\pm$ 25%, and the results from water were below the ethylene glycol values; backflow was postulated to account for the difference.

Very similar experiments with water and/or ethylene glycol have been performed by Morcos and Bergles (143), Bergles and Simonds (144), and Hong et al. (145). A large variation in peripheral wall temperature, to 50°C between the top and bottom of a glass tube (145), was observed in these experiments. The results exhibit a substantial

amount of scatter, but indicate that very near the entrance the Nusselt number is the same as in pure forced convection. Farther along, the Nusselt number curve (plotted versus axial distance) branches out and approaches a constant value that is a function of the Rayleigh number. Development of the temperature profile is rapid, requiring a decreasing length of tube as the Rayleigh number increases.

Finite difference analyses, which use a high-Prandtl-number-fluid assumption (i.e., primary axial flow is unaffected by the secondary flow) so that the inertia terms in the momentum equation can be neglected, give results in good agreement with the experimental data for water (145). Cheng et al. (92), and Cheng and Ou (146) compared their theoretical results with the experimental data reported by others and found reasonable agreement, considering the scatter in the experimental data. Cheng et al. (92) also noted a dip, or minimum, in the theoretical Nusselt number as flow progresses, before the asymptotic or fully developed value is attained.

Of greater relevance to the present analysis are the experimental results with air as the heat transfer medium. McComas and Eckert (147) investigated the range of $100 < Re < 900$ and $Gr < 1000$ (based on D^3), but in a small (ca. 1 cm dia.) tube. Gas properties were evaluated at the local axial temperature. At higher Grashof numbers, the local (axial) Nusselt numbers at first followed the forced convection results as flow progressed, then deviated and became constant at a higher level - which was a function of the Gr.

A slight dip was observed in the Nu versus axial position curve, but only at low Re; the peripheral temperature variation was practically nil.

A wider (25.4 mm I.D.) tube was used by Hussain and McComas (148). A peripheral temperature variation of up to 7°C for a wall-to-bulk temperature difference of 28°C occurred in the upper Grashof number range (ca. 5×10^4, based on D^3). Heat transfer results were somewhat puzzling: at Re < 1200 the asymptotic Nusselt number was lower than that for pure forced convection. This may have been caused by exit end effects. For Re > 1200, enhanced heat transfer was observed, and agreement with the data of Mori et al. (137), who studied a narrower Rayleigh number range, is quite good. But the empirical correlation of Mori et al. (137), discussed earlier, appears to overpredict the Nu at higher Ra.

c. Combined convection in inclined tubes

Only a few studies on inclined tubes are extant; flow development with combined convection has not been studied in inclined tubes. Iqbal and Stachiewicz (118,121) calculated the temperature and velocity fields by a perturbation method. This method gives unrealistically high estimates of the Nusselt number at even moderate values of Re · Ra (ca. 10^3) (145). The results of that study (118), to Re · Ra < 3×10^3, not only give erroneous values of Nu, but also show the occurrence of a maximum in the Nu at an inclination angle between 20-60°. All other studies indicate that the combined heat transfer is a maximum at an angle of 0° (i.e., horizontal tube) where interaction between primary and secondary flow is maximized.

Recently Hwang and Cheng (149) approached the problem of combined convection in horizontal tubes by a combination of line iterative and boundary vorticity methods. The calculated transverse profiles of the axial temperature and velocity match the experimental data of Mori et al. (137) rather well, to a considerably greater extent than the theoretical results of Mori and Futagami (138). This numerical method has been applied to inclined tubes by Cheng and Hong (150), with solutions obtained by a combined boundary vorticity/iterative relaxation method of the governing equations, which are written in finite difference form. The greatest distortion of temperature and velocity profiles is shown to occur in a horizontal tube, and it decreases with inclination angle. Heat transfer results show a similar trend. For a gas (Pr = 0.75) and a circular tube at an inclination of 45°, the Nusselt number was found to depend on the Rayleigh number and the Re · Ra product, to Ra ≤ ca. 450 (for Re · Ra < 5 x 10^4). At larger Rayleigh numbers, the Nu becomes independent of Re and is a function of Ra only. This numerical solution checks exactly with the known numerical results for the horizontal and the vertical tube.

The experiments of Sabbagh et al. (151) with a gas in an inclined tube were an attempt to corroborate the theoretical results discussed above. Although qualitatively the experimental data are similar to the theoretical results, they are seriously flawed since even the Nusselt number obtained at 0° inclination is much greater than measured by Mori et al. (137): 7.85 versus ca. 5.6. The

measured temperature and velocity profiles are also very different from those calculated by Cheng and Hong (150).

Better results were obtained by Futagami and Abe (152) in a simultaneous experimental/theoretical study. They were able to correlate results at various angles (α) of inclination using as a correction factor the cosine of α. For example, the temperature and velocity profiles, for inclination angles of 0° and 45° and at Re · Ra cos α = 8 x 10^4, are nearly identical. A comparison was made with the analytical heat transfer results of Hwang and Cheng (149) discussed earlier. Even though those results were for a horizontal orientation, reasonable agreement was found with the values obtained by Futagami and Abe (152), when plotted against Re · Ra cos α as a parameter.

Inclined rectangular channels of aspect ratios = 0.5, 1.0 (square cross section), and 2.0 were examined by Ou et al. (153) in a numerical analysis. A Prandtl number of 5 (i.e., water) was used throughout. Results for various inclinations were correlated through the use of a trigonometric function in the Ra and Re calculations. The results clearly indicate that the effect of cross-sectional shape, over the range studied, was negligibly small. This justifies the use here of circular-tube results for the semicircular receiver-halves.

In summary, given the paucity and variability in the above studies, a certain subjective judgmental factor enters into the choice of the results to be used herein. It was decided to base

the heat transfer coefficient from combined convection on the
theoretical work of Cheng and Hong (150). Because that work does
not adequately cover the full Re · Ra range encountered here, the
studies of Hwang and Cheng (149) in the low Re · Ra range, and
Hussain and McComas (148) in the intermediate Re · Ra range are
also used. Since the last two were derived for horizontal tubes,
the correction cos α of Futagami and Abe (152) is incorporated
into those results (Figure 27). The complete set of expressions
defining enhanced heat transfer from natural convection is:

$$(Nu_c)_{45°}/(Nu_f)_{0°} = 0.27(Re \cdot Ra)^{0.16}$$

$$\text{for Re} \cdot \text{Ra} < 2.75 \times 10^5 , \qquad \text{(after (149))}$$

$$(Nu_c)_{45°}/(Nu_f)_{0°} = 2.0$$

$$\text{for Re} \cdot \text{Ra} \geqslant 2.75 \times 10^5 , \qquad \text{(after (148))}$$

and

$$(Nu_c)_{45°}/(Nu_f)_{0°} = 0.31(Ra)^{0.27}$$

$$\text{for Ra} \geqslant 1000 , \qquad \text{(after (150))}$$

where $(Nu_c)_{45°}$ is the Nusselt number in combined convection, at an
inclination angle of 45°, and $(Nu_f)_{0°}$ is the Nusselt number in pure
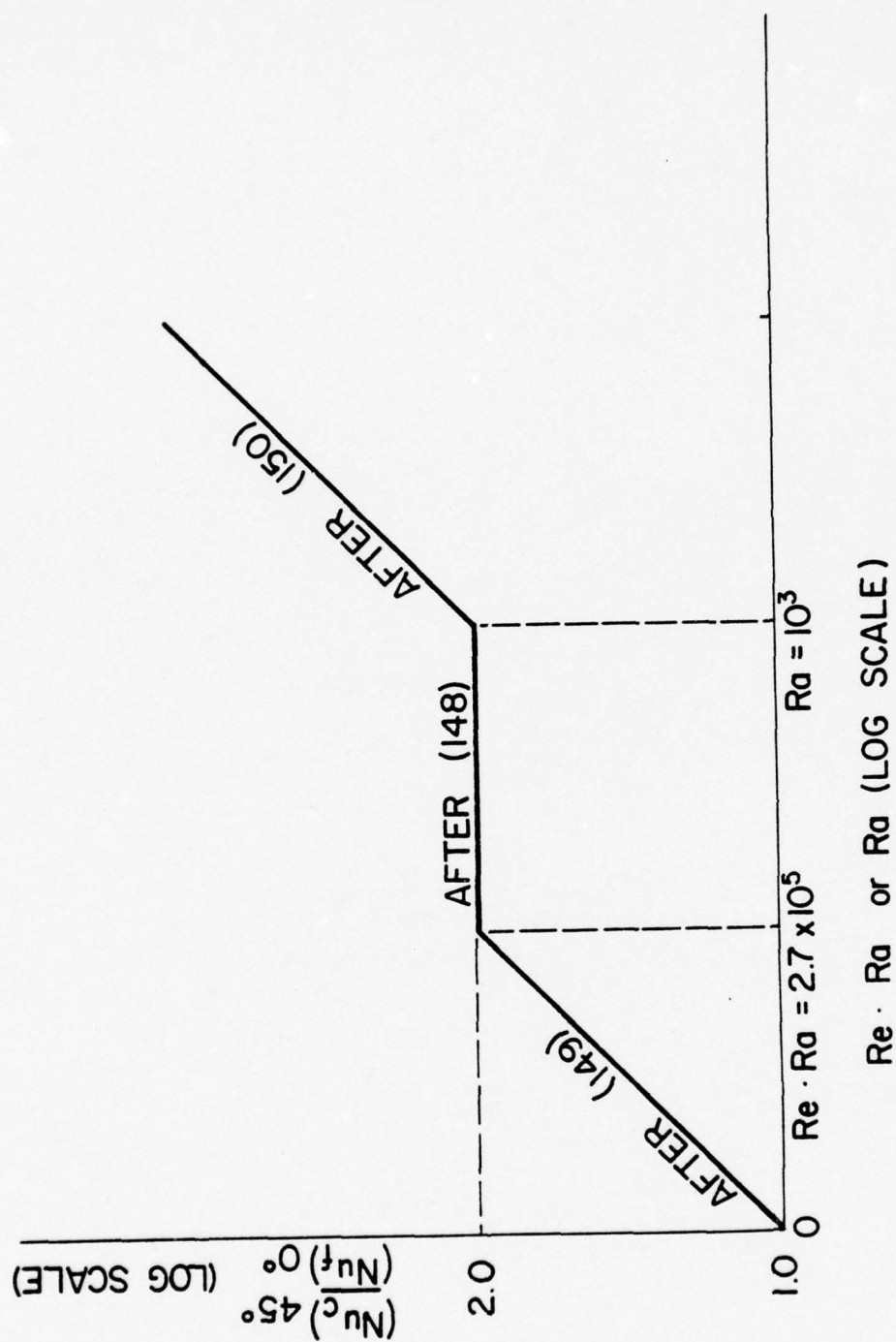
Figure 27. Nusselt number ratio.

forced convection in a horizontal tube. These expressions were
incorporated into the mathematical model in such a way that there
was no overlap among them (Figure 27).

A number of hand calculations were performed in order to
support the choice of the above expressions. Data from experiments
with the solar collector were used as input. It was determined that:

(1) The cross-sectional shape of the receiver can be ignored
(i.e., the Nu ratio above is the same, for circular and semicircular
tubes). Two calculations were made by integrating temperature and
velocity profiles, taken from Cheng and Hong (150), in the definition
of the bulk fluid temperature, T_b. The difference in the calculated
bulk temperatures for a semicircular and circular cross section was
only ca. 3% at the Re and Ra values typically measured.

(2) The difference between calculated and measured $\bar{T}_w - T_g$,
for various flow rates and at all axial positions was quite small.
The ratio $(\bar{T}_w - T_b)_{calc.} / (\bar{T}_w - T_g \text{ meas. at centerline})$ spanned the
range 0.8-1.0, with most values clustered near 1.0. The experi-
mental $\bar{T}_w$ was found by using the temperature distributions in the
Pyrex and the graphite as discussed earlier; i.e., it can be shown
that $\bar{T}_w = 0.7 \, T_{graphite} + 0.3 \, T_{Pyrex}$. The good agreement between
calculated and measured results permits several conclusions to be
drawn:

(a) The Nusselt numbers are reasonably accurate.

(b) The measured gas temperature, T_g, which is measured at a point in the vertical center of the upper half of the semicircular receiver, closely represents the bulk, or mean mixed, fluid temperature T_b. Such would not normally be the case, except when the temperature and velocity profiles are completely flat; the ratio of $(\bar{T}_w - T_b)/(\bar{T}_w - T_{g\ at\ centerline})$ for fully developed profiles is not negligible. Here, the downward distortion in the velocity and temperature profiles is sufficient to nearly offset the large variations in temperature and velocity encountered in the transverse plane of the receiver. This is so because the measured centerline fluid temperature is actually on the shoulder of the profile, rather than at its minimum (Figure 26).

Strictly speaking, these conclusions apply only to the upper half of the semicircular receiver, where all temperature measurements were made (because of the concentrated solar flux in the lower receiver half, no thermocouples were placed there). It will be assumed here that the heat transfer processes within the lower half are quantitatively, if not qualitatively, very similar. Therefore, the measurements made consistently represent the true thermal energy level of the heat transfer fluid, i.e., $T_{g\ at\ centerline} \simeq T_b$. This eases the computation enormously.

7. Energy Balance

a. Introduction

Since the gas used (Ar) is transparent to solar and thermal radiation, it heats by convection only. The driving potential for its heating is the difference between the gas and (averaged) wall temperatures; this difference can be calculated if the Nusselt number is known. The radial losses, consisting of conduction through the insulation and radiation from the aperture, are purely a function of the wall temperature if an external (i.e., skin) temperature is known or posited. The axial conductive loss, mainly along the absorber, can be determined from the rate of axial temperature change.

b. Energy balance equations

An energy balance is now made on a small ($\simeq$ differential) control volume (see Figure 28):

$$q_N = \dot{m} \, C_p (dT_b/dz) = q_S - q_L - q_{C2} \, ,$$

or, in finite difference form

$$\dot{m} \, C_p [(T_b)_m - (T_b)_{m-1}] = q_S - \{\sigma(\bar{T}_w)^4_{m-1} + \sigma[((\bar{T}_w)_{m-1} + \bar{T}_e)/2]^4\}$$

$$- k_{insul.}[(\bar{T}_w)_{m-1} - \bar{T}_e] - (k_P + k_G)[2(T_b)_m - (T_b)_{m-1} - (T_b)_{m+1}]$$
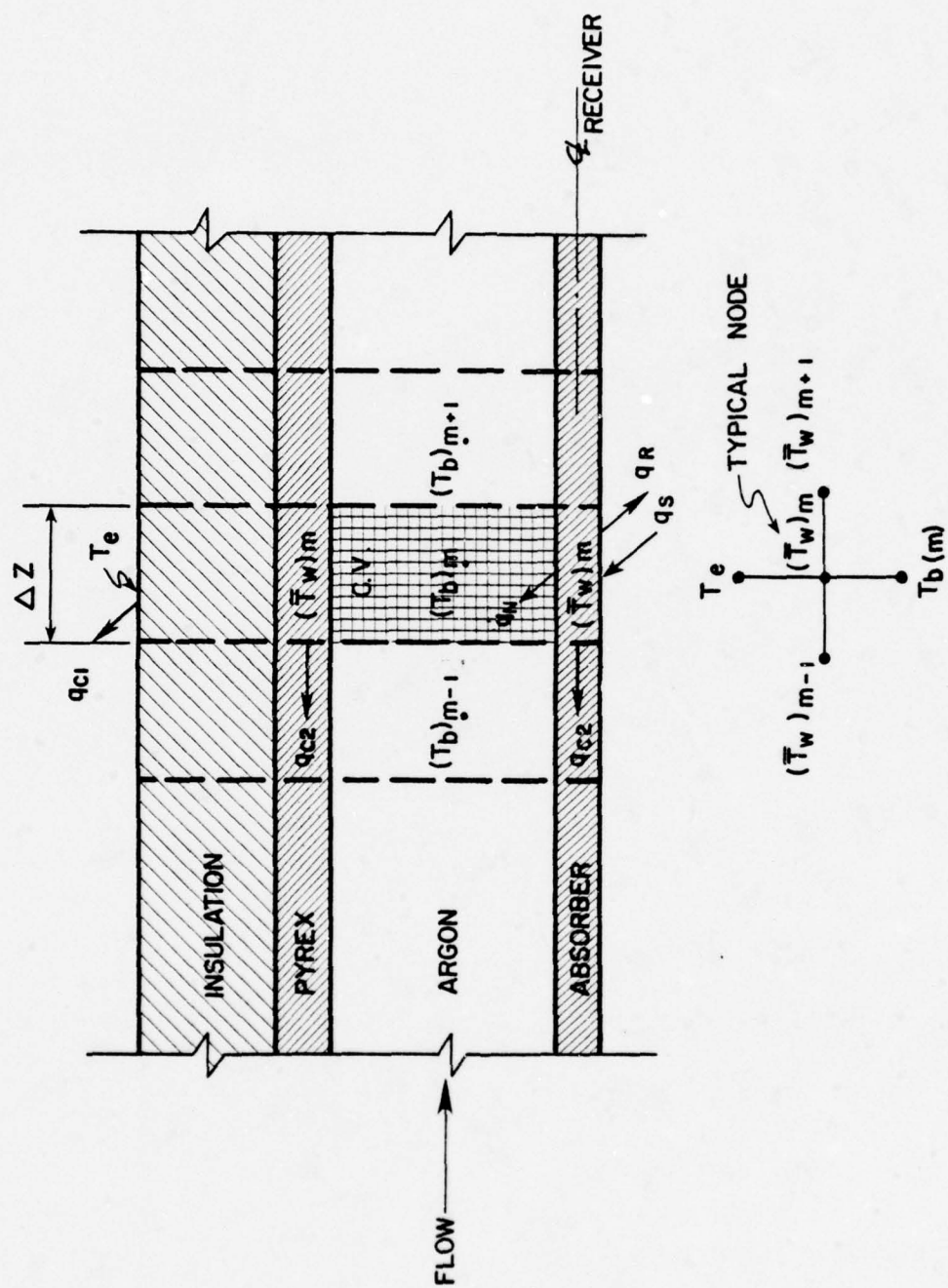
Figure 28. Energy balance.

where the first term on the R.H.S. represents the available concentrated solar flux at the Pyrex window; the second is the radiative loss from the aperture, both from the Pyrex and the aperture sides; the third is the loss through the insulation; the last term represents the axial conduction loss, by the Pyrex and the absorber. For clarity, the appropriate view factors, areas, and radiative properties are not shown in the equation. The problem is a two-dimensional one, with the first two loss terms essentially consisting of (one-dimensional) radial losses. The second, axial, dimension enters through the axial conduction loss term.

As described earlier, $\bar{T}_w$ is now the average peripheral wall temperature of Pyrex + graphite. $\bar{T}_w$ is obtained (except at the first step; see Appendix I) by solving the governing equation for the convective heat transfer within the collector:

$$q_N = \bar{h}(\bar{T}_w - T_b)_{m-1} \, ,$$

where $\bar{h} = Nu \cdot k/D_h$. All the parameters except $\bar{T}_w$ are known or can be calculated.

There are two unknowns, $(T_b)_m$, which is being solved for, given the known or calculated $(T_b)_{m-1}$, and $(T_b)_{m+1}$; there is only one equation. A second equation must now be written for an additional step, i.e.,

$$\dot{m} \, C_p [(T_b)_{m+1} - (T_b)_m] = q_S - \{\sigma (\bar{T}_w)_m^4 + \sigma [((\bar{T}_w)_m + \bar{T}_e)/2]^4\}$$

$$- \, k_{insul.} [(\bar{T}_w)_m - \bar{T}_e] - (k_P + k_G)[2(T_b)_m - (T_b)_{m-1} - (T_b)_{m+1}]$$

A typical node is illustrated on Figure 28. Two additional approximations were made in the equations (nodes), to make them manageable:

(1) The solution would not converge when the wall temperatures were used in computing the axial loss. Thus, it was necessary to replace these with the gas temperatures, i.e., $(\partial^2 \bar{T}_w / \partial z^2) \simeq (\partial^2 T_b / \partial z^2)$, or

$$[2(\bar{T}_w)_m - (\bar{T}_w)_{m-1} - (\bar{T}_w)_{m+1}] \simeq [2(T_b)_m - (T_b)_{m-1} - (T_b)_{m+1}] \; .$$

An examination of the experimental data (Figure 25) shows that this is a reasonable approximation.

(2) The axial conduction loss term is the same in both equations used in the solution, so as not to introduce new unknowns, i.e., now

$$(\partial^2 \bar{T}_w / \partial z^2) \simeq (\partial^2 T_b) / \partial z^2) \simeq \text{constant} \; ,$$

over the two steps. Again, examination of the data (Figure 25) reveals that the slope of the temperature profile changes slowly, so the approximation is valid.

Two further assumptions common to this type of problem are made:

(1) Friction can be ignored because of smooth surfaces and low velocities.

(2) Viscous dissipation and compressibility effects can be neglected (154,155), again because of the low velocities.

The two equations considered can now be readily solved by an iterative approach. A simultaneous solution is precluded by the difficult nonlinear terms.

c. Computational method

A computer program was written in the FORTRAN IV language, and the program was executed on a PDP-9 computer. The program exceeded the computer's memory storage capacity and had to be subdivided into three parts. The program was executed rapidly; the relatively slow mechanical printer was the limiting factor on run time.

The program performs an energy balance on a 1 cm-long control volume of the receiver and calculates the axial bulk temperature profile of the receiver over the 32-to-123 cm length. The two equations mentioned are solved iteratively at each step, until the solution converges on a predetermined value. The bulk temperature profile itself is calculated by a forward-one numerical integration of the equation, with the solution marching on from the initial

conditions at the 32-cm axial position. The main features of this program are:

(1) Use of actual gas properties at the T_b of the control element under consideration. The argon properties are tabulated by Hilsenrath et al. (156), with some properties also listed by Ražnjević (157). Properties are evaluated at T_b to yield a minimal error in determining the heat transfer (37).

(2) Inclusion of enhanced heat transfer due to both developing flow and buoyancy. Each effect is assumed to act independently of the other (i.e., no coupling present).

(3) Consideration of axial heat loss at the inlet by conduction in the graphite and glass.

In the actual computation, the program (see Figure 29 and Appendix I):

(1) Determines the average direct flux, from the two measurements described earlier.

(2) Calculates the argon flow rate.

(3) Calculates gas properties and Nu's from the T_b of the previous step.

(4) Calculates thermal (transverse only) losses.

(5) Calculates T_b.

161
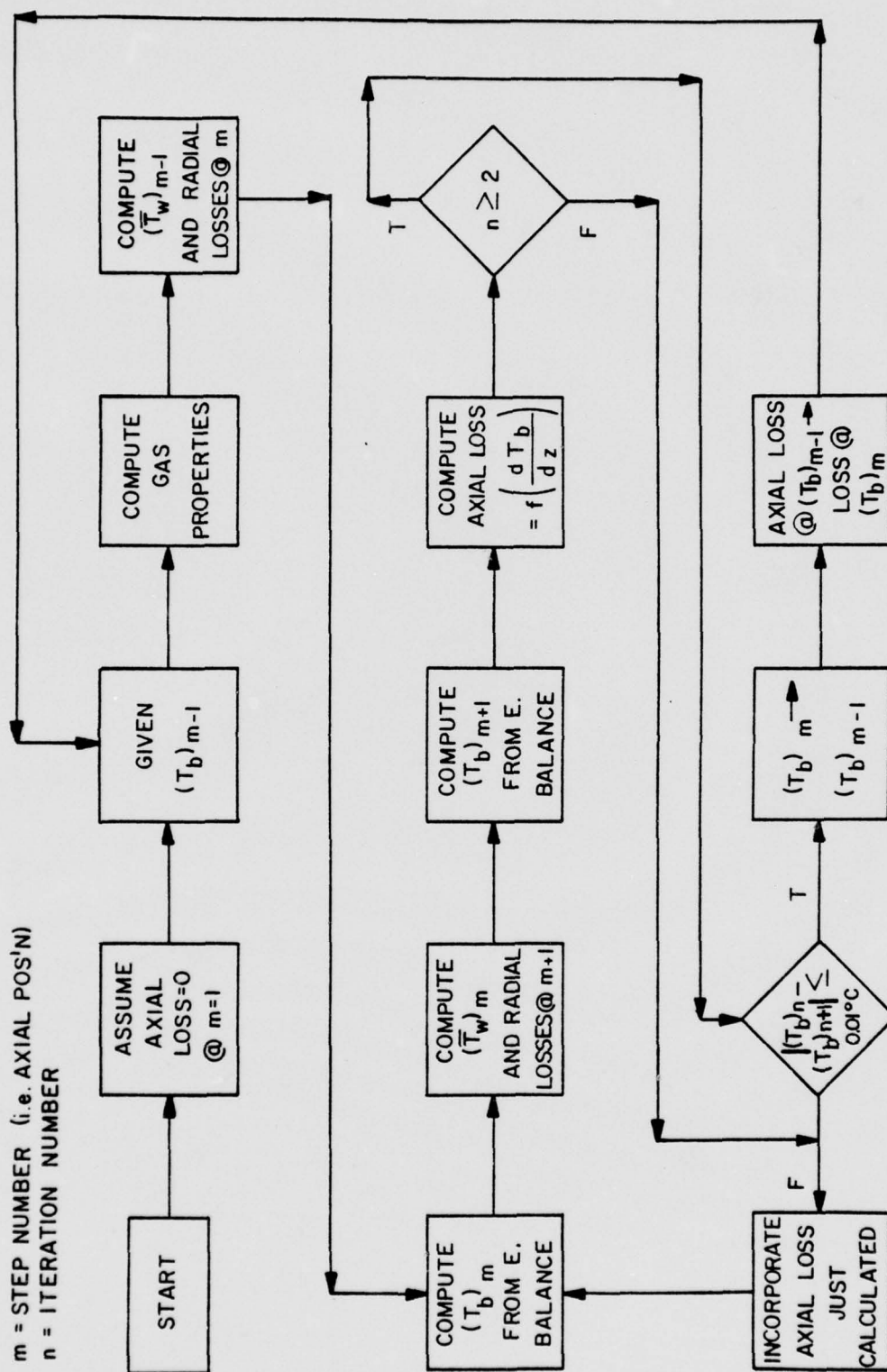
Figure 29. Computer program flow chart.

(6) Repeats (4) and (5) for an additional step.

(7) Computes an axial conductive loss from the temperature gradient difference between the two steps.

(8) Iterates (5), (6), and (7) until the solution converges within 0.01°C. The axial loss from (7) is now included in calculating the T_b in (5).

(9) Goes on to the next step and begins at (3) again.

d. Stability and convergence

It is possible for some small error (e.g., round-off error) to increase as the computation progresses. The instability can cause the error terms to completely overshadow the desired solution, making it worthless.

Karplus (158) used an electrical circuit analog of finite difference equations to determine the criteria for stability. A typical node in the solution was considered; if the node is stable (i.e., its analog serves to dissipate rather than supply energy to other nodes, in response to an excitation) then the entire network must be stable. When the finite difference equation is put in a form with all the terms on one side, the stability criteria become:

(1) If all the coefficients of the finite difference expressions are positive, then the equation is always stable.

(2) If some coefficients are negative, the Σ coefficients must be < 0 as a sufficient condition for stability.

Here, the terms in the energy balance equation can be rearranged, and it is apparent that all the coefficients of the finite difference expressions are positive. The equation and its solution are therefore unconditionally stable. The control element size (i.e., the number of steps, or subdivisions, in the computation) is thus determined purely from considerations of accuracy in a trade-off against computer time (159).

The normal control element size selected was 1 cm, with a convergence criterion of 0.01°C for the iterative solution of the axial conduction loss. A fair number of calculations were repeated, with an element size of 0.01 cm and convergence on 0.001°C. Execution time was greatly lengthened, and the temperatures were only slightly higher than those normally calculated. The difference was between 1-7°C, and provided no better agreement with the experimental data, so the less stringent approach was adopted.

Lax's (160) equivalence theorem states that, given a properly posed initial value problem, and a finite difference approximation to it that satisfies the consistency condition, stability is a necessary and sufficient condition for a convergent approximation. A problem is taken as properly posed if a family of genuine solutions exists, and if the solutions depend uniquely and continuously on the initial data (161). For consistency, the truncation error → 0

as the element size → 0. Since both these conditions appear to be satisfied here, and no problems with convergence beyond those described earlier were encountered, the solution is assumed convergent.

D. Results of Computation

1. Graphite Absorber

The results of several typical computations, together with the actual experimental measurements in parentheses, are shown in Appendix II and Figures 30-32. Agreement between the experimental and calculated temperatures is quite good here, but becomes rather poor at the higher flow rates as previously discussed in Chapter III, Section E (see also Figure 33). The influence of flow rate, flux, and inlet temperature on the temperature profiles is apparent. The efficiency of heat utilization is, as one might expect, high at first (the SUF, a measure of thermal efficiency, is above 0.6 for two of the runs illustrated in Appendix II), but decreases rapidly as the gas heats and losses mount. By the end of the test section it is only 0.04-0.23, indicating that little additional heating can take place farther downstream. The average wall temperature profiles parallel the graphite absorber temperature profiles (measured graphite temperatures shown in parentheses) but are somewhat lower because of the inclusion of the glass receiver temperature in the average. There is some error present in the flux measurements/calculations

Figure 30.   Temperature profiles on 19.XI.76, 12:30 p.m.   The direct solar flux was
647 W m^{-2}, the flow rate was 11.9 l min^{-1}, and the ambient temperature
14°C.   Because of the very low flow rate (Re $\approx$ 175):   (1) The gas
conductivity (axial) was probably not negligible, and served to flatten
the measured profile.   (2) The calculation would proceed to completion only
with the smaller control volume element (0.1 cm long) discussed.
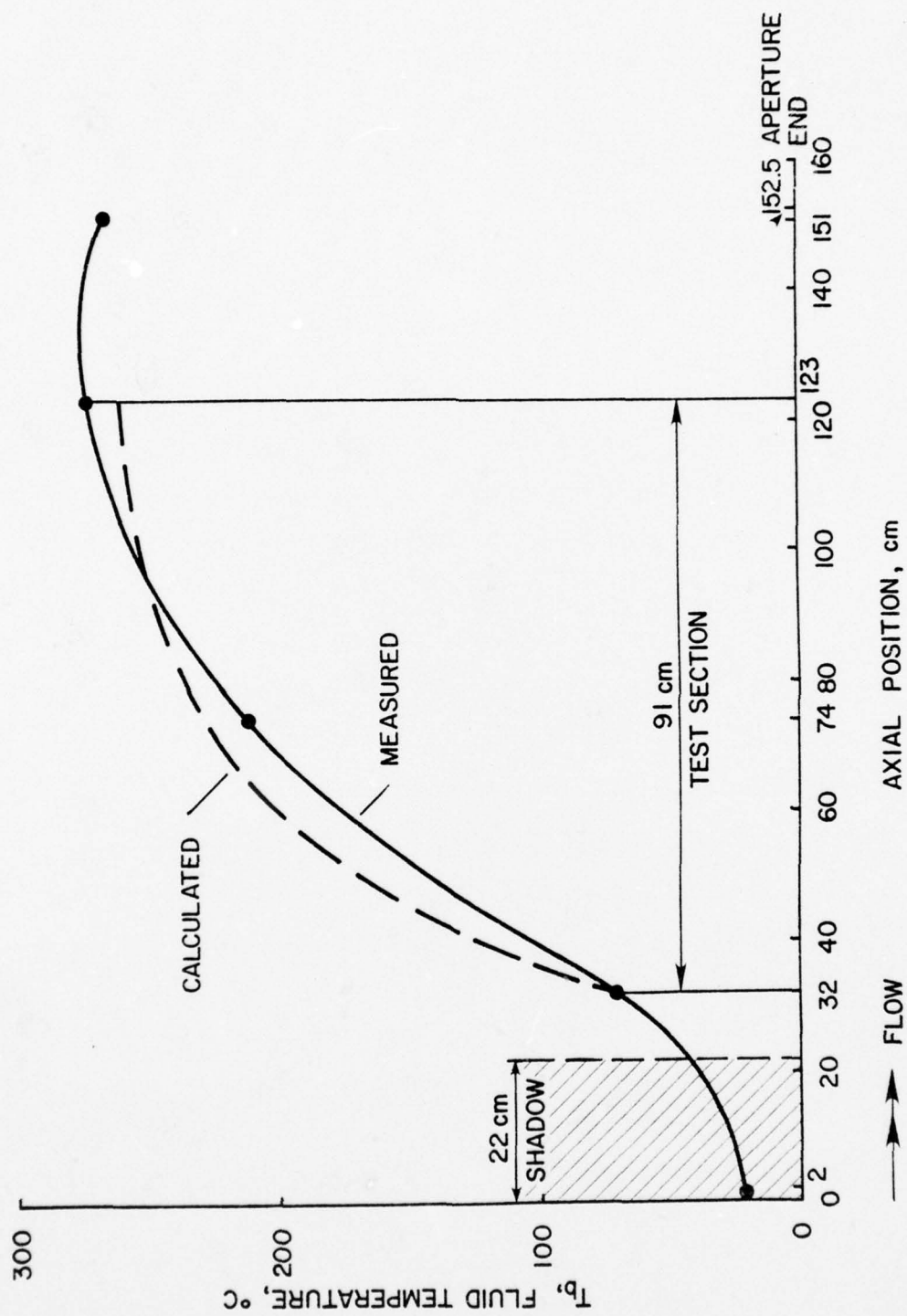
Figure 31. Temperature profiles on 23.III.77, 1:45 p.m. The direct solar flux was 872 W m^{-2}, the flow rate was 29.3 l min^{-1}, and the ambient temperature was 9°C. The highest temperature rise was measured on this occasion: 286°C over the 149 cm instrumented length. Also see Figure 22.
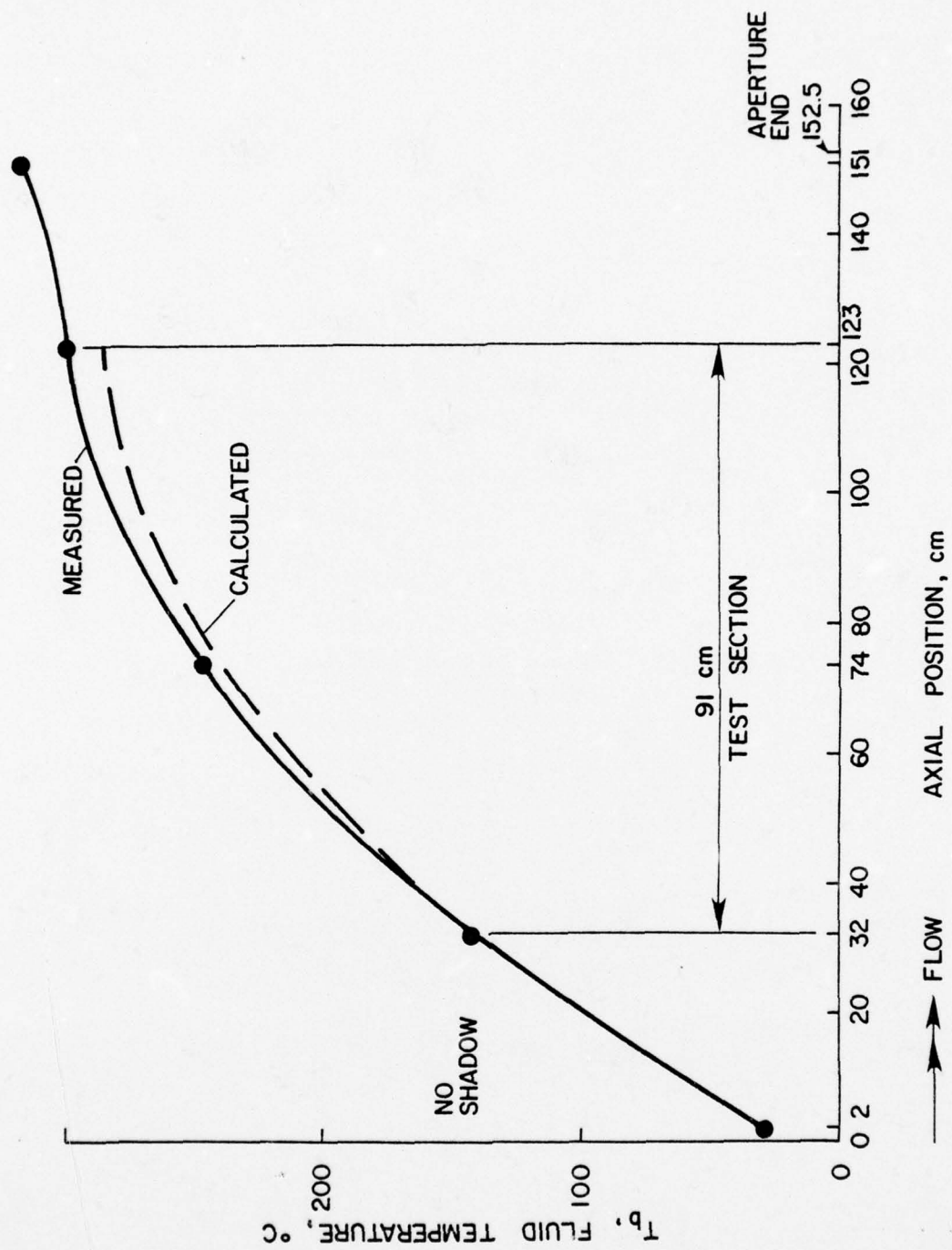
Figure 32. Temperature profiles on 17.III.77, 1:00 p.m. The direct solar flux was 852 W m^{-2}, the flow rate was 38.7 l min^{-1}, and the ambient temperature was 11°C. Some perturbation is observed near the receiver exit. Also see Figure 25.
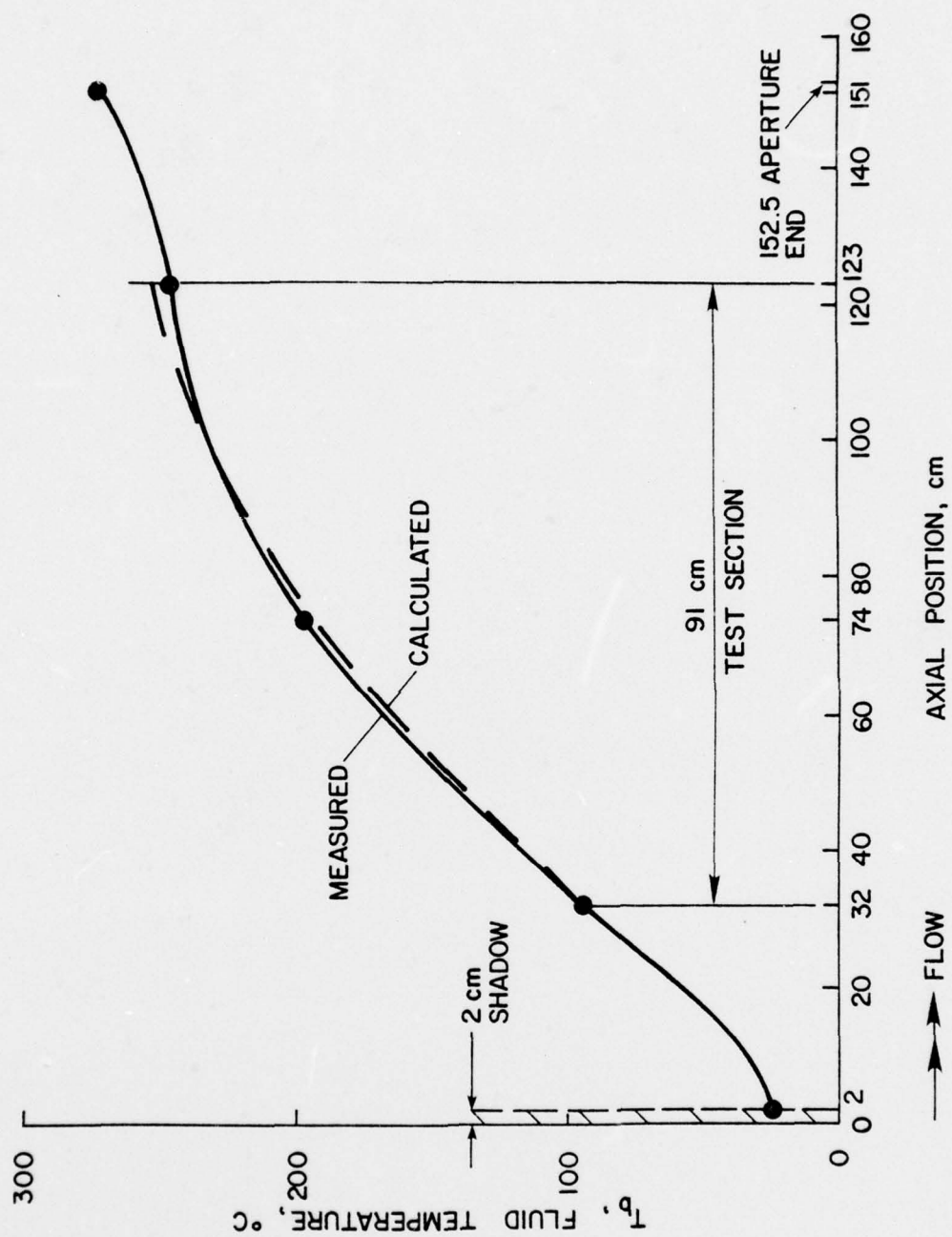
Figure 33. Temperature profiles on 9.III.77, 1:15 p.m. The direct solar flux was 864 W m^{-2}, the flow rate was 62.6 l min^{-1}, and the ambient temperature was 20°C. Strongly perturbed flow is observed in the downstream half of the receiver.
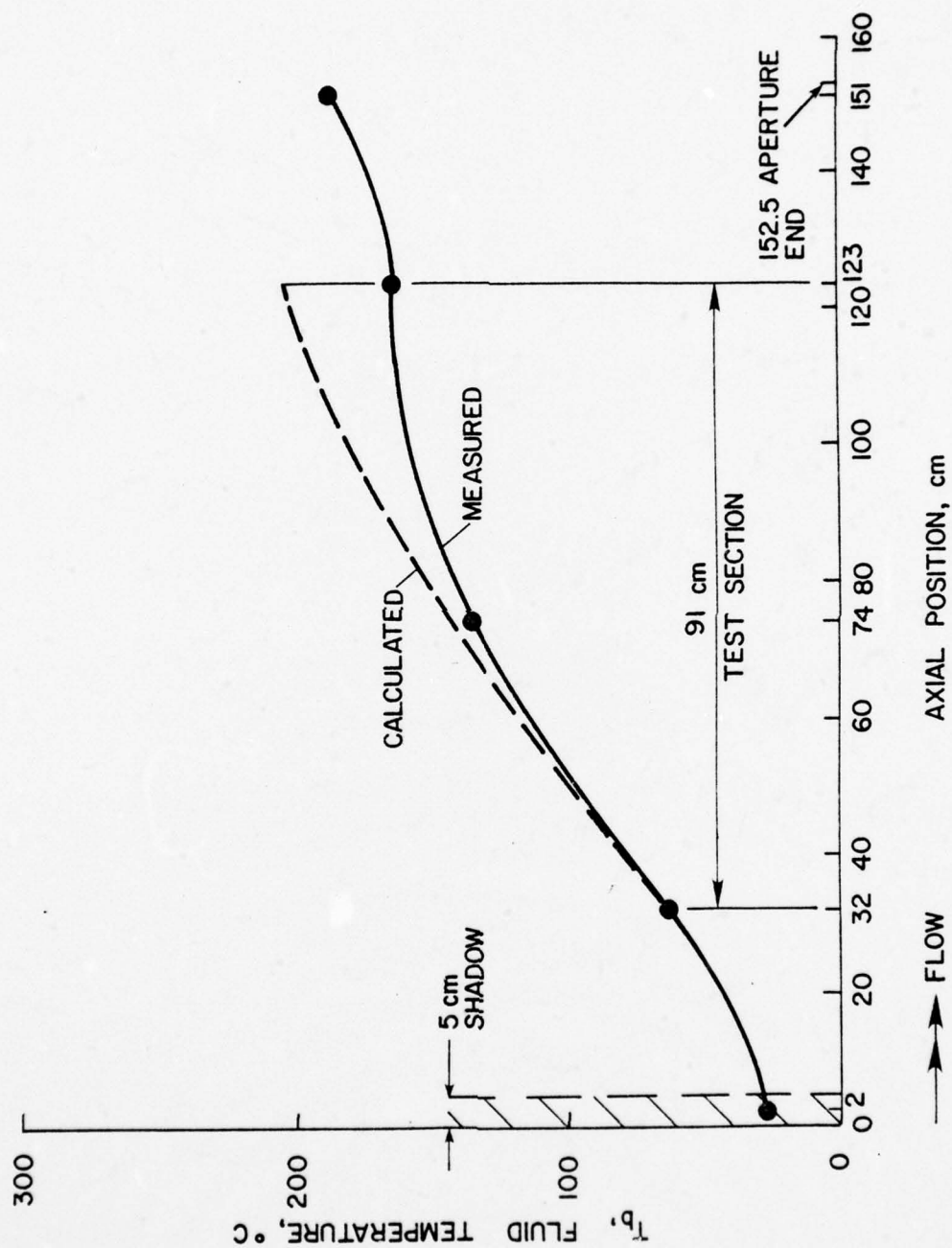
(compare FX1 with FX2 in Appendix II) and possibly some error in an assumed 5% loss because of misalingment between the reflected flux and the receiver aperture. All the results are summarized and compared in Table 9.

A number of calculations were also repeated, when there was no receiver inlet shadowing, starting right at the first thermocouple position 2 cm along the aperture. In general, a larger error is present in these calculated results since the inlet end effect becomes more severe and some of the assumptions become less tenable.

Furthermore, the use of the heating tape was found to provide little new information on the performance of the collector. At low flow rates, the exit temperature of the gas already approaches its asymptotic limit (see, for example, Figures 30 and 31); preheating the incoming gas thus serves only to move the onset of near-asymptotic conditions closer to the receiver inlet. The agreement between calculated and experimental temperatures is also somewhat poorer, as asymptotic conditions are approached (Table 9 and Figure 30). Sufficient variability in inlet temperatures was provided by the changes in flow rate, ambient temperature, solar flux, and aperture shadowing; preheating was therefore a redundant feature for this collector.

2. Selective Absorber

The standard program was modified to account for the different dimensions and properties of the selective copper absorber. Agreement

Table 9. Comparison of measured and calculated temperatures.

Date	Time, p.m.	Perp. direct solar flux, $W\ m^{-2}$	Flow rate, $1\ min^{-1}$	ΔT, °C (i.e., T17 – T14) Measured	Calculated
15.X.76	1:30	754	44.7	135	147
	2:45	717	89.5	55	94
23.X.76	1:30[a]	787	32.8	172	184
	2:30	750	62.3	84	131
14.XI.76	1.00	788	98.1	56	105
19.XI.76	12:30	647	11.9	201	189[b]
	1:50	566	26.6	158	158
14.XII.76	12:45	766	40.7	158	187
11.II.77	1:15	772	95.2	63	103
2.III.77	1:30	872	65.2	110	148
9.III.	1:15[c]	864	62.6	98	141
11.III.	1:00	776	52.1	111	134
17.III.	1:00[d]	852	38.7	151	159
19.III.	1:30	872	32.3	155	161
23.III.	1:45[e]	872	29.3	155	142
29.III.	1:15	860	20.9	139	121
30.III.	12:25	836	40.6	128	141
1.IV.	12:45	867	45.1	134	151
12.IV.	1:45	721	31.9	48	34
15.IV.	2:15	876	40.5	127	147

Table 9. Continued.

Date	Time, p.m.	Perp. direct solar flux, W m^{-2}	Flow rate, 1 min^{-1}	ΔT, °C (i.e., T17 - 14)	
				Measured	Calculated
17.IV.77	1:45	Very high preheat temperature; program stalls.			
8.V.	1:35[a]	782	33.0	96	99
14.V.	1:45	804	42.6	93	105
	2:45	793	42.2	51	56
26.V.[f]	1:30	721	20.7	132	98
	2:30	764	25.8	124	110
	3:30[a]	780	31.6	111	117
3.VI.	1:30	795	36.8	120	130
	2:30	813	40.5	117	138
	3:30	822	44.0	112	143
4.VI.	1:30	758	26.0	119	108
	2:30	775	31.5	116	121
	3:30	773	35.9	111	128

[a]See Figure 34

[b]Calculated with a 0.1 cm control volume and 0.001 °C axial loss convergence. See Figure 30

[c]See Figure 33

[d]See Figure 32

[e]See Figure 31

[f]Selective absorber now, and hereafter

between the experimental and calculated temperatures is not quite as good as for the graphite absorber. The buckling and rippling of the selective absorber is the probable cause of the larger discrepancy, as this undoubtedly disturbed the flow.

Comparison of an experiment, where the measured and theoretical temperatures are in close agreement, with the graphite absorber results for similar conditions (a composite of two graphite results was necessary, to span the temperature range) is shown in Figure 34. It is apparent that, within the limits of experimental and computational error, no gain results from the selective surface. This speaks well for the already high efficiency (i.e., low apparent emittance) of the cavity receiver design analyzed here. The higher end loss from the graphite is evident (Figure 34); its emittance is of course much higher, and it conducts more heat because of its thickness.

E. Conclusions

One phase in the development sequence of a particular solar thermal collector design has been described. The difficulties in a realistic modeling effort are readily apparent, yet do not compromise the validity of the results obtained. The experience gained with this model can prove useful for the examination of a larger model, or even the full-scale device. Sufficiently turbulent flow probably cannot be attained in any experimental model short of an extremely
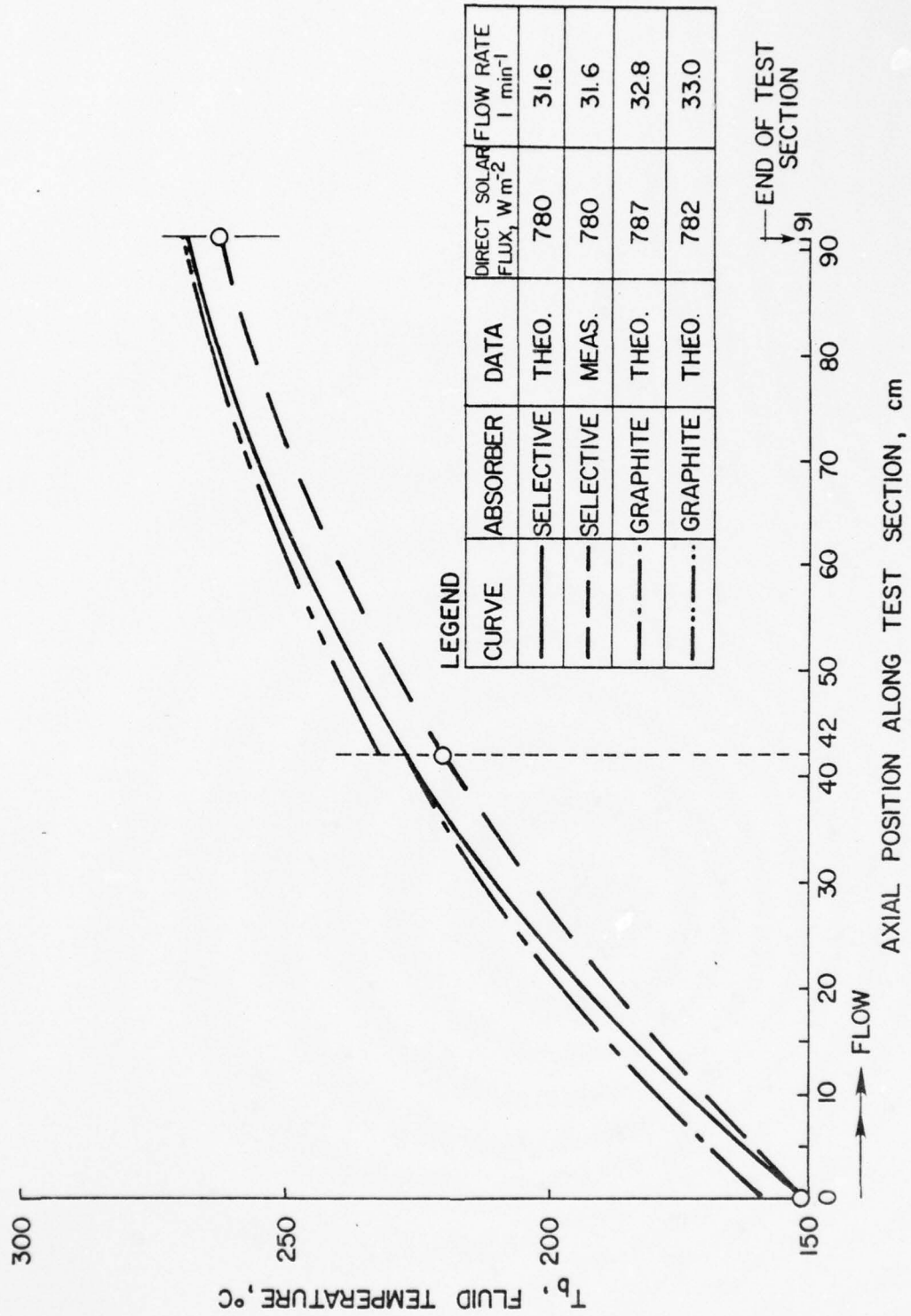
Figure 34. Absorber comparison.

large one, so that some buoyancy and developing flow effects even in a turbulent flow regime would still be present. However, their influence could be much reduced with a substantially larger collector and higher flow rates. A closer agreement between calculated and measured temperature profiles would thus occur in a larger model.

In conclusion, the basic concept studied here is sound, and reasonably efficient utilization (see $\overline{\overline{SUF}}$, or ASUF, in Appendix II) of solar energy at high fluid temperatures has been observed. This utilization is of course much lower than that estimated for the full-scale design (see Chapter V), because of end effects and greater radial heat losses. Again, a larger model should evince higher thermal efficiencies, approaching those of the full-scale. An indication of the potential power production for the particular device described here is illustrated by an example: at the 32.3 1 min^{-1} flow rate (Appendix II), energy is stored in the gas as it flows through the 91-cm long test section at a rate equal to 385 W. This power is much too low to drive any commercially available gas turbine.

CHAPTER V

MATHEMATICAL MODEL OF THE FULL-SCALE DESIGN

A. Approach

The good agreement between experimental and calculated temperature profiles in the scale model permits the formulation of a second computer model, of the proposed full-scale device (32), with confidence. This mathematical model of the full-scale collector is much less involved than the computer model of the experimental device.

The length (700 m) and relatively flat axial temperature profile of the full-scale collector allow both end effects and axial conduction to be neglected. The highly turbulent flow of the helium (Re = ca. 9×10^4) in the receiver reduces free convection effects to negligible values. Petukhov et al. (162) have shown that at this Reynolds number, and at the anticipated maximum Grashof number in the receiver, free-convection effects will cause a deviation in the forced convection Nusselt number of less than 1%. The same authors also show that flow development is essentially complete in ca. 10 to 20 diameters, so both these factors will be ignored here.

The temperature gradient between the heat transfer surfaces (glass + graphite) and the gas (He in the full-scale) can be calculated from the relation given by Kays (163):

$$Nu = 0.022 \ Pr^{0.6} \ Re^{0.8} \ .$$

A constant axial heat input is assumed in the above; however, if a constant axial wall temperature is taken instead as the more accurate representation, the only change in the relation occurs in the coefficient, from 0.022 to 0.021. At any rate, the calculated maximum temperature difference is only ca. 8°C, a trivial quantity. Thus the receiver, exclusive of the insulation, can be taken as isothermal radially. The computation therefore becomes a straightforward one-dimensional numerical integration of the energy balance on a small control volume, and yields the axial temperature profile of the flowing gas.

The main features of the computation are as follows:

(1) A control volume (element) length of 10 m.

(2) Consideration of radial losses only (i.e., essentially 1-D, although of course the radiant loss is mainly 2-D), which include conduction through the insulation and radiation by the aperture, both by the aperture sides and the glass window.

(3) Use of a variable view factor from the aperture, to account for examination of different pipe diameters and insulation thicknesses. The view factor is computed by the crossed-string method, as described in Chapter IV.

The standard configuration of the full-scale device has the following dimensions (from (32)) and properties (which are identical, except for the aperture emittance, with the material properties of the scale model): a receiver pipe of 30 cm inside diameter, glass pipe and graphite absorber thicknesses equal to 0.05 of this diameter, 10 cm thick Fiberfrax insulation with temperature-dependent thermal conductivity, a 6 cm wide aperture with an emittance (both glass and aperture sides) of 0.75, a mirror array width of 4 m and reflectance = 0.8, and a convective cover transmittance of 0.85. The more important perameters are individually varied in a computer program written in FORTRAN IV (see Appendix III). The helium inlet temperature is always taken as 349°C, and the mass flow rate is a constant 88 kg s^{-1} at ca. 7 atm pressure (from (32)). A conservative direct perpendicular solar flux of 800 W m^{-2}, and a 25°C ambient temperature (this is also the external insulation temperature) are assumed throughout.

B. Results of Computation

At a given (concentrated) solar flux level, the only signif-icant method for improving collector thermal efficiency involves

reduction of thermal losses. This can be achieved in any number of ways; the most influential parameters for the radiation-cavity collector design are the following:

(1) Increasing/decreasing the standard 6 cm aperture width results in approximately a 10°C/(cm of width changed) gas outlet temperature decrease/increase, respectively (see Figure 35). The aperture ought to be kept as small as possible, but it must be recalled that a tradeoff condition exists here. The pointing error, mirror surface error, tracking error, economical mirror width, and similar constraints limit the width of mirror strips to a value which is probably considerably greater than the optimum suggested by radiative loss considerations.

(2) Since at high temperatures radiative losses predominate, the greatest efficiency increase is accomplished by significantly lowering the I.R. emittance of the aperture (see Figure 36). This merits further study, as will be discussed in Chapter VI.

(3) Considerable gains can be made from an increase in mirror reflectance from 0.8 to 0.9 (see Figure 37; the SUF, as defined, is irrelevant and is not shown). Front-surface mirrors with a reflectance in this higher range are available, but degradation of the reflective surface could pose difficulties.

(4) Some improvement also results from increasing the convective cover transmittance from 0.85 to 0.95 (see Figure 38). In fact,

Figure 35. Effect of aperture width (theoretical).

Figure 36. Effect of aperture emittance (theoretical)
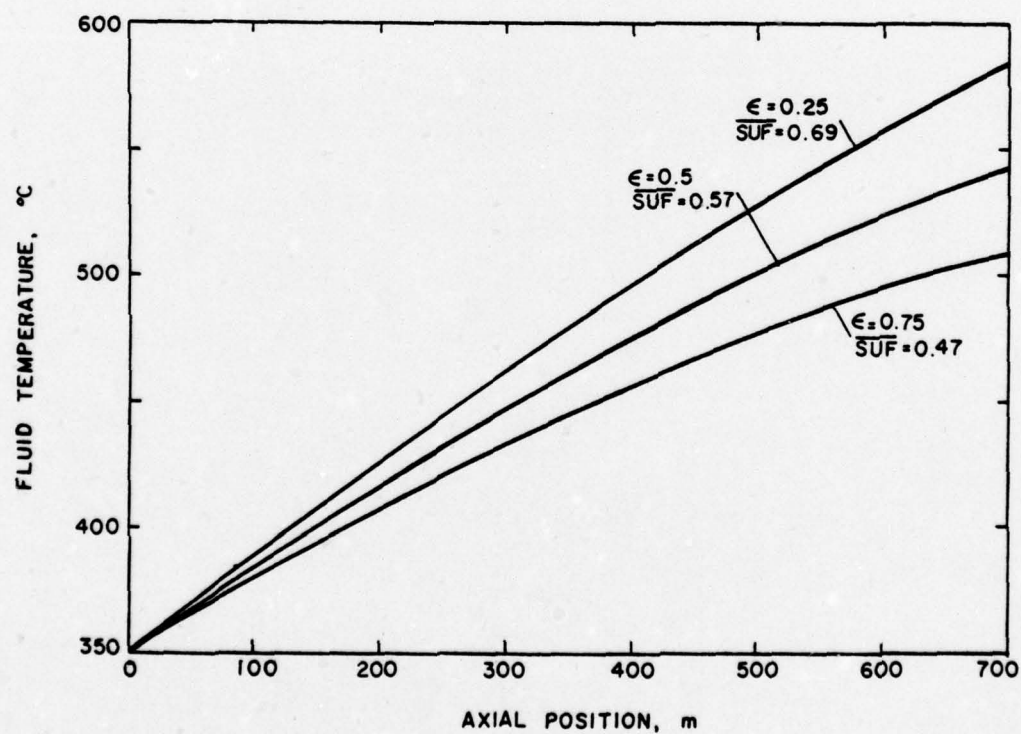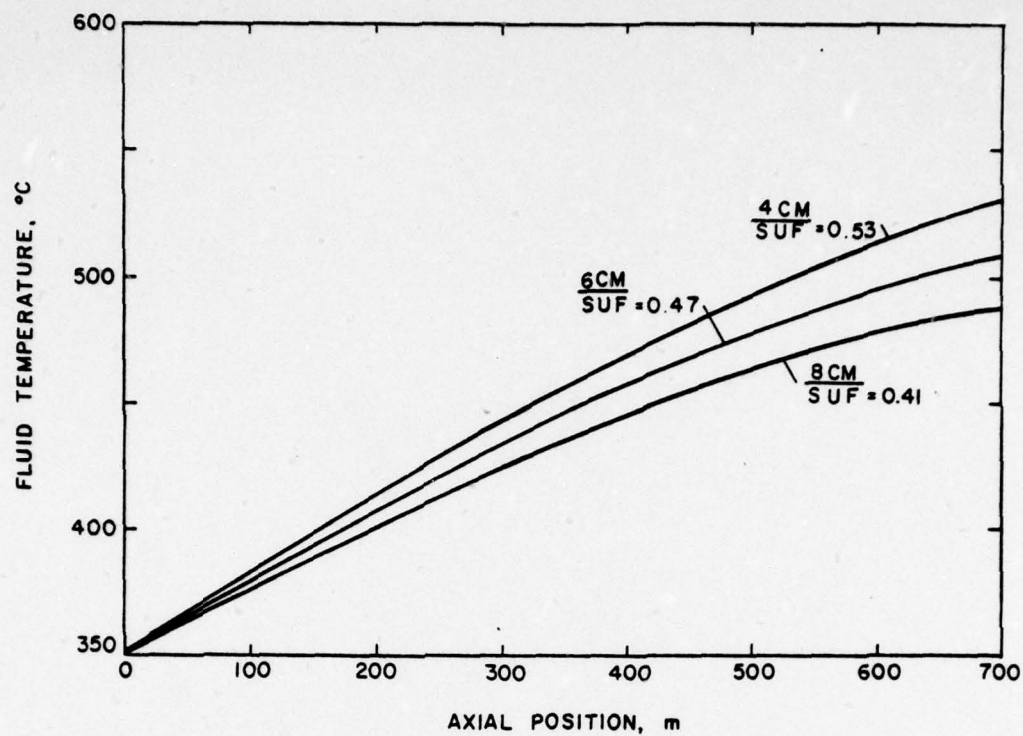
Figure 37. Effect of mirror reflectance (theoretical).

Figure 38. Effect of cover transmittance (theoretical).
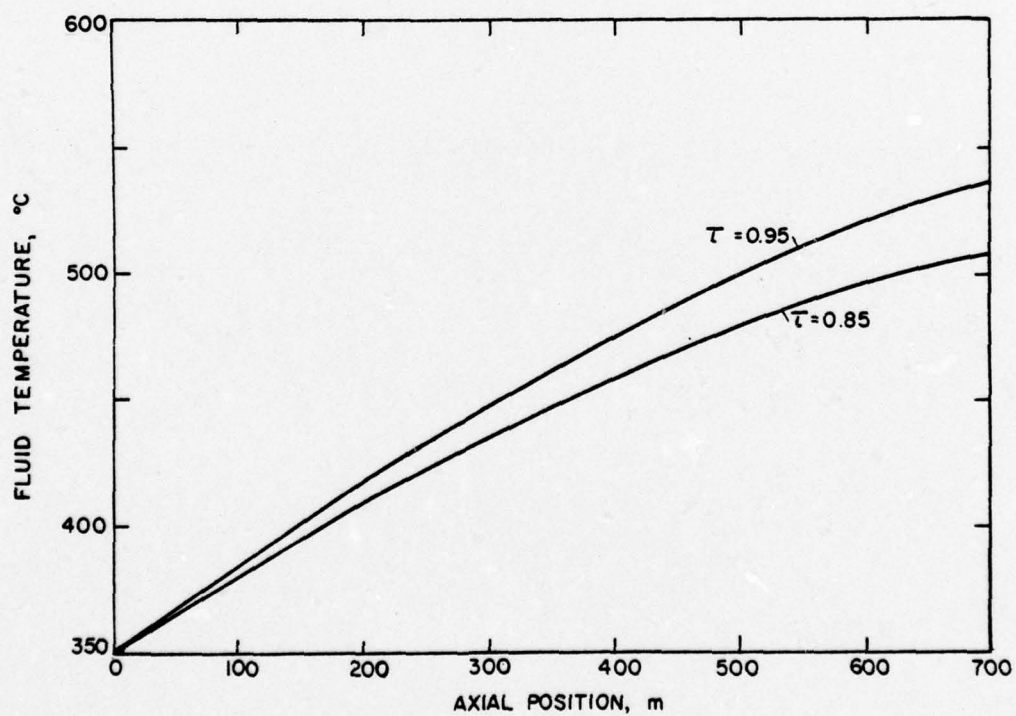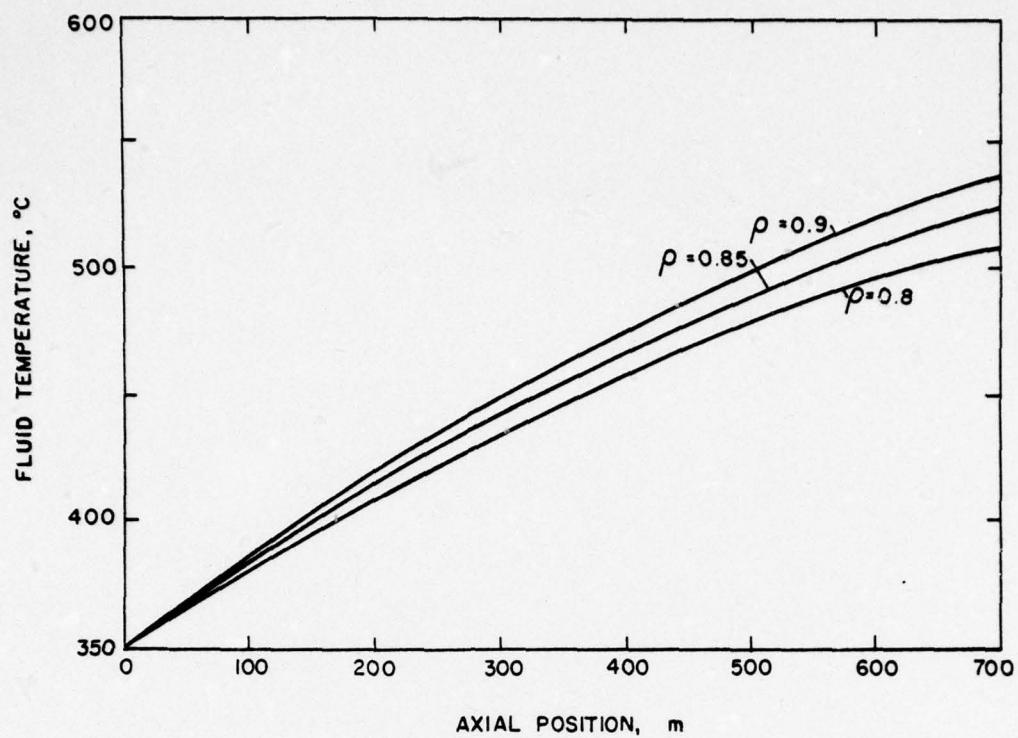
it may prove advantageous to dispense with this cover altogether.
The tradeoff (not studied) with augmented free convection loss from
the aperture in the full-scale device would probably result in a
net gain, given the proportionately small size of the aperture.
Again, the SUF is irrelevant.

(5) For a 30 cm I.D. receiver pipe, 10 cm of insulation is
about optimal (see Figure 39). The reason behind the seeming insen-
sitivity of the device to insulation thickness lies in the radiant
loss from the aperture. This is negatively affected by the wider
aperture sides (from thicker insulation), although the increased
radiation is somewhat offset by a poorer view factor to the ambient
environment. Thus, any gain from added insulation (beyond 10 cm)
is masked and overwhelmed by associated radiative losses. The same
mechanism operates in apparently making a 5 cm thick insulation
almost as effective as the double (10 cm) thickness.

(6) Reducing the pipe diameter to 20 cm, for the same gas
mass flow rate, has a negligible effect on efficiency (see Figure 40).
Use of the smaller pipe would entail a larger pressure drop (fric-
tional loss) which was not included in this calculation. An
alternate conclusion is that an increase in mirror width (i.e.,
flux concentration ratio) is probably not an effective means for
increasing the thermal efficiency.

Figure 39.   Effect of insulation thickness (theoretical).

Figure 40.   Effect of receiver diameter (theoretical).
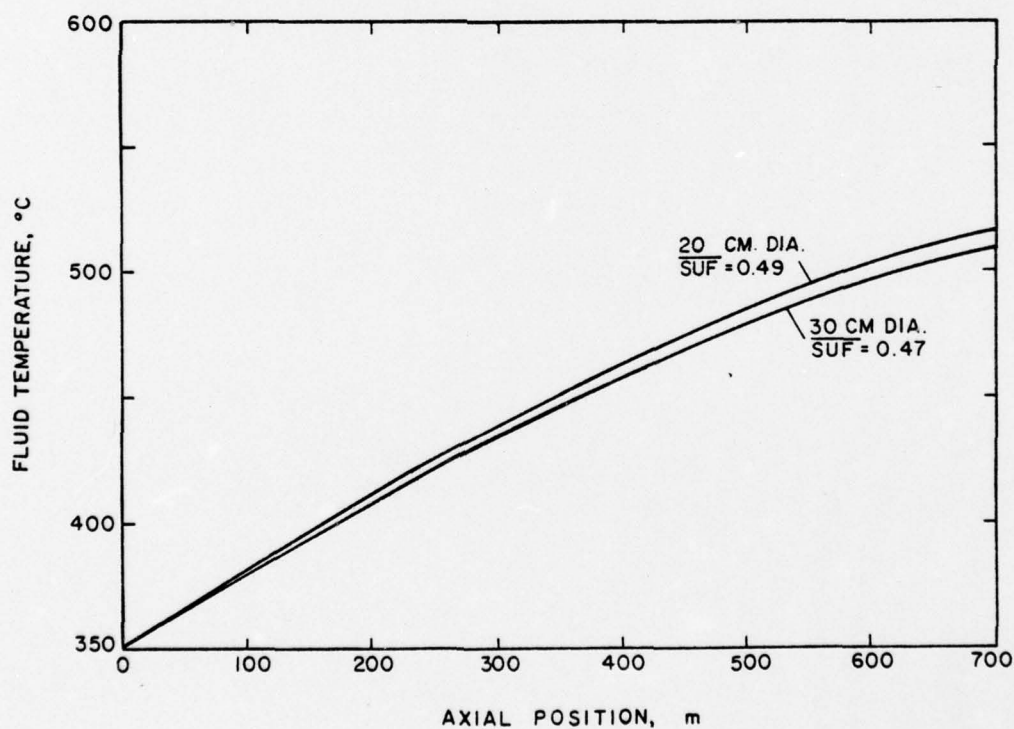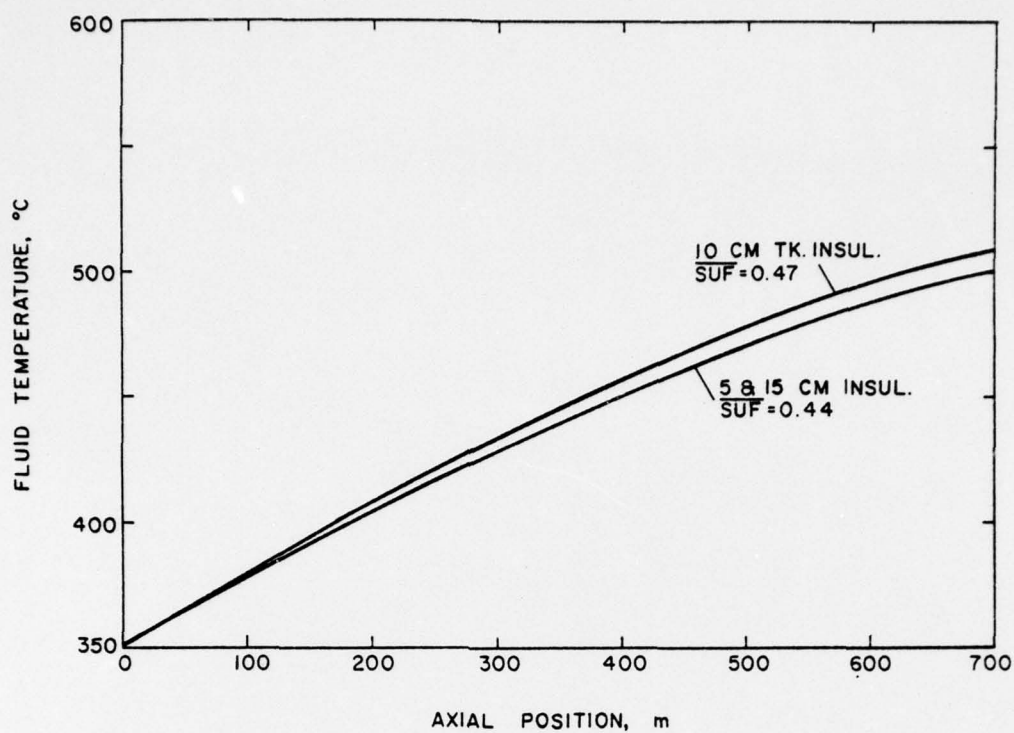
C.   Conclusions from Theoretical Analysis

      The good agreement between experimental and theoretical results has allowed optimization studies of the full-scale device to be performed, via a second computer model. These indicate that average (over the length of the receiver) heat utilization efficiencies (i.e., heat into fluid/heat into receiver, also termed here the Solar Utilization Factor, of SUF) on the order of 50% and a receiver gas (He) exit temperature of ca. 510°C are realistic design goals. This analysis lends credence to the concept as first proposed (32), and confirms that the originally projected efficiencies were not overly optimistic.

CHAPTER VI

SUMMARY AND SUGGESTIONS FOR FURTHER STUDY

A high-temperature solar collector design has been described herein, and the results of experimental and theoretical studies have been discussed. In summary, these studies have shown that:

(1) High fluid exit temperatures, at a reasonable thermal efficiency, are achievable with this design.

(2) Readily available materials can be employed in a high-temperature collector with little degradation. Very similar materials could be used in a practical full-scale device.

(3) The Archimedes mirror-concentrator is easily constructed and focused, requiring little maintenance thereafter.

(4) A fixed glass receiver pipe surrounded by rotating insulation and aperture is a simple and effective means of radiation-cavity construction.

(5) The use of circular tracks, chain drive, and a stepping motor is a method which could be readily adapted to a full-scale tracking system. For example, earthen/reinforced concrete tracks could be made at low cost and to acceptable tolerances.

(6) Further study of a selective absorber is not warranted since the cavity receiver design is already very efficient. The influence of absorber emittance would be even smaller in a full-scale device, since its aperture is proportionately (compared to the experimental model) smaller.

(7) In theory, the efficiency admits of significant improvement, by the various means discussed in Chapter V.

The great differences in scale and thermodynamic behavior that exist between the model and the practical size suggest that further study is desirable. A 1/3 scale collector (i.e., double the cross-sectional scale of the present model) with a 3-cm aperture and fully turbulent (Re = 10^4) flow would have a gas outlet temperature ca. 350°C, for a 30°C inlet temperature. The effective length is taken as 10 m, and a direct solar flux of 800 W m^{-2} is assumed in the calculation. A stagnation temperature in excess of 420°C should result. A Pyrex pipe could still be used at such temperatures; models larger than this would require more costly receiver pipe materials (e.g., aluminosilicate glass).

Another aspect that merits additional study is the deposition of an I.R. heat shield on the Pyrex aperture. Tin oxide films exhibit excellent selectivity, with a high transmittance in the solar wavelength range, and a low emittance at longer (thermal) wavelengths (164,165). The durability and mechanical properties

of the films are outstanding (166). While various methods exist (164) for applying tin oxide coatings to surfaces, a straightforward technique such as proposed by Lytle and Junge (167), with boro-silicate glass as the substrate material, would be worth investigating.

A small pilot plant, of a size which could employ a commercially available gas turbine, would be a necessary element in the progression to full-scale construction. At some step along this study sequence, attention should be given to optimum receiver pipe length, fluid mass flow rate, and receiver arrangement (in the last, tilt or hori-zontal positioning tradeoffs need to be considered). Last, but by no means least, a detailed economic analysis of the proposed design needs to be made in order to ascertain its viability. As the costs of other power-production methods increase with time, a point could well be reached in the near future at which solar thermal power would become economically competitive.

REFERENCES

1. A. B. Meinel and M. P. Meinel, _Applied Solar Energy_, Addison-Wesley, Reading, MA (1976).

2. J. A. Duffie and W. A. Beckman, _Solar Energy Thermal Processes_, Wiley, New York (1974).

3. A. B. Meinel and M. P. Meinel, ASME Winter Annual Mtg., Paper No. 72-WA/Sol-7 (1972).

4. A. B. Meinel, Physics Today 25 (2), 44 (1972).

5. D. T. Nelson, D. L. Evans, R. K. Bansal, Solar Energy 17, 285 (1975).

6. D. O. Lee and W. P. Schimmel, Jr., Proc. 9th Intersociety Energy Conversion Engineering Conf., 347 (1974).

7. A. B. Meinel and M. P. Meinel, Solar Energy 18, 177 (1976).

8. M. W. Edenburn, Solar Energy 18, 437 (1976).

9. J. W. Ramsey, B. P. Gupta and G. R. Knowles, J. Heat Transfer 99, 163 (1977).

10. M. H. Cobble and P. R. Smith, ASME Winter Annual Mtg., Paper No. 75-WA/Sol-4 (1975).

11. P. Singh and L. S. Cheema, Solar Energy 18, 135 (1976).

12. J. R. Howell and R. B. Bannerot, Solar Energy 19, 149 (1977).

13. R. H. Turner, Proc. 11th Intersociety Energy Conversion Engineering Conf., 1239 (1976).

14. E. R. G. Eckert et al., "Research Applied to Solar-Thermal Power Systems," Report: NSF/RANN/SE/GI-34871/PR/73/2, University of Minnesota and Honeywell, Minneapolis, MN (1973).

15. C. R. Easton, R. W. Hallet, Jr., S. Gronich, and R. L. Gervais, Proc. 9th Intersociety Energy Conversion Engineering Conf. 271 (1974).

16. A. F. Hildebrandt and L. L. Vant-Hull, ASME Winter Annual Mtg., Paper No. 73-WA/Sol-7 (1973).

17. F. A. Blake and J. D. Walton, Solar Energy 17, 213 (1975).

18. F. A. Blake, T. R. Tracey, J. D. Walton, and S. Bomar, Solar Energy 18, 513 (1976).

19. L. L. Vant-Hull and A. F. Hildebrandt, Solar Energy 18, 31 (1976).

20. F. W. Lipps, Solar Energy 18, 555 (1976).

21. M. Riaz and T. Gurr, Solar Energy 19, 185 (1977).

22. A. Sobin, W. Wagner, and C. R. Easton, Solar Energy 18, 21 (1976).

23. T. H. Springer and W. B. Thomson, Proc. 11th Intersociety Energy Conversion Engineering Conf., 1232 (1976).

24. P. O. Jarvinen, Solar Energy 19, 139 (1977).

25. P. O. Jarvinen, Proc. 11th Intersociety Energy Conversion Engineering Conf., 1244 (1976).

26. C. R. Easton, J. E. Raetz, and L. L. Vant-Hull, Proc. 11th Intersociety Energy Conversion Engineering Conf., 1272 (1976).

27. L. Wen and Y. C. Wu, Proc. 11th Intersociety Energy Conversion Engineering Conf., 1209 (1976).

28. R. S. Caputo and V. C. Truscello, Proc. 11th Intersociety Energy Conversion Engineering Conf., 1216 (1976).

29. Anon., Industrial Research 19 (3), 42 (1977).

30. F. Kreith, Principles of Heat Transfer, 2nd ed., International Textbook Co., Scranton, PA (1967), p. 203.

31. H. B. Palmer, Proc. 8th Intersociety Energy Conversion Engineering Conf., 366 (1973).

32. H. B. Palmer and S. C. Kuo, Proc. 9th Intersociety Energy Conversion Engineering Conf., 264 (1974).

33. A. B. Meinel and M. P. Meinel, Applied Solar Energy, Addison-Wesley, Reading, MA (1976), p. 234.

34. Anon., Materials Handbook, 8th ed., Corning Glass Works, Corning, NY (1968).

35. T. A. Myles, private communication, The Carborundum Co., Niagara Falls, NY (December 7, 1976).

36. P. I. Cooper, Solar Energy 12, 333 (1969).

37. E. M. Sparrow and J. L. Gregg, in Recent Advances in Heat and Mass Transfer, J. P. Hartnett, ed., McGraw-Hill, NY (1961), pp. 353-371.

38. A. Brown, J. Heat Transfer 97, 133 (1975).

39. E. R. G. Eckert and R. M. Drake, Analysis of Heat and Mass Transfer, McGraw-Hill, NY (1972), p. 780.

40. F. Kreith, Principles of Heat Transfer, 2nd ed., International Textbook Co., Scranton, PA (1967), Chapter 7.

41. W. M. Kays, Convective Heat and Mass Transfer, McGraw-Hill, NY (1966), p. 60.

42. Anon., "Material Information" (bulletin), Corning Glass Works, Corning, NY (September, 1971), pp. 1-4.

43. Anon., "Fiberfrax Ceramic Fiber Forms for 2600 F," (brochure), The Carborundum Company, Niagara Falls, NY (June, 1975).

44. J. R. Singham, Int. J. Heat Mass Transfer 5, 67 (1962).

45. F. Rusinko, Jr., private communication, Airco-Speer Carbon-Graphite, St. Marys, PA (August 4, 1976).

46. E. A. Christie, Int. Solar Energy Soc. Conf., Preprint of Paper No. 7/81, Melbourne, Australia (1970).

47. M. D. Kudryashova, Appl. Solar Energy 5 (4), 82 (1969).

48. R. C. Weast, ed., Handbook of Chemistry and Physics, 56th ed., CRC Press, Cleveland (1975), p. D-171.

49. H. H. Plumb, ed., Temperature - Its Measurement and Control in Science and Industry, Instr. Soc. of America, Pittsburgh (1972), Vol. 4, pp. 1534, 1781, 2017.

50. J. F. Swindells, ed., "Precision Measurement and Calibration - Temperature," National Bureau of Stds. Special Publication 300 (1968), Vol. 2, pp. 220-400.

51. M. P. Thekaekara, Inst. of Envir. Sci., Proc. 20th Annual Mtg. (Supplement), p. 21 (1974).

52. M. P. Thekaekara, "Solar Irradiance at Ground Level," deck no. 17, on punched cards, available from National Space Sci. Data Ctr., NASA/GSFC, Code 601, Greenbelt, MD.

53. Y. S. Touloukian, ed., Thermophysical Properties of High Temperature Solid Materials, MacMillan, NY (1967), Vols. 1 and 4.

54. T. J. Love, Radiative Heat Transfer, C. E. Merrill, Columbus, OH (1968), p. 208.

55. Anon., ASHRAE Handbook of Fundamentals, NY (1972), p. 385.

56. S. L. Valley, ed., Handbook of Geophysics and Space Environments, Air Force Cambridge Res. Labs., McGraw-Hill, NY (1965), Chapter 16.

57. P. Moon, J. Franklin Inst., 230 (5), 583 (1940).

58. K. L. Coulson, Solar and Terrestrial Radiation, Academic Press, NY (1975), pp. 47-49.

59. N. Robinson, ed., Solar Radiation, Elsevier, Amsterdam (1966), p. 105.

60. K. Ya. Kondratyev, Radiation in the Atmosphere, Academic Press, NY (1969), pp. 199, 243, 380.

61. N. Neuroth, Glastech. Ber. 41, 243 (1968).

62. E. P. Markin and N. N. Sobolev, Opt. and Spectroscopy 9, 309 (1960).

63. Anon., "Properties of Glasses and Glass-Ceramics," (booklet), Corning Glass Works, Corning, NY (October, 1972).

64. M. Pirani, J. Sci. Instrum. 16, 372 (1939).

65. M. Born and E. Wolf, Principles of Optics, 5th ed., Pergamon, NY (1975), p. 42.

66. E. A. Porai-Koshits, S. P. Zhdanov, and N. S. Andreev, Proc. 3rd All-Union Conf. on Glassy State, Leningrad (1959), pp. 468-471.

67. W. Sieber, Z. tech. Physik 22, 130 (1941).

68. W. D. Wood, H. W. Deem, and C. F. Lucks, in Thermal Radiative Properties, Vol. 3 of High-Temperature Materials, Plenum Press, NY (1964), pp. 432-440.

69. B. A. Khrustalev and A. M. Rakov, Heat Transfer-Soviet Res. 1 (4), 187 (1969).

70. H. Goochee, private communication (telephone), Airco-Speer Carbon-Graphite, St. Marys, PA (December 1, 1976).

71. W. B. Meinel, private communication, W. B. Meinel Laboratory, Tucson, AZ (February, 1977).

72. H. C. Hottel and T. A. Unger, Solar Energy 3 (3), 10 (1959).

73. C. L. Tien, C. K. Chan, and G. R. Cunnington, J. Heat Transfer 94, 41 (1972).

74. A. Standen, ed., Kirk-Othmer Enclycopedia of Chemical Technology 2nd ed., J. Wiley, NY (1964), Vol. 4, pp. 217, 236.

75. J. Reuther, private communication, The Pennsylvania State University (September, 1975).

76. E. S. L. Beale, in Technical Data on Fuel, H. M. Spiers, ed., The British National Committee, London (1962), pp. 124-134.

77. R. F. Stearns, R. R. Johnson, R. M. Jackson, and C. A. Larson, Flow Measurement with Orifice Meters, D. Van Nostrand, NY (1951).

78. F. W. Schmidt and B. Zeldin, Appl. Sci. Res. 23, 73 (1970).

79. W. M. Kays, Convective Heat and Mass Transfer, McGraw-Hill, NY (1966), p. 121.

80. J. Norman, private communication, Meteorology Department, The Pennsylvania State University (March 23, 1977).

81. R. C. Temps and K. L. Coulson, Solar Energy 19, 179 (1977).

82. B. Y. H. Liu and R. C. Jordan, Solar Energy 4 (3), 1 (1960).

83. D. W. Ruth and R. E. Chant, Solar Energy 18, 153 (1976).

84. J. F. Orgill and K. G. T. Hollands, Solar Energy 19, 357 (1977).

85. S. E. Tuller, Solar Energy 18, 259 (1976).

86. I. Catton, P. S. Ayyaswamy, and R. M. Clever, Int. J. Heat Mass Transfer 17, 173 (1974).

87. J. N. Arnold, I. Catton, and D. K. Edwards, J. Heat Transfer
    98, 67 (1976).

88. H. Ozoe, H. Sayama, and S. W. Churchill, Int. J. Heat Mass
    Transfer 18, 1425 (1975).

89. E. R. G. Eckert and R. M. Drake, Jr., Analysis of Heat and
    Mass Transfer, McGraw-Hill, NY (1972), pp. 536-541.

90. M. N. Özisik, Radiative Transfer, J. Wiley, NY (1973),
    Chapter 3.

91. H. C. Hottel and A. F. Sarofim, Radiative Transfer, McGraw-
    Hill, NY (1967), pp. 31-33.

92. K. C. Cheng, S. W. Hong, and G. J. Hwang, Int. J. Heat Mass
    Transfer 15, 1819 (1972).

93. C. M. Usiskin and R. Siegel, J. Heat Transfer 82, 369 (1960).

94. R. Siegel and M. Perlmutter, Int. J. Heat Mass Transfer 5,
    639 (1962).

95. M. Perlmutter and R. Siegel, J. Heat Transfer 84, 301 (1962).

96. R. S. Thorsen, Int. J. Heat Mass Transfer 12, 1182 (1969).

97. R. Thorsen and D. Kanchanagom, Proc. 4th Int. Heat Transfer
    Conf., 3, Paper R2.8, Paris-Versailles (1970).

98. E. R. G. Eckert, T. F. Irvine, Jr., and J. T. Yen, Trans.
    ASME 80 (1), 1433 (1958).

99. E. M. Sparrow and A. Haji-Sheikh, J. Heat Transfer 87, 426
    (1965).

100. E. M. Sparrow and A. Haji-Sheikh, J. Heat Transfer 88, 351
     (1966).

101. E. R. G. Eckert and T. F. Irvine, Jr., Trans. ASME 78 (1), 709
     (1956).

102. W. C. Reynolds, J. Heat Transfer 82, 108 (1960).

103. W. M. Kays, Convective Heat and Mass Transfer, McGraw-Hill,
     NY (1966).

104. Ibid., pp. 139-142.

105. Ibid., p. 63.

106. J. G. Knudsen and D. L. Katz, <u>Fluid Dynamics and Heat Transfer</u>, McGraw-Hill, NY (1958), pp. 368-374.

107. J. R. Sellars, M. Tribus, and J. S. Klein, Trans. ASME <u>78</u> (1), 441 (1956).

108. W. M. Kays, Trans. ASME <u>77</u> (1), 1265 (1955).

109. S. W. Churchill and H. Ozoe, J. Heat Transfer <u>95</u>, 78 (1973).

110. H. L. Langhaar, J. Appl. Mech. <u>64</u>, A-55 (1942).

111. E. M. Sparrow and S. H. Lin, Phys. Fluids <u>7</u>, 338 (1964).

112. R. W. Hornbeck, Appl. Sci. Res. <u>13</u> (A), 224 (1964).

113. E. B. Christiansen and H. E. Lemmon, AIChE J. <u>11</u>, 995 (1965).

114. F. W. Schmidt and B. Zeldin, AIChE J. <u>15</u>, 612 (1969).

115. D. L. Ulrichson and R. A. Schmitz, Int. J. Heat Mass Transfer <u>8</u>, 253 (1965).

116. R. Manohar, Int. J. Heat Mass Transfer <u>12</u>, 15 (1969).

117. S. W. Hong and A. E. Bergles, Int. J. Heat Mass Transfer <u>19</u>, 123 (1976).

118. M. Iqbal and J. W. Stachiewicz, J. Heat Transfer <u>88</u>, 109 (1966).

119. G. N. Faris and R. Viskanta, Int. J. Heat Mass Transfer <u>12</u>, 1295 (1969).

120. P. H. Newell, Jr. and A. E. Bergles, J. Heat Transfer <u>92</u>, 83 (1970).

121. M. Iqbal and J. W. Stachiewicz, Int. J. Heat Mass Transfer <u>10</u>, 1625 (1967).

122. T. M. Hallman, Trans. ASME <u>78</u> (1), 1831 (1956).

123. L. N. Tao, Appl. Sci. Res. <u>9</u> (A), 357 (1960).

124. M. Iqbal, B. D. Aggarwala, and A. G. Fowler, Int. J. Heat Mass Transfer <u>12</u>, 1123 (1969).

125. M. Iqbal, A. K. Khatry, and B. D. Aggarwala, Appl. Sci. Res. <u>26</u>, 183 (1972).

126. M. Iqbal, B. D. Aggarwala, and A. K. Khatry, J. Heat Transfer <u>94</u>, 52 (1972).

127. M. Iqbal, S. A. Ansari, and B. D. Aggarwala, J. Heat Transfer 92, 237 (1970).

128. B. D. Aggarwala and M. Iqbal, Int. J. Heat Mass Transfer 12, 737 (1969).

129. A. L. Nayak and P. Cheng, Int. H. Heat Mass Transfer 18, 227 (1975).

130. A. K. Muntjewerf, H. A. Leniger, and W. J. Beek, Appl. Sci. Res. 23, 134 (1970).

131. P. M. Worsøe-Schmidt and G. Leppert, Int. J. Heat Mass Transfer 8, 1281 (1965).

132. W. T. Lawrence and J. C. Chato, J. Heat Transfer 88, 214 (1966).

133. R. C. Biggs and J. W. Stachiewics, Proc. 4th Int. Heat Transfer Conf., 4, Paper NC3.1, Paris-Versailles (1970).

134. D. Maitra and K. S. Raju, J. Heat Transfer 97, 135 (1975).

135. A. J. Ede, Int. J. Heat Mass Transfer 4, 105 (1961).

136. B. R. Morton, Quart. J. Mech. Appl. Math. 12, 410 (1959).

137. Y. Mori, K. Futagami, S. Tokuda, and M. Nakamura, Int. J. Heat Mass Transfer 9, 453 (1966).

138. Y. Mori and K. Futagami, Int. J. Heat Mass Transfer 10, 1801 (1967).

139. K. C. Cheng and G. J. Hwang, J. Heat Transfer 91, 59 (1969).

140. S. W. Hong and A. E. Bergles, J. Heat Transfer 98, 459 (1976).

141. R. L. Shannon and C. A. Depew, J. Heat Transfer 90, 353 (1968).

142. R. L. Shannon and C. A. Depew, J. Heat Transfer 91, 251 (1969).

143. S. M. Morcos and A. E. Bergles, J. Heat Transfer 97, 212 (1975).

144. A. E. Bergles and R. R. Simonds, Int. J. Heat Mass Transfer 14, 1989 (1971).

145. S. W. Hong, S. M. Morcos and A. E. Bergles, Proc. 5th Int. Heat Transfer Conf., 3, Paper NC4.6, Tokyo (1974).

146. K. C. Cheng and J. W. Ou, Proc. 5th Int. Heat Transfer Conf., 3, Paper NC4.7, Tokyo (1974).

147. S. T. McComas and E. R. G. Eckert, J. Heat Transfer 88, 147 (1966).

148. N. A. Hussain and S. T. McComas, Proc. 4th Int. Heat Transfer Conf., 4, Paper NC3.4, Paris-Versailles (1970).

149. G. J. Hwang and K. C. Cheng, Proc. 4th Int. Heat Transfer Conf., 4, Paper NC3.5, Paris-Versailles (1970).

150. K. C. Cheng and S. W. Hong, Appl. Sci. Res. 27, 19 (1972).

151. J. A. Sabbagh, A. Aziz, A. S. El-Ariny, and G. Hamad, J. Heat Transfer 98, 322 (1976).

152. K. Futagami and F. Abe, Trans. Japan Soc. Mech. Engrs. 38, 1799 (1972), in Japanese.

153. J. W. Ou, K. C. Cheng, and R. C. Lin, Int. J. Heat Mass Transfer 19, 277 (1976).

154. W. M. Kays, Convective Heat and Mass Transfer, McGraw-Hill, NY (1966), p. 39.

155. A. H. Shapiro, The Dynamics and Thermodynamics of Compressible Fluid Flow, Ronald Press, NY (1953), Chapter 1, p. 48.

156. J. Hilsenrath et al., "Tables of Thermal Properties of Gases," National Bureau of Stds. Circ. 564 (1955).

157. K. Ražnjević, Handbook of Thermodynamic Tables and Charts, Hemisphere Pub. Corp., Washington (1975), p. 297.

158. W. J. Karplus, AIEE Trans. 77 (1), 210 (1958).

159. G. M. Dusinberre, Heat Transfer Calculations by Finite Differences, Int. Textbook Co., Scranton PA (1961).

160. P. D. Lax and R. D. Richtmyer, Comm. Pure Appl. Math. 9, 267 (1956).

161. R. D. Richtmyer and K. W. Morton, Difference Methods for Initial-Value Problems, 2nd ed., Interscience, NY (1967), pp. 40-45.

162. B. S. Petukhov, A. F. Polyakov, V. A. Kuleshov, and Yu. A. Sheckter, Proc. 5th Int. Heat Transfer Conf., 3, Paper NC4.8, Tokyo (1974).

163. W. M. Kays, Convective Heat and Mass Transfer, McGraw-Hill, NY (1966), p. 173.

164. A. V. Sheklein, Appl. Solar Energy $\underline{3}$ (4), 84 (1967).

165. A. B. Meinel and M. P. Meinel, <u>Applied Solar Energy</u>, Addison-
      Wesley, Reading, MA (1976), p. 282.

166. A. V. Sheklein and N. B. Rekant, Appl. Solar Energy $\underline{7}$ (3),
      24 (1971).

167. W. O. Lytle and A. E. Junge, "Electroconductive Products and
      Production Thereof," expired U.S. Patent No. 2,566,346
      (1951).

APPENDIX   I

COMPUTER PROGRAM OF SCALE MODEL

>T TT-DT1 SOL 4 SRC

```
          COMMON PPH,PHG,TAM,T1,HFX, SHD, ALT, TB, TEX, T12,DAY,T16,ASUF,
          1BSU,B,QCO,ADT
1         FORMAT (1H ,10X,35HSOLAR COLLECTOR TEMPERATURE PROFILE)
2         FORMAT (1H , 32HTHE FOLLOWING VARIABLES ARE USED)
3         FORMAT (F7.2)
4         FORMAT (1H+,13HPPH =          )
5         FORMAT (1H+,13HPHG =          )
6         FORMAT (1H+,13HTAM =          )
7         FORMAT (1H+,12HT1 =          )
8         FORMAT (1H+,13HHFX =          )
9         FORMAT (1H+,13HSHD =          )
10        FORMAT (1H+,13HALT =          )
11        FORMAT (1H+,12HTB =          )
12        FORMAT (1H+,13HTEX =          )
13        FORMAT (1H+,13HT12 =          )
14        FORMAT (1H+,13HDAY =          )
15        FORMAT (1H+,13HT16 =          )
          WRITE (4,1)
16        WRITE (4,2)
          WRITE (4,4)
          READ (4,3) PPH
          WRITE (4,5)
          READ (4,3) PHG
          WRITE (4,6)
          READ (4,3) TAM
          WRITE (4,7)
          READ (4,3) T1
          WRITE (4,8)
          READ (4,3) HFX
          WRITE (4,9)
          READ (4,3) SHD
          WRITE (4,10)
          READ (4,3) ALT
          WRITE (4,11)
          READ (4,3) TB
          WRITE (4,12)
          READ (4,3) TEX
          WRITE (4,13)
          READ (4,3) T12
          WRITE (4,14)
          READ (4,3) DAY
          WRITE (4,15)
          READ (4,3) T16
          ASUF = 0.0
          BSU = 0.0
          B = 0.0
          QCO = 0.0
          ADT = 0.0
          CALL SOL5
          CALL SOL6
          GO TO 16
          END
```

```
      SUBROUTINE SOL5
      COMMON PPH,PHG,TAM,T1,HFX,SHD,ALT,TB,TEX,T12,DAY,DUM(2),
     1DUM1(4),BFX,GM,FLO
      CPT = PPH*(1.062-0.0008*TAM)/1.042
      FLO = EXP(3.41+.495*ALOG(CPT)-.062*ALOG(CPT)**2+.0161*ALOG(CPT)
     1**3)
      FLO = FLO*3.59*(72.5+PHG)/(273.0+T12)
      GM = FLO*0.0297
      VEL = FLO*0.93
      FX1 = 36.4*(T1-TAM)
      ANG = ATAN(91.5/ALT)
      PRF = HFX*697.0/SIN(ANG)
      IF (DAY-183.0)17,17,18
17    ETX = 1400.0-(0.497*DAY)
      GO TO 19
18    ETX = 1309.0+0.497*(DAY-183.0)
19    RT = PRF/ETX
      HD = 3.01-6.85*RT+4.19*RT**2
      FX2 = PRF*(1.0-HD)*COS(0.86-ANG)
      AFX = (FX1+FX2)/2.0
      BFX = AFX*3.67E-3
      WRITE (4,100)FX1,FX2,AFX
      WRITE (4,105) FLO,VEL
      WRITE (4,110)
100   FORMAT (1H ,6HFX1 = ,F7.1,4X,6HFX2 = ,F7.1,4X,6HAFX = ,F7.1)
105   FORMAT (1H0,6HFLO = ,F6.1,4X,10HAND VEL. = ,F6.1)
110   FORMAT (1H0,5HPOSN.,4X,2HRE,7X,2HRA,4X,7HT INCR.,4X,
     16HBULK T,6X,3HSUF,2X,8HAVG. SUF,4X,3HTW2)
      RETURN
      END
```

```
        SUBROUTINE SOL6
        COMMON DUM(5),SHD,ALT,TB,TEX,DUM1(2),T16,ASUF,
       1BSU,B,QCO,ADT,BFX,GM,FLO
        DT2 = (T16-TB)/42.0
        QN2 = DT2*GM*0.521
        DO 40 I = 1,91
        VI1 = 2.13E-4*(1.0+0.0025*TB)
        RHO = 0.487/(TB+273.0)
        VI2 = VI1/RHO
        CON = 1.63E-4*(1.0+0.0026*TB)
        RE = 4.75E-3*FLO/VI1
        RA = 2.75E+3*DT2/((TB+273.0)*VI2**2)
        Z = 1.92*RE/(32.0+FLOAT(I)-SHD)
        ANU = 4.18+3.17E-2*Z-3.67E-5*Z**2+1.91E-8*Z**3
        IF (RA-1000.0)24,21,21
21      BNU = 0.31*RA**0.27
        GO TO 31
24      IF ((RE*RA)-2.75E+5)30,27,27
27      BNU = 2.0
        GO TO 31
30      BNU = 0.27*(RE*RA)**0.16
31      SNU = 5.74E+3*CON*ANU*BNU
        TW2 = TB+0.114*QN2/(CON*SNU)
        TAV = (TW2-TEX)/2.0+273.0+TEX
        QIS2 = 1.04E-3*(TW2-TEX)*(2.87-4.15E-3*TAV+1.76E-5*TAV**2)
        QGL2 = 0.90E-11*(TW2+273.0)**4
        QTR2 = 1.79E-11*TAV**4
32      QN2 = BFX-QIS2-QGL2-QCO-QTR2
        DT2 = QN2/(GM*0.521)
        TW3 = TW2+DT2
        TAV = (TW3-TEX)/2.0+273.0+TEX
        QIS3 = 1.04E-3*(TW3-TEX)*(2.87-4.15E-3*TAV+1.76E-5*TAV**2)
        QGL3 = 0.90E-11*(TW3+273.0)**4
        QTR3 = 1.79E-11*TAV**4
        QN3 =BFX-QIS3-QGL3-QCO-QTR3
        DT3 = QN3/(GM*0.521)
        QC2 = DT2*3.04
        QC3 = DT3*3.04
        QCO = (QC2-QC3)
        IF (ABS(DT2-ADT)-0.01)36,36,34
34      ADT = DT2
        GO TO 32
36      TB = TB+DT2
        SUF = QN2/BFX
        BSU = BSU+SUF
        ASUF = BSU/FLOAT(I)
        IF (I.LE.IFIX(B)) GO TO 40
38      WRITE (4,115) I,RE,RA,DT2,TB,SUF,ASUF,TW2
        B = B+10.0
40      CONTINUE
115     FORMAT (1H ,I2,4X,F7.1,2X,F7.1,2X,F5.1,5X,F6.1,6X,F4.2,4X,F4.2,
       14X,F6.1)
        RETURN
        END
```

Definition of Terms in Computer Program
(Listed in Order of Appearance)

Input Parameters:

PPH   measured ΔP of n-butyl phthalate, cm

PHG   measured ΔP of mercury, cm

TAM   ambient temperature (shaded thermometer or thermocouple T2), °C

T1   measured temperature of Cu plate in flux bulb (= T1), °C

HFX   total solar flux on a horizontal surface, langley min^{-1}

SHD   measured length of shadow at receiver inlet, from beginning of aperture, cm

ALT   measured horizontal length of shadow cast by 91.5 cm high vertical rod, cm

TB   bulk temperature of gas (initially = T14, at m = 0), °C

TEX   measured average (axial) temperature of insulation exterior (= (T3 + T8)/2, = T_e), °C

T12   measured temperature of gas at flow constriction (= T12), °C

DAY   day of the year

T16   measured temperature of gas near axial center of receiver (= T16), °C, used only at first step, to start computation

Other Terms in Program:

CPT ΔP of n-butyl phthalate corrected to 25°C, cm

FLO   gas flow rate at STP (0°C, 760 torr), liter min^{-1}

GM gas mass flow rate, $g\ s^{-1}$

VEL gas velocity at STP, $cm\ s^{-1}$

FX1 calculated direct perpendicular solar flux, from flux bulb ΔT, $W\ m^{-2}$

ANG solar altitude above horizon, °

PRF total perpendicular solar flux, $W\ m^{-2}$

ETX perpendicular extraterrestrial solar flux, $W\ m^{-2}$

RT flux ratio

HD diffuse fraction of total solar flux

FX2 calculated direct perpendicular solar flux, from total horizontal reading, $W\ m^{-2}$

AFX average of FX1 and FX2, $W\ m^{-2}$

BFX concentrated solar flux available at receiver Pyrex aperture, $W\ cm^{-1}$

DT2 temperature rise of gas over step, $(T_b)_m - (T_b)_{m-1}$, $°C\ cm^{-1}$

QN2 net heat flux into gas at step m, $W\ cm^{-1}$

VI1 dynamic viscosity of gas $(= \mu)$ at $(T_b)_{m-1}$, $g\ s^{-1}\ cm^{-1}$

RHO density of gas $(= \rho)$ at $(T_b)_{m-1}$, $g\ cm^{-3}$

VI2 kinematic viscosity of gas $(= \nu)$ at $(T_b)_{m-1}$, $cm^2\ s^{-1}$

CON thermal conductivity of gas $(= k)$ at $(T_b)_{m-1}$, $W\ cm^{-1}\ °C^{-1}$

RE Reynolds number $(= Re)$, dimensionless

RA Rayleigh number $(= Ra)$, dimensionless

Z   axial position from onset of heating ($= 1/z^+$), dimensionless

ANU   ratio of Nusselt numbers, (developing velocity and temperature profiles Nu)/(fully established velocity and temperature profiles Nu), both Nu's at an assumed constant axial heat input

BNU   ratio of Nusselt numbers, (Nu from combined convection at 41° tilt)/(Nu for pure forced convection, horizontal orientation), both Nu's at an assumed constant axial heat input

SNU   actual Nusselt number, including effects of developing flow, tilt, buoyancy, and varying fluid thermal conductivity, dimensionless

TW2   average (peripheral) temperature of heat transfer surfaces, Pyrex + graphite, at step m, °C

TAV   mean (transverse) insulation temperature at step m, °K

QIS2   heat conducted (lost) through insulation at step m, W cm^{-1}

QGL2   heat radiated (lost) by Pyrex window at step m, W cm^{-1}

QTR2   heat radiated (lost) by Transite sides of aperture at step m, W cm^{-1}

TW3   average (peripheral) temperature of heat transfer surfaces, Pyrex + graphite, at step m, °C

QIS3   heat conducted (lost) through insulation at step m + 1, W cm^{-1}

QGL3   heat radiated (lost) by Pyrex window at step m + 1, W cm^{-1}

QTR3   heat radiated (lost) by Transite sides of aperture at step m + 1, W cm^{-1}

QN3   net heat flux into gas at step m + 1, W cm^{-1}

DT3   temperature rise of gas over step, $(T_b)_{m+1} - (T_b)_m$, °C cm^{-1}

QC2   total heat conducted axially, Pyrex + graphite, at step m, W cm^{-1}

QC3   total heat conducted axially, Pyrex + graphite, at step m + 1, $W\ cm^{-1}$

QCO   net heat conducted axially (lost), Pyrex + graphite, at step m, $W\ cm^{-1}$

ADT   dummy temperature used in computing axial loss

SUF   Solar Utilization Factor, a measure of collector thermal efficiency, at step m

BSU   axial sum of SUF's

ASUF   average SUF over axial length (= $\overline{\overline{SUF}}$)

B   dummy count, used to print only every 10th computation

APPENDIX II

COLLECTOR TEMPERATURE PROFILES

PERFORMANCE ON 29.III.77, 1:15 P.M.

FX1 = 946.4   FX2 = 774.2   AFX = 860.3
FLO = 20.9   AND VEL. = 19.5

POSN.	RE	RA	T INCR.	BULK T	SUF	AVG. SUF	TW2
1	323.5	173.3	3.5	180.5 (181)	0.35	0.35	212.1 (253)
11	308.3	145.7	2.5	207.9	0.25	0.29	243.3
21	297.2	94.2	2.0	229.9	0.20	0.26	258.8
31	289.0	63.8	1.6	247.5	0.16	0.23	271.0
41	282.7	44.8	1.3	261.5 (272)	0.13	0.21	280.7
51	277.9	32.3	1.0	272.6	0.10	0.19	288.3
61	274.2	23.8	0.8	281.4	0.08	0.18	294.3
71	271.4	17.7	0.6	288.4	0.07	0.16	299.0
81	269.1	13.4	0.5	294.0	0.05	0.15	302.7
91	267.4	10.5	0.4	298.4 (316)	0.04	0.14	305.7 (346)

PERFORMANCE ON 19.XI.76, 1:50 P.M.

FX1 = 582.4   FX2 = 550.0   AFX = 566.2
FLO = 26.6   AND VEL. = 24.7

POSN.	RE	RA	T INCR.	BULK T	SUF	AVG. SUF	TW2
1	544.8	970.7	3.4	38.4 (38)	0.66	0.66	79.3 (90)
11	510.4	756.4	2.7	67.0	0.53	0.58	119.6
21	484.0	478.5	2.3	92.0	0.46	0.54	138.2
31	463.2	317.9	2.0	113.7	0.40	0.50	154.8
41	446.7	220.1	1.7	132.3 (131)	0.35	0.47	168.6
51	433.3	158.3	1.5	148.4	0.30	0.44	180.2
61	422.5	117.1	1.3	162.3	0.26	0.41	189.9
71	413.6	88.7	1.1	174.1	0.22	0.39	198.2
81	406.3	68.4	0.9	134.3	0.19	0.36	205.3
91	400.2	53.5	0.8	193.0 (193)	0.16	0.34	211.2 (223)

PERFORMANCE ON 19.III.77, 1:30 P.M.

FX1 = 855.4   FX2 = 888.4   AFX = 871.9
FLO = 32.3   AND VEL. = 30.0

POSN.	RE	RA	T INCR.	BULK T	SUF	AVG. SUF	TW2
1	553.6	353.7	3.4	123.4 (123)	0.53	0.53	175.6 (216)
11	523.5	278.6	2.7	152.6	0.43	0.46	210.0
21	500.3	183.3	2.3	177.7	0.37	0.43	227.7
31	482.0	126.2	2.0	199.2	0.31	0.40	242.6
41	467.4	90.0	1.7	217.5 (224)	0.27	0.37	255.0
51	455.7	66.1	1.4	233.1	0.23	0.35	265.4
61	446.2	49.6	1.2	246.4	0.19	0.32	274.2
71	438.4	38.0	1.0	257.6	0.16	0.30	281.6
81	432.1	29.5	0.9	267.1	0.14	0.28	287.7
91	426.9	23.2	0.7	275.1 (281)	0.12	0.27	292.9 (318)

PERFORMANCE ON 15.X.76, 1:30 P.M.

FX1 = 800.8   FX2 = 707.7   AFX = 754.3
FLO = 44.7   AND VEL. = 41.6

POSN.	RE	RA	T INCR.	BULK T	SUF	AVG. SUF	TW2
1	853.5	575.0	2.6	69.6 (70)	0.65	0.65	131.2 (160)
11	812.3	449.5	2.2	93.0	0.56	0.59	159.1
21	778.1	316.1	2.0	114.3	0.51	0.56	174.2
31	749.6	227.4	1.8	133.5	0.46	0.54	188.8
41	725.8	168.6	1.6	150.8 (155)	0.41	0.51	201.3
51	705.6	128.2	1.5	166.3	0.37	0.49	212.3
61	688.5	99.4	1.3	180.2	0.33	0.46	221.8
71	673.9	78.4	1.2	192.7	0.30	0.44	230.3
81	661.3	62.7	1.1	203.8	0.26	0.42	237.7
91	650.5	50.8	0.9	213.7 (202)	0.23	0.40	244.3 (240)

Definition of Terms in Computer Results

FX1   calculated direct perpendicular solar flux, from flux bulb ΔT (discussed in Chapter IV), $W\ m^{-2}$

FX2   calculated direct perpendicular solar flux, from Weather Bureau Station (discussed in Chapter IV), $W\ m^{-2}$

AFX   (FX1 + FX2)/2

FLO   Ar flow rate at STP, $liter\ min^{-1}$

VEL   Ar velocity in receiver at STP, $cm\ s^{-1}$

POSN.   axial position along test section, cm

RE   Reynolds number

RA   Rayleigh number

T INCR.   Ar bulk temperature rise from previous step, $°C\ cm^{-1}$

BULK T   Ar bulk temperature (= T_b), °C, in parentheses are measured temperatures

SUF   Solar Utilization Factor, a measure of collector thermal efficiency (= q_N/q_S), dimensionless

ASUF   average SUF over length, Σ SUF/POSN., dimensionless

TW2   average (peripheral) temperature of heat transfer surfaces, Pyrex + graphite, °C, in parentheses are measured temperatures of the graphite absorber

APPENDIX   III

COMPUTER PROGRAM OF FULL-SCALE COLLECTOR

```
        SOL11
        COMMON DIA,TK,WW,EW,ET,RM,TR
1       FORMAT (1H ,10X,35HSOLAR COLLECTOR TEMPERATURE PROFILE)
2       FORMAT (1H ,32HTHE FOLLOWING VARIABLES ARE USED)
3       FORMAT (F7.2)
4       FORMAT (1H+,13HDIA =          )
5       FORMAT (1H+,12HTK =          )
6       FORMAT (1H+,12HWW =          )
7       FORMAT (1H+,12HEW =          )
8       FORMAT (1H+,12HET =          )
9       FORMAT (1H+,12HRM =          )
10      FORMAT (1H+,12HTR =          )
        WRITE (4,1)
20      WRITE (4,2)
        WRITE (4,4)
        READ (4,3) DIA
        WRITE (4,5)
        READ (4,3) TK
        WRITE (4,6)
        READ (4,3) WW
        WRITE (4,7)
        READ (4,3) EW
        WRITE (4,8)
        READ (4,3) ET
        WRITE (4,9)
        READ (4,3) RM
        WRITE (4,10)
        READ (4,3) TR
        WRITE (4,25)
25      FORMAT (1H ,5HPOSN.,8X,7HT INCR.,5X,6HBULK T,9X,3HSUF,7X,
        18HAVG. SUF)
        CALL SOL12
        GO TO 20
        END
```

```
       SUBROUTINE SOL12
       COMMON DIA,TK,WW,EW,ET,RM,TR
       BSU = 0.0
       K = 90
       TB = 349.0
       A = (TK**2+1.2*TK*WW+WW**2)**0.5
       Y = 1.2*TK+WW
       FT = (TK+Y-A)/(2.0*TK)
       FW = (A-TK)/WW
       DO 40 I = 10,700,10
       QG = WW*0.1*EW*FW*5.67E-8*(TB+273.0)**4
       TAV = (TB-25.0)/2.0+298.0
       QT = 0.2*TK*ET*FT*5.67E-8*TAV**4
       B = ALOG(1.0+1.9*TK/DIA)
       QC = 0.63*(TB-25.0)*(2.87-4.15E-3*TAV+1.76E-5*TAV**2)/B
       QS = 3.2E+4*RM*TR
       QN = QS-QG-QT-QC
       DT = QN/4.45E+3
       TB = TB+DT
       SUF = QN/QS
       BSU = BSU+SUF
       ASUF = 10.0*BSU/FLOAT(I)
       IF (I.LE.K) GO TO 40
30     WRITE (4,35) I,DT,TB,SUF,ASUF
35     FORMAT (1H ,I4,8X,F5.1,8X,F6.1,8X,F4.2,8X,F4.2)
       K = K+100
40     CONTINUE
       RETURN
       END
```

Definition of Terms in Computer Program

DIA   inside diameter of receiver pipe, cm

TK   insulation thickness, cm

WW   window width (i.e., aperture width at glass pipe), cm

EW   emittance of glass at aperture

ET   emittance of aperture sides (Transite)

RM   mirror reflectance

TR   convective cover transmittance

POSN.   axial position from inlet, m

T INCR.   temperature rise over element length, °C

K   counter, for printing every 10th computation (i.e., every 100 m of length)

TB   bulk gas temperature (= T_b), °C

A, Y   computed aperture dimensions used in determining the view factors, cm

FT   view factor of aperture sides, dimensionless

FW   view factor of glass window, dimensionless

QG   radiant loss from window, W

TAV   average (linear) temperature of aperture sides at a given axial position, °K

QT   radiant loss from aperture sides, W

B   accounts for mean insulation thickness, dimensionless

QC   conduction loss through insulation, W

QS   reflected solar flux at glass window, W

QN   net heat into fluid, W

DT   temperature rise over element length, °C

SUF   Solar Utilization Factor, discussed in text, dimensionless

BSU ΣSUF over length

ASUF   average SUF over length (= $\overline{\overline{SUF}}$)

VITA

Zenen Igor Antoniak was born in Przemysl, Ukraine, on
April 12, 1940. When he was nine, his family moved to Philadelphia,
Pennsylvania, USA. He attended LaSalle High School for the first
two years, then Central High School and graduated in June 1958.
In September of 1958 he enrolled at Drexel University in Philadel-
phia, PA, but departed in 1961 because of financial difficulties
without obtaining a degree. A varied engineering career ensued
with employment by a number of firms such as Baldwin-Lima-Hamilton,
the DuPont Company, Hercules, Inc., and Scott Paper Company, among
other. Six months in 1962 were spent on active duty training in
the Army Medical Corps. He resumed his studies at Drexel University
in September, 1967 and received a B.S. Degree in Mechanical Engineer-
ing in 1970 and a M.S. Degree in Environmental Engineering in 1971.
He was then employed as an engineer specializing in air pollution
by the United States Environmental Protection Agency, Region III
Office, in Philadelphia, PA, for three years. In September of 1974
he went to The Pennsylvania State University to become a candidate
for the Ph.D. Degree in Fuel Science.

He is a member of the American Society of Mechanical Engineers,
the International Solar Energy Society, and Sigma Xi.

DISTRIBUTION

Commander (NSEA 09G32)
Naval Sea Systems Command
Department of the Navy
Washington, D. C. 20362   Copies 1 and 2

Commander (NSEA 0342)
Naval Sea Systems Command
Department of the Navy
Washington, D. C. 20362   Copies 3 and 4

Defense Documentation Center
5010 Duke Street
Cameron Station
Alexandria, VA 22314   Copies 5 through 16